ABSTRACT

Title of Dissertation: MULTI-GEV LASER WAKEFIELD
ACCELERATION IN OPTICALLY
GENERATED PLASMA WAVEGUIDES

Jaron Eugene Shrock
Doctor of Philosophy, 2023

Dissertation directed by: Professor Howard Milchberg
Department of Physics

Plasma based electron accelerators offer a promising path to overcoming the significant technological and economic challenges facing the evolution to higher energies by radiofrequency (RF) accelerator technology. In particular, laser-driven wakefield acceleration (LWFA) in plasmas can produce accelerating gradients 1000 times larger than linear RF accelerators, enabling the production of GeV-scale electron bunches in just a few centimeters of acceleration. Efficient LWFA of electrons to this energy scale requires the use of optical guiding to maintain drive laser intensity over much longer distances than the characteristic diffraction length of the pulse.

In this dissertation, I will present the first successful implementations of optically generated plasma waveguides in multi-GeV laser wakefield acceleration. I will focus on three primary topics: (1) experimental considerations for generating and diagnosing meter-scale plasma waveguides and the wakefield acceleration process, (2) the experimental demonstration of electron bunches accelerated up to 5 GeV in an all-optical LWFA, and (3) development of a

model of drive pulse evolution and electron injection in agreement with a broad range of our experimental results, including the demonstration of localized electron injection through modification of the waveguide properties.

MULTI-GEV LASER WAKEFIELD ACCELERATION IN OPTICALLY GENERATED
PLASMA WAVEGUIDES

by

Jaron Eugene Shrock

Dissertation submitted to the Faculty of the Graduate School of the
University of Maryland, College Park, in partial fulfillment
of the requirements for the degree of
Doctor of Philosophy
2023

Advisory Committee:
 Professor Howard Milchberg, Chair
 Professor Phillip Sprangle
 Professor Wendell Hill III
 Professor Drew Baden
 Professor Ki-Yong Kim

Dedication

For Amanda.

Acknowledgements

First, I would like to thank Amanda for the endless love and support over the last few years. Things didn't unfold like we expected, but I could never have made it to this point without you. I also couldn't have made it here without unyielding support of my parents, Kelley and Gene, and am so grateful for the endless opportunities and encouragement they have given me. I am also so thankful for Amanda's parents, Bob and Jill, as well as our many friends who have been nothing but kind during this journey.

Next, I would like to thank my advisor, Dr. Howard Milchberg, for his excellent guidance, mentorship, and willingness to open every door for his students. Howard has given me opportunities and challenges available to few graduate students, and I will always be grateful for his support in facing them.

None of the work in this dissertation was completed alone. I am indebted to my fellow lab members not just for their keen scientific insights, but for the open and supportive environment to which they all contribute. In particular, I would like to thank Dr. Bo Miao, Ela Rockafellow, and Dr. Linus Feder for their patience and perseverance during long nights in the lab, as well as their comradery during our extended research campaigns. I am also grateful for the many simulating (and sometimes welcomingly distracting) conversations with those group members I haven't had the opportunity to work with on a daily basis: Matthew Le, Lucas Railing, Scott Hancock, Dr. Sina Zahedpour, Andrew Goffin, Dr. Robert Schwartz, Dr. Daniel Woodbury, Dr. Ilia Larkin, Stefan Waczynski, Dr. Anthony Zingale, Nischal Tripathi, Michael Parker, and Frederica Liu.

Table of Contents

List of Figures

Chapter 1: Introduction

1.1 *Motivation and outline*

Particle accelerators are an indispensable tool for modern scientific research, and have broad applications in industry. Among many other uses, they are employed in such varied areas as advanced radiation sources for crystallography and nanotechnology [1], in the treatment of certain cancers [2], in the production of isotopes [3,4], and to study fundamental physics [5,6]. Electron accelerators in particular have uses in particle colliders and advanced light sources [7]. Conventional radiofrequency (RF) accelerators rely on oscillating electromagnetic fields to accelerate electrons to increasingly high energies in sequential cavities. The voltage and phase of the fields are carefully controlled so that the accelerated electron bunch is positioned to experience a maximally accelerating field in each cavity. The accelerating fields of RF accelerators are limited by material breakdown potentials to about 100 MeV/m, which means that high-energy accelerators such as the Stanford Linear Accelerator (SLAC), Fermilab Tevatron, and Large Hadron Collider (LHC) require km-scale acceleration distances. The extreme scale and cost of these devices is prohibitive for not just the development of TeV scale accelerators, but widespread proliferation of current technology beyond a handful of select research facilities.

As first proposed by Tajima and Dawson, [8] plasma based accelerators can sustain accelerating fields 1000 times greater than conventional RF technology, and offer a promising path towards the future development of a potential TeV-scale lepton collider [9] and unique light sources [10–15]. Plasma accelerators rely on the electric fields (wakefields) from plasma waves (wakes) driven by ultra-intense laser pulses

[16,17] or relativistic particle bunches [18–21]. Laser driven wakefield accelerators (LWFAs) have demonstrated multi-GeV electron gain in ≤ 20 cm [22–25]. Beam-driven wakefield accelerators (PWFAs) have been shown to more than double the energy of some electrons from a 42 GeV drive beam—duplicating the energy gain the of 3 km long SLAC in just 85 cm of plasma [20]. For use in an eventual collider [9,26], as an x-ray [27] or synchrotron radiation light source [28], or as the driver for a free electron laser (FEL) [29–31], significant improvements must be made in several areas [32]: higher energy gain, more repeatable performance, and lower beam emittance. These qualities, particularly energy gain and repeatability, can be improved by use of a plasma waveguide, which extends the interaction length of the drive pulse beyond its natural diffractive range. Use of a plasma waveguide enables maximum acceleration in the more stable and efficient quasi-linear regime (see Sec. 1.3.2) and offers a path to controllable electron injection into the wake.

In this dissertation, we present the first implementation of novel laser-generated plasma waveguide formation techniques in a multi-GeV LWFA (the highest demonstrated energy gain in an all-optical LWFA at the time) and outline a new picture for intense pulse propagation and electron injection in meter scale LWFAs within long plasma waveguides. This chapter will provide a brief introduction to relevant topics: how ultra-intense lasers interact with matter, the key elements of LWFAs and plasma waveguides, two techniques developed by our group at the University of Maryland for the optical generation of meter scale plasma waveguides, and computational approaches for modeling LWFAs and pulse propagation.

Chapter 2 discusses the key elements for implementing and diagnosing LWFAs reliant on these techniques. This includes Bessel beam generation and the design of meter-scale supersonic gas jets as well as optical, plasma, and electron bunch diagnostics.

In Chapter 3, we discuss results from experiments performed using the ALEPH laser system at Colorado State University, where a self-waveguiding pulse was used to accelerate electrons up to 5 GeV over a 20 cm gas jet. This includes analysis of the plasma structure, guided pulse, and accelerated electron bunches, as well as complementary particle-in-cell (PIC) simulations detailing the process.

Chapter 4 focuses on the details of intense pulse propagation and electron injection in meter scale plasma waveguide LWFAs. We outline three characteristic phases of pulse evolution resultant from both linear and non-linear effects and show that the model is well-matched to experimental results. We present further experimental results demonstrating that localization of a dopant gas within the waveguide limits the number of times localized injection occurs, producing electron beams with a single quasi-monoenergetic peak.

1.2 *Ionization of neutral gases by high-intensity lasers*

The development of increasingly bright coherent light sources and discovery of chirped pulse amplification (CPA, [33]) has enabled exploration of laser-matter interaction regimes where the strength of the laser electric field becomes comparable to the electrostatic forces which bind electrons to ions. In this 'ultra-intense' regime, the electromagnetic fields of a laser pulse can ionize atoms and rapidly heat the resultant plasma. Ionization by short-pulse ($\lesssim$ ps) lasers occurs in three distinct

3

regimes: (1) multi-photon ionization (MPI), (2) tunneling ionization, and (3) optical field ionization (OFI, also referred to as 'over the barrier' or 'above threshold' ionization') [34–36]. One way to quantify the comparative strength of the interaction between a laser pulse and bound electron is through the Keldysh parameter, γ_k [34]. This compares the relative strengths of the electron binding energy and momentum in the electric field:

$$\gamma_k = \sqrt{\frac{E_i}{2U_p}}, \tag{1.1}$$

where E_i is electron ionization energy and $U_p \sim E^2$ is the laser ponderomotive energy (see Sec. 1.4). Cartoon depictions of the different regimes are shown in Figure 1.1.
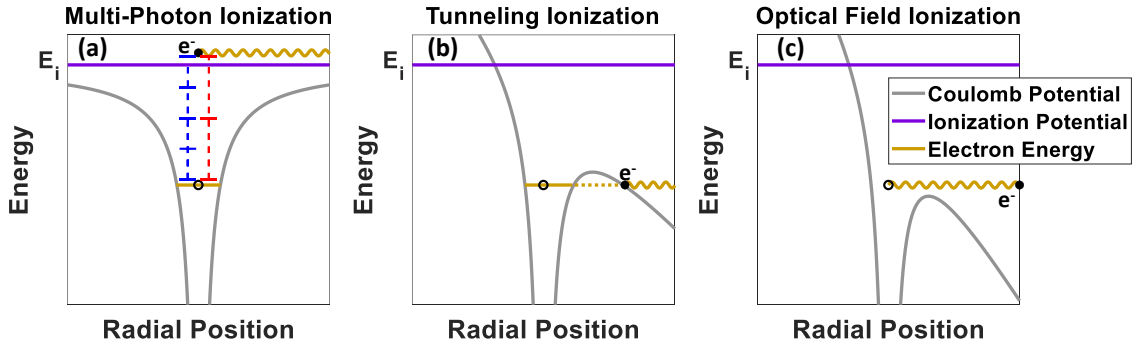
Figure 1.1: Regimes of ultra-intense laser ionization. An electron (black dot) is bound in a Coulomb potential (gray curve) in its ground state (gold line), and requires energy E_i to overcome the ionization potential (purple line). **(a)** multi-photon ionization (MPI). Absorption of multiple photons sufficiently increases electron energy until it is above the ionization threshold. **(b)** tunneling ionization. A strong electric field from the laser pulse perturbs the Coulomb potential and increases the probability that the electron is able to tunnel through the potential barrier and escape. **(c)** optical field ionization (OFI). The perturbation from the laser electric field is significant enough that the electron is no longer bound and escapes.

When $\gamma_k \gg 1$, the electron energy gained from motion in the laser field is insufficient to overcome the ionization potential barrier. Absorption of multiple photons of energy $\hbar\omega$ can sufficiently increase the energy to free the electron (panel (a)). For a given ionization potential and frequency ω, the number of photons required

for multiphoton ionization is $n = \lceil E_i/\hbar\omega \rceil$, where $\lceil x \rceil$ denotes the ceiling function. The ionization rate W_n for n-photon absorption will depend on the number of photon-electron collisions, specifically

$$W_n = \sigma_n I_L^n, \qquad (1.2)$$

where σ_n is the n-photon absorption cross section and I_L is the laser intensity. As seen in Eq. 1.2, the intensity requirement increases exponentially with the number of photons required for MPI. As laser intensity increases and $\gamma_k \sim 1$, the electric field becomes of comparable strength to the Coulomb potential binding the electron to its ion. Tunneling ionization occurs when the perturbation from the external laser field is significant enough to dramatically increase the probability of the bound electron tunneling outside the potential (panel (b)). OFI (above threshold ionization) occurs when $\gamma_k \ll 1$. Under this condition, the laser pulse electric field dominates the binding field and the electron is instantaneously liberated (panel (c)), gaining energy from ponderomotive (Sec. 1.3.1) motion in the electric field [35]. An estimate [37] of the laser intensity required in the barrier-suppression-ionization limit is

$$I_{OFI} = \frac{cE_i^2}{128\pi Z^2 e^6}, \qquad (1.3)$$

where Z is the ionization state of the product ion. As an example, for hydrogen $I_{OFI} \approx 1.4 \times 10^{14}\ W/cm^2$, which is easily achievable even with low-energy ($\gtrsim$ mJ) ultra-short ($\lesssim 100$ fs) laser pulses.

We note one other ionization regime which is accessible for longer pulses (> ps). If the intensity is sufficiently high to ionize some seed population of electrons (or if one is present due to some other process [38]), these electrons will oscillate in the electric field. However, when a free electron is located near ions or neutral atoms, the

oscillations in the laser field can cause electron-neutral or electron-ion collisions, knocking the electron out of phase with the electric field and allowing it to keep some of the oscillation energy. This process is called inverse bremsstrahlung (IB) heating. IB heated electrons can gain sufficient energy to collisionally ionize the surrounding neutrals (or ions if they are not fully ionized) in a cascading effect. This is called 'avalanche' ionization [39].

1.3 Laser wakefield acceleration (LWFA)

A particle-in-cell (PIC, see Sec. 1.6) simulation demonstrating the LWFA process is shown in Figure 1.2. The ponderomotive force (Sec 1.3.1) of an ultra-intense laser pulse expels electrons from the optical axis. This density perturbation forms a plasma wave (a wake, in analogy to a boat traveling atop a lake) behind the pulse with regions of low and high electron density (the much heavier protons are effectively stationary compared to the electrons on the short timescales of the laser pulse and electron motion). Due to their appearance, the positively charged regions are sometimes called 'buckets'. At the back of each bucket, where the electron density transitions from low to high, there is a large electric field which can accelerate electrons that are injected into and trapped in the region. As these electrons are accelerated, they eventually begin to move faster than the drive pulse and traverse the wake to the region where the electric fields slow them down (Sec. 1.3.2). Successful LWFA relies on two key pieces: (1) efficient driving of plasma waves over a long enough distance to maximally accelerate electrons and (2) effective injection of free electrons into the fields generated by those waves (Sec. 1.3.3).
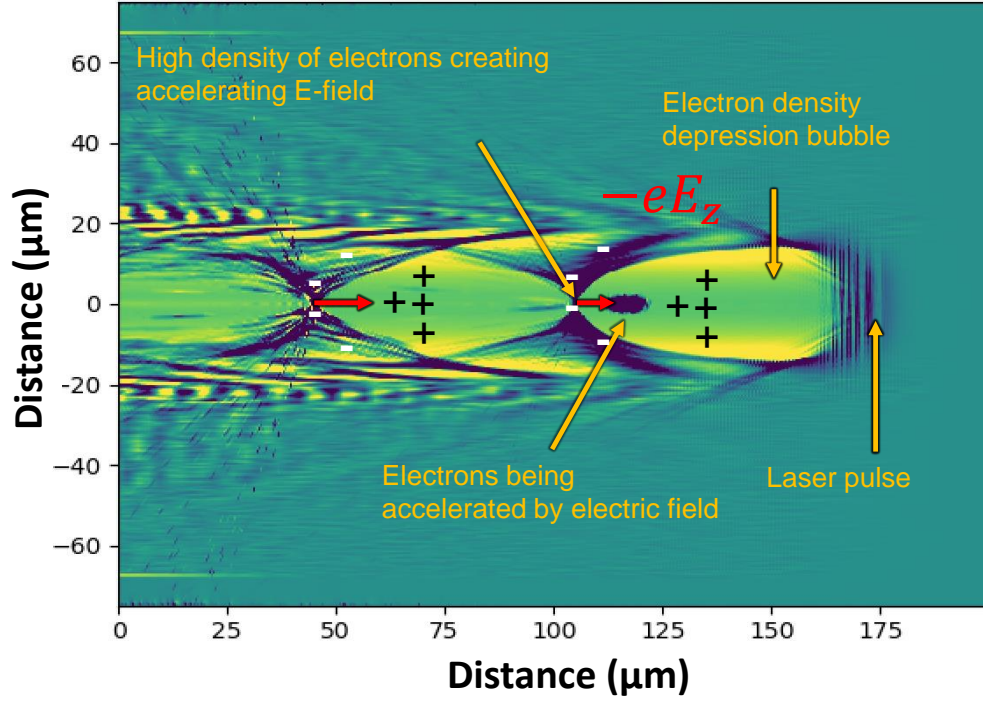
Figure 1.2: Example of laser wakefield acceleration. An ultra-intense laser pulse expels electrons from the optical axis and drives a plasma wave behind the pulse. The ions are effectively stationary on the electron movement timescales, resulting in bulk charge separation in phase with the plasma electron oscillations. This generates strong electric fields, which can rapidly accelerate coupled electrons beyond the velocity of the propagating pulse.

1.3.1 Ponderomotive force and plasma waves

Electrons are driven away from the optical axis by the ponderomotive force, $\boldsymbol{F_p}$, of an intense laser pulse propagating in a plasma. In the linear regime, this can be derived starting with the electron cold fluid momentum equation,

$$\frac{d\boldsymbol{p}}{dt} = -e\left(\boldsymbol{E} + \boldsymbol{v} \times \frac{\boldsymbol{B}}{\boldsymbol{c}}\right), \tag{1.4}$$

in Gaussian units, where $\mathbf{p}$ and $\mathbf{v}$ are the momentum and velocity of the electron fluid elements and d/dt is the convective derivative [16]. We define the dimensionless parameter $|a| = e|\boldsymbol{A}|/m_e c^2$, where $\mathbf{A}$ is the vector potential corresponding to the laser field. a is proportional to the electron quiver momentum in the electric field, $\boldsymbol{p_q} =$

$m_e c\boldsymbol{a}$. The maximum value of $\boldsymbol{a}$, corresponding to the peak laser intensity, is labelled a_0. It can be calculated from the peak intensity I_0 as $a_0^2 \cong 7.3 \times 10^{-19}[\lambda(\mu m)]^2 I_0 (W/cm^2)$. For $a_0 > 1$, the electron momentum is sufficiently high that relativistic effects become significant. This defines the relativistic, non-linear regime of laser-plasma interactions, while $a_0 \ll 1$ defines the linear regime. The transition regime between these two, $a_0 \sim 1$, features some characteristic behavior of both and is called the quasilinear regime.

Assuming that the field is polarized transversely, and $|a| \ll 1$, we can use Eq. 1.4 to find second order motion in $\delta\boldsymbol{p} = \boldsymbol{p} - \boldsymbol{p_q}$:

$$\frac{d\delta\boldsymbol{p}}{dt} = -\left[\frac{\boldsymbol{p_q}}{m_e} \cdot \nabla\right]\boldsymbol{p_q} - \boldsymbol{p_q} \times (c\nabla \times \boldsymbol{a}).$$ (1.5)

This gives the ponderomotive force in the linear regime.

$$\boldsymbol{F_p} = \frac{d\delta\boldsymbol{p}}{dt} = -m_e c^2 \nabla\left(\frac{a^2}{2}\right).$$ (1.6)

For a Gaussian or near-Gaussian drive pulse, where the maximum intensity is at the transverse center, Eq. 1.6 indicates that $\boldsymbol{F_p}$ will push electrons along and away from the optical axis. In the non-linear regime, the ponderomotive force can be derived from the electron momentum equation for relativistic momentum. In terms of the normalized momentum $\boldsymbol{u} = \boldsymbol{p}/(m_e c)$, and the relativistic correction factor $\gamma = (1 - \boldsymbol{u}^2)^{-1/2}$, the generalized non-linear ponderomotive force is

$$\boldsymbol{F_p} = -m_e c^2 \nabla\gamma.$$ (1.7)

Just as in the linear regime, it can be seen that pulses peaked in space and time will expel electrons along and transversely away from the optical axis.

After the pulse has propagated through a given region of the plasma, the electrostatic force generated by the charge separation pulls expelled electrons back towards the optical axis, forming a wave behind the pulse. In the linear regime $a_0 \ll 1$, analytical descriptions of these waves driven by the ponderomotive force of an intense laser pulse can be derived from Poisson's equation and the cold fluid equations for momentum and continuity. In a background plasma with density n_0, this gives the following equations for the density perturbation $\delta n = (n - n_0)/n_0$ and electrostatic potential ϕ [16]:

$$\left(\frac{\partial^2}{\partial t^2} + \omega_p^2\right)\frac{\delta n}{n_0} = \frac{c^2 \nabla^2 a^2}{2} \tag{1.8}$$

$$\left(\frac{\partial^2}{\partial t^2} + \omega_p^2\right)\phi = \frac{\omega_p^2 a^2}{2}, \tag{1.9}$$

where $\omega_p^2 = 4\pi n_0 e^2/m_e$ is the plasma oscillation frequency. Since $a = a(t)$ implicitly, these indicate the behavior of a driven harmonic oscillator. Eq. 1.8 shows that the density perturbation (wake) will be of comparable size to the transverse laser spot size, and Eq. 1.9 implies that wakes will be driven resonantly when the laser intensity envelope is of comparable scale to the plasma wavelength, $\lambda_p = 2\pi c/\omega_p$. For a plasma density $\sim 10^{17}$ cm^{-3}, this means that ϕ, and its corresponding electric field (the wakefield) will be resonantly driven by pulses with temporal envelopes of ~ 100 fs. We note that Eq. 1.9 also indicates the presence of transverse electric fields away from the axis. These can have a focusing effect on accelerating electron bunches, and play a role in the trapping of electrons in the wake (Sec. 1.3.3).
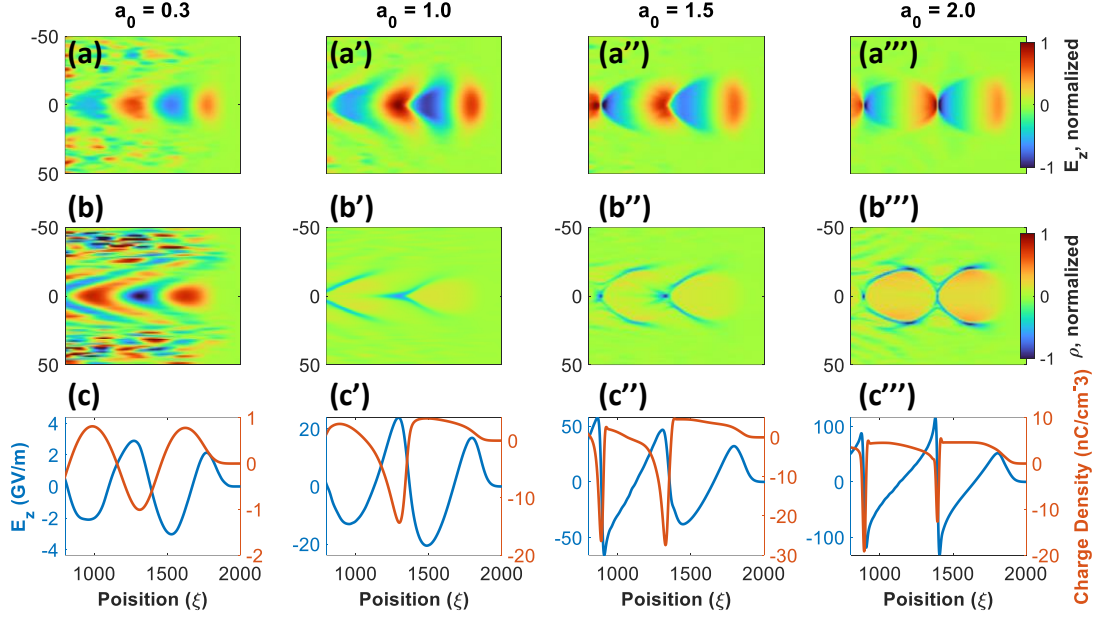
Figure 1.3: Examples of wakes and wakefields excited by drive pulses of different intensities. **(a)-(a''')** axial electric field of the wakes excited by drive pulses of different intensities. Each panel is normalized to its respective maximum. **(b)-(b''')** charge density of the driven wakes. Each frame is normalized to its maximum amplitude variation. **(c)-(c''')** lineouts of the axial electric field and charge density taken on the optical axis.

As the laser intensity increases to $a_0 \gtrsim 1$, the model of a linear perturbation begins to break down and the driven plasma waves become (highly) nonlinear. A 1D analytical solution can be found in the non-linear regime for idealized conditions, but 3D solutions are best calculated by PIC (Sec. 1.6) simulations [16,17,40].

A qualitative example of the change in the behavior between the linear, quasilinear, and non-linear regimes is given in Figure 1.3. Panels (a)-(a''') show the structure of the accelerating field, E_z, for drive pulses of different intensities. The horizontal coordinate $\xi = v_g t - z$ gives the pulse frame coordinates at a time t and position z (along the laser propagation direction) for a pulse travelling with group velocity v_g. Panels (b)-(b''') show the structure of the plasma waves driven by the pulses. The on-axis lineouts of each are plotted in panels (c)-(c'''). As a_0 increases,

both the wave structure and the fields become less sinusoidal, exhibiting less fidelity to the driven harmonic oscillator descriptions in Eqs. 1.8 and 1.9. It can also be observed that for $a_0 = 2$, the density perturbations have expelled nearly all electrons from the wake, forming complete 'bubbles' of positively charged ions surrounded by electrons. When all electrons are expelled from the wake, the bubbles become nearly circular. This highly non-linear regime is often referred to as the 'blowout' regime [40–43].

1.3.2 LWFA energy gain and scaling

Free electrons moving in phase with the wakefield will experience an accelerating electrostatic force in the direction of laser propagation. As seen in Eqs. 1.8 and 1.9, increasing the drive pulse intensity or plasma density increases the amplitude of the density perturbations and accelerating wakefields. Maximizing the accelerating field, however, does not always maximize energy gain in a LWFA.

Energy gain in a LWFA is limited by three processes: dephasing, depletion, and diffraction. Dephasing occurs when an electron bunch is accelerated beyond the group velocity of the drive pulse and moves into the region of the wake where the fields are decelerating. Electrons are considered 'dephased' when they have traversed ¼ of the plasma wavelength λ_p from the back of the wake and they have begun to experience a significantly weaker accelerating field. The laser propagation distance over which this phenomenon occurs is called the dephasing length, L_d. In the 1D limit for an idealized, resonant pulse, the dephasing length is given by

$$L_d \simeq \frac{\lambda_p^3}{2\lambda^2} \times \begin{cases} 1 & a_0^2 \ll 1 \\ \frac{\sqrt{2}}{\pi} \frac{a_0}{N_p} & a_0^2 \gg 1 \end{cases}, \tag{1.10}$$

where λ is the laser wavelength and N_p is the number of plasma periods behind the

laser pulse. Energy gain, particularly at higher electron densities ($> 10^{18}\ cm^{-3}$), can

also be limited by depletion of the laser pulse. Depletion refers to deposition of the

drive pulse energy into plasma waves and corresponds with redshifting of the pulse

frequency [16,17,44–46]. If a sufficient amount of energy deposition has occurred, the

pulse will no longer have sufficient intensity to drive the wake. Under the same

idealizations as Eq. 1.10, the scale length for depletion L_{pd} is given by

$$L_{pd} \simeq \frac{\lambda_p^3}{\lambda^2} \times \begin{cases} \frac{2}{a_0^2} & a_0^2 \ll 1 \\ \frac{\sqrt{2}}{\pi} a_0 & a_0^2 \gg 1 \end{cases}. \tag{1.11}$$

We emphasize that these scalings are derived in only one dimension. Analytic

calculations of L_{pd} and L_d in 3D will yield slightly different results [40,43], as will

including more of dynamic physical processes which are not accounted for in many

estimates. As an example of the complexity for explicitly calculating the dephasing

length, consider the following: when $a_0 > 1$, the leading edge of the drive pulse erodes

as it deposits energy into plasma waves, causing some amount of phase slippage

between the pulse and wake which depends on the plasma density. In this case, the

dephasing length can be estimated from the group velocity:

$$L_d = \frac{\lambda_p}{2} \left(1 - v_g - v_{etch}\right), \tag{1.12}$$

where v_g is the laser group velocity and $v_{etch} = (N_{e0}/N_{cr})c$ is the velocity at which

the leading edge erodes opposite of the pulse propagation due to depletion [47]. A full

12

calculation of the dephasing length from Eq. 1.12 would require acknowledging that implicitly $v_g = v_g(\xi)$, and the group velocity changes due to non-linear propagation effects [16,17,48–50]. The picture becomes even more intractable when incorporating more physical elements such as imperfect pulse and plasma density profiles. In practice, scalings such as those discussed here are best used for coarse estimations, while PIC simulations (Sec. 1.6) are required to more fully understand the detailed physical processes in LWFA.

Assuming a constant accelerating field, the energy gain ΔW before dephasing or depletion is nominally $\Delta W = eE_z L_{acc}$, where L_{acc} is the length of the accelerator. The maximum energy gain will occur when L_{acc} is equal to the shorter of either L_d or L_{pd} (in the quasilinear regime, $L_d \simeq L_{pd}$). In [40], it is found that the energy gain ΔW accounting for both dephasing and depletion scales as

$$\frac{\Delta W}{mc^2} \sim \begin{cases} a_0^2 \dfrac{\omega_0^2}{\omega_p^2} = a_0^2 \dfrac{N_{cr}}{N_e}, & a_0 \ll 1 \\[2mm] a_0 \dfrac{\omega_0^2}{\omega_p^2} = a_0 \dfrac{N_{cr}}{N_e}, & a_0 \gg 1 \end{cases} \tag{1.13}$$

where ω_0 is the laser frequency, and $N_{cr} = m_e \omega_0^2 / 4\pi e^2$ is the critical plasma density above which the plasma is opaque to light of frequency ω_0. Eq. 1.13 shows that maximum energy gain relates inversely to the plasma density. Though dephasing and depletion limit the possible energy gain for a single LWFA, staging of multiple LWFAs (similar to the many RF cavities used in conventional accelerators) has been proposed as a path to accelerate electrons well beyond the GeV level [9]. Successful staging [26] of LWFAs presents many technical challenges, and is active area of research [51] outside the scope of this dissertation.

For the low $10^{17} \, cm^{-3}$ plasma densities consistent with the energy gain of ~10 GeV desired for a potential module in a staged LWFA accelerator [9], Eq. 1.13 requires at least PW laser power in the nonlinear regime. The desired energy gain can be achieved much more efficiently in the quasilinear regime with $a_0 \sim 1$. This corresponds to a dephasing length $L_d \sim 1 \, m$. For the typical high-intensity laser pulse of waist size $w_0 < 100 \, \mu m$, this is many, many times longer than the Rayleigh range $Z_r = \pi w_0^2 / \lambda$ over which the pulse diffracts sufficiently that the waist size w_0 increases by $\sqrt{2}$.

Diffraction presents a challenge to LWFA design: the drive pulse will not remain sufficiently intense for long enough to accelerate electrons to the maximum achievable energy gain for a given plasma and laser. The solution is to use some form of optical guiding to counter diffraction and maintain the laser intensity over a long enough distance that acceleration is limited by either dephasing or depletion. Different types of optical guiding and the generation of plasma waveguides will be discussed in secs. 1.4 and 1.5.

1.3.3 Injection

Beyond exciting strong plasma waves, LWFAs require mechanisms to trap electrons in phase with the strong accelerating fields. At the simplest level, electrons inside the wake will be trapped and accelerated ('injected') if they have sufficiently high longitudinal momentum to be accelerated to a velocity greater than the wake velocity before the bucket passes by. They must also have sufficiently small transverse momentum not to escape the focusing fields from the edges of the bucket. Techniques for doing this generally fall into three categories: self-injection, density transition injection, and optical injection.

As shown in Figure 1.3, for high laser intensity ($a_0 \gg 1$), the wake density distribution becomes increasingly steep, and the electrostatic fields increasingly large. At a field strength E_{wb}, the wave breaking field strength, the amplitude of the electrostatic field generated by the wake is such the velocity of electrons oscillating according to Eq. 1.8 exceeds the phase velocity of the wake [52,53]. Those electrons moving on trajectories with suitable transverse momentum are trapped in phase with the wake and can be further accelerated by the wakefield. This process is called 'self-injection' [54]. In a thermal plasma (or one generated by the pulse itself), a portion of the electrons will have sufficient initial momentum that they can be trapped through this process even when the wakefield amplitude is below the wavebreaking threshold [55,56]. A major drawback of this technique is that it requires relativistic laser intensities which are not ideal for high energy gain LWFAs.

While self-injection relies on the electrostatic force of the wake to accelerate electrons into phase, other techniques achieve injection by controlling the wake phase velocity with tailored plasma density profiles. Downramp injection employs a gradually decreasing plasma density gradient to reduce the wake phase velocity behind the driver [57–59]. The effect is more pronounced for buckets further from the laser pulse. In the second bucket, the phase velocity of the wake becomes comparable to the motion of electrons in the plasma oscillations (as in the self-injection case), and injection occurs [57]. Injection can also be achieved with a sharp (of order λ_p) decrease in plasma density [60,61]. During the transition, the wake phase velocity dramatically slows. Electrons which may have had insufficient momentum to be trapped at the high-

density phase velocity are suddenly rephrased into the strong accelerated field of the wake and trapped.

We note that a longitudinally varied density profile may also be used to increase the overall energy gain of a LWFA. In the quasilinear regime, energy gain is limited by dephasing as accelerated electrons begin to move faster than the wake. If the wake velocity is increased, the electrons are 're-phased' with the accelerating field. In practice, this is achieved by increasing the plasma density, either with a controlled taper to lock the wake in phase with the accelerating electrons [62], or more coarsely with sharp increases in plasma density [63,64].

Several techniques have been developed which rely on laser interaction to impart electrons with the necessary momentum for injection. Many of these rely on the use of multiple pulses. Once class of approaches relies on the ponderomotive force to provide the necessary 'kick' to the electrons. This was proposed initially for a perpendicularly propagating pulse which would ponderomotively accelerate electrons in the bucket after the drive pulse. With enough acceleration in the longitudinal direction of the drive pulse, they could be trapped in the wake. However, it has been best realized when the ponderomotive force was provided by the beating of laser pulses with different frequencies [65–67]. This approach is called 'beat wave' or 'colliding pulse' injection, and has many variations and subtleties outside the scope of the work discussed here [68].

The technique used in the experiments discussed in this dissertation is ionization injection [69–72]. Ionization injection relies only on a single pulse (the LWFA drive pulse) to inject electrons into the wake. Due to shielding, inner electrons

16

of atoms require more energy to ionize than outer electrons. For OFI by an ultra-short laser pulse, this can mean that for a given working gas, the inner electrons will only be ionized by the most intense portion of the pulse. If the pulse is driving a wake, electrons born near the height of pulse will not experience sufficient ponderomotive force to expel them from the wake. Moreover, they will experience significant longitudinal acceleration from the wakefield and can be trapped before slipping out of the wake.

In order for maximum trapping to occur, most of the inner-shell ionization must occur near the maximum of the wake potential. This is the case for resonantly driven wakefields: $c\tau \simeq \lambda_p$, where τ is the timescale of the pulse. When the drive pulse is much shorter than the plasma length some injection is still possible. Tunnel-ionization of off-axis inner shell electrons which were not previously ionized via OFI at the crest of the pulse may be able to obtain sufficient longitudinal momentum for trapping. A highly simplified cartoon is shown in Figure 1.4. From the same PIC simulations as Figure 1.3, an off-resonant drive pulse E_{short} drives a wake with the accelerating field E_{wake} and corresponding electrostatic potential Ψ_{wake}. Even though the amplitude of the short pulse is well over the OFI threshold (green line), very few electrons will be born at a location with suitable potential for trapping (the dashed black lines denote the minimum potential for trapping). A weaker, resonant pulse (dashed red line), however, will ionize inner shell electrons at a much more suitable location for trapping. We note that this schematic does not include the change in the wake structure excited by the resonant pulse.
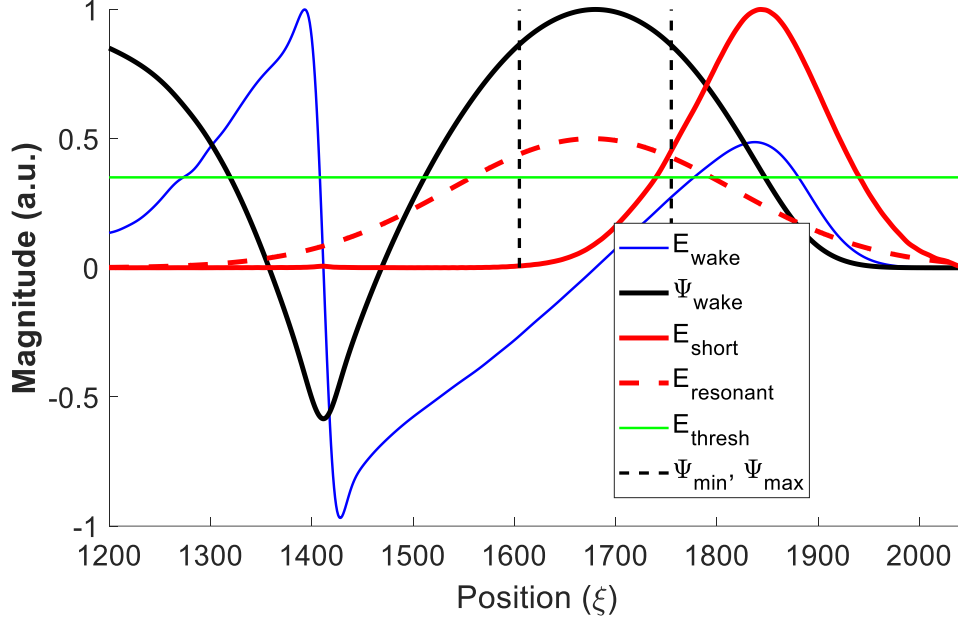
Figure 1.4: Plots of important quantities for ionization injection. A wake with accelerating field E_{wake} (solid blue line) and corresponding potential Ψ_{wake} (solid black line) is driven by an ultrashort laser pulse (E_{short}, red line) which is shorter than resonant: $c\tau_{short} < \lambda_p$. E_{short} is well above the threshold for OFI, E_{thresh}(solid green line). However, most electrons born during the pulse are outside of the trapping region between Ψ_{min} and Ψ_{max} (dashed black lines), and will not gain suitable longitudinal momentum to be trapped in the wake. On the other hand, a weaker, but resonant pulse, $E_{resonant}$ (dashed red line), will ionize many electrons in the trapping region. E_{wake}, Ψ_{wake}, and E_{short} are taken from the same simulations as Figure 1.3. However, Ψ_{min}, Ψ_{max}, E_{thresh}, and $E_{resonant}$ are artificial and added for conceptual clarity.

These different injection phenomena do not necessarily happen in isolation. Ionization injection has been shown to enhance shock injection [73], and nonlinear pulse evolution may enable different types of injection as the laser intensity increases and decreases [74]. In Chapter 4, we will discuss in particular how different phases of linear and nonlinear pulse propagation can induce and suppress ionization injection, and how this behavior can be used to better control ionization injection.

18

1.4 Plasma waveguide theory

The high laser intensities ($> 10^{18}$ W/cm^2) required for LWFA necessitate that ultra-high power ($> .1$ TW) laser pulses are focused to small (<100 μm) beam sizes. Focusing of a finite aperture beam leads to diffractive spreading after the focus. For a Gaussian beam, this spreading is characterized by the Rayleigh range, Z_r over which w_0 increases by $\sqrt{2}$ and the intensity halves. Diffraction presents a significant barrier to efficient LWFA, which requires that pulses maintain constant high-intensity over distances many times the Rayleigh length. For example, to reach dephasing-limited energy gain in a plasma with density $1 \times 10^{17}\ cm^{-3}$, a pulse with intensity $a_0 \sim 1$ and waist size $w_0 = 45\ \mu m$ must remain focused for $\sim 1\ m$, more than 100 Rayleigh lengths.

In general, diffraction can be countered with a focusing refractive index profile (a local maximum in the index corresponding to the center of the laser mode). For a Gaussian beam with Rayleigh range Z_r, the beam curvature leading to diffraction can be exactly cancelled by a graded index of refraction when

$$\Delta n = \frac{1}{kZ_r},\tag{1.14}$$

where Δn is the difference in the index of refraction between the center of the beam and at the waist and $k = 2\pi/\lambda$ [75]. A waveguide extends this profile over a long propagation distance, enabling transmission of the beam over many Rayleigh ranges.

We note that the exact index profile required to counter diffraction will vary for different beam shapes. In general, for a given index profile, the beam shapes for which diffraction balancing occurs are called the modes of a waveguide. Certain index profiles

may not be capable of sustaining any modes (for instance if the condition in Eq. 1.14 is not met), while others may sustain many. We will discuss techniques for finding the modes of a given waveguide in Sec. 1.4.2. For low intensity beams, waveguides can be formed with special glass strands in fiber optic cables [76], dielectric chips [77], or photonic crystals [78]. Fiber optics in particular are widely used to enable the transmission of information encoded in laser modes over long distances. One common class of fiber optics uses a stepped index profile: a high index core surrounded by a low index cladding. Throughout this dissertation we will use the core/cladding terminology to refer to high and low index portions of a waveguide, even when the transition between the two is continuous. Unfortunately, for the ultra-high intensity pulses needed for LWFA and other relativistic laser-plasma interaction, the damage thresholds for solid waveguides are far too low, requiring different waveguide solutions. Since the ultimate goal is to study laser-plasma interaction, plasmas are a natural choice of medium for high-intensity waveguides. In a plasma, guiding of intense laser pulses can be achieved either through relativistic self-focusing or with the use of a preformed plasma channel.

1.4.1 Relativistic self-guiding

At sufficiently high power, electron quiver velocities in the laser electric field become significantly relativistic. This effect introduces an intensity-dependent term to the index of refraction $n = n_0 + n_2 I$, where n_2 is the nonlinear index of refraction. In practical units, for a Gaussian pulse, we can define the critical power [79]:

$$P_{sf} \simeq 17.4 \frac{N_{cr}}{N_e} \ (GW) \tag{1.15}$$

as the power for which the intensity-induced curvature in the index of refraction is sufficient to counter the natural diffraction of the beam. If the laser power can be maintained during propagation, then the pulse can self-guide over many Rayleigh ranges [24,41,42,80,81]. For longer pulses ($c\tau \geq \lambda_p$), the density perturbations introduced by the ponderomotive displacement of electrons can also provide a focusing effect for later parts of the pulse [48,50,82–85]. The process is complicated by pulse erosion due to diffraction of the leading edge and energy deposition into plasma waves [16,17], as well as ionization induced diffraction [80]. But these can be mitigated with sufficient laser energy, temporal phase shaping, and tuning of the focal location with respect the gas distribution. At PW laser powers, self-guiding has enabled acceleration of electrons to the GeV level [24,81]. Self-guiding has also enabled LWFA with sub-terawatt pulses [86], and is necessary for LWFAs driven by kHz lasers with limited pulse energy [87,88]. The effects of ponderomotive plasma modification by short ($c\tau < \lambda_p$) pulses within a plasma waveguide will be discussed further in secs. 1.4.3 and 4.2.4.

1.4.2 Pre-formed plasma waveguides and leaky modes

For the low densities (10^{17} cm^{-3}) desirable for multi-GeV LWFA, Eq. 1.15 indicates that relativistic self-guiding requires >PW power. At these low densities, high energy gain LWFAs can be much more efficiently driven with lower intensity $a_0 \sim 1$ pulses and preformed plasma waveguides. In a cold plasma, the index of refraction, n, is given by

$$n = \sqrt{1 - \frac{\omega_p^2}{\omega^2}} \approx 1 - \frac{N_e}{2N_{cr}} \qquad (1.16)$$

for $N_e/N_{cr} \ll 1$, which is satisfied in all of our experiments. The relationship between index and plasma density means that plasma density profiles suitable for optical guiding should be concave.

Laser-generated pre-formed plasma waveguides are leaky to varying degrees, and their modes are quasi-bound [89,90] (see below). While excessive leakiness can lead to rapid exponential energy attenuation, a guide with a well-bound fundamental mode, but leaky higher order modes, is desirable to help regularize the laser profile for generation of well-behaved laser wakefields [91,92]. For a given waveguide profile, the leakiness of a quasi-bound mode is quantified by the $1/e$ energy attenuation length, $L_{1/e}$ [89]. For application to LWFA, the plasma waveguide should be designed to ensure that the attenuation length of the fundamental mode satisfies $L_{1/e} > L_d, L_{depl}$, the dephasing and depletion lengths in the LWFA process.

As demonstrated in [89,90], the quasi-bound mode structure and attenuation lengths for a radially symmetric plasma profile are found by solving the cylindrical Helmholtz equation for (p, m) eigenmodes, where $p = 0, 1, 2, \ldots$ and $m = 0, 1, 2, \ldots$ are radial and azimuthal indices:

$$\frac{d^2\mathcal{E}}{ds^2} + \frac{1}{s}\frac{d\mathcal{E}}{ds} + \left(n^2(s) - \frac{\beta^2}{k_0^2} - \frac{m^2}{s^2}\right)\mathcal{E} = 0 \ , \qquad (1.17)$$

where $E(r, z) = \mathcal{E}(r)e^{i\beta z}$ is the electric field, k_0 is the vacuum wavenumber, β is the longitudinal propagation number, $s = k_0 r$ is a dimensionless radial coordinate, and $n(s)$ is the refractive index profile corresponding to the plasma profile. For an infinite

22

parabolic plasma density profile $N_e(r) = N_{e0} + \Delta N_e(r/r_0)^2$, where N_{e0} is the on-axis plasma density, r_0 is the scale width, and $\Delta N_e = N_e(r_0) - N_{e0}$, Eq. 1.17 reduces to the associated Laguerre equation [89,90]. The solutions are the Laguerre-Gauss (LG) modes:

$$E_p^m(r, \phi, z) = A_p^m e^{-r^2/w_{ch}^2} \times \left(\frac{2r^2}{w_{ch}^2}\right)^{m/2} \times L_p^m\left(\frac{2r^2}{w_{ch}^2}\right) \times e^{im\phi} \times e^{i\beta_p^m z}. \qquad (1.18)$$

In Eq. 1.18 A_p^m is a normalization constant, $w_{ch}^2 = r_0/\sqrt{\pi r_e N_{cr}}$, is the channel mode size, $r_e = e^2/m_e c^2$ is the classical electron radius, L_p^m is the Laguerre polynomial of radial order p and azimuthal order m, and β_p^m is the longituindal wavenumber associated with the (p,m) mode:

$$\beta_p^m = (k_0^2 - 4\pi r_e N_{e0} - 4(2p + m + 1)/w_{ch}^2)^{1/2}. \qquad (1.19)$$

Differentiating Eq. 1.19, we see that different modes will propagate with different group velocities dependent on their mode numbers [89,93]:

$$v_g = \left(\frac{\partial \beta_{p,m}}{\partial \omega}\right)^{-1} = c\left[1 - \frac{N_{e0}}{2N_{cr}} - \frac{2}{kw_{ch}^2}(2p + m + 1)\right]. \qquad (1.20)$$

For a given waveguide, the higher order modes will propagate more slowly than low order modes. And for different waveguides, those with smaller w_{ch} and higher on-axis plasma density will have slower mode propagation velocities. As will be discussed in more detail in Chapter 4, this can mean that under certain waveguide and pulse conditions, energy coupled into different modes at the start of the guide can spatially separate over long propagation distances.

Though Eqs. 1.18-1.20 are only exactly true for an infinite parabolic channel, they will be very close approximations nearly parabolic, finite width channels. In the

case of a finite parabolic channel with a maximum plasma density at some radius r_m, it is possible to derive a cut off condition for the number of higher order modes sustained by the waveguide dependent on the channel depth, $\Delta N_e(r_m)$ [89,94]:

$$\Delta N_e < \frac{(2p+m+1)^2}{\pi r_e r_m^2}.$$

(1.21)

We note that the bound modes of a plasma waveguide are wavelength independent. The structure will be slightly different since $w_{ch}^2 \sim N_{cr}^{-1/2}$, but the same number of radial azimuthal modes will be bound for different wavelengths. For a real plasma waveguide, the plasma density in the region $r > r_m$ quickly drops to zero, and the solution to Eq. 1.17 dictates a superposition of inward and outward propagating conical waves [89,90]. As a mode propagates through the waveguide, energy will leak out of the channel region into these radiating waves. The modes of plasma waveguides are thus considered 'quasi-bound', though when ΔN_e and r_m are sufficiently large, the leakage is minimal and the resulting modes are sometimes referred to as 'bound'.

For increasingly less parabolic channels, fidelity of the waveguide modes to Eq. 1.18 decreases, as does the accuracy of Eqs. 1.19-1.21. The quasi-bound modes will, however, still be characterized by radial and azimuthal mode numbers (p, m), and they can be identified computationally with a method described in [89,90]. We solve Eq. 1.17 for a range of $\beta' = \beta/k_0$ for a fixed azimuthal mode number m and use the $\mathcal{E}(r)$ solutions to compute the resonance function $\eta(\beta') = (|\mathcal{E}_{vacuum}|^2 A)^{-1} \int_A |\mathcal{E}|^2 dA$, where $\mathcal{E}_{vacuum}$ is the vacuum solution and A denotes the waveguide cross-section. If there are any bound modes for a given m, $\eta(\beta')$ will have a maximum at the corresponding longitudinal wavenumber, β'. All radial modes, p, will be identified by

this process, assuming that the range of the β' is large enough and the sampling frequency is sufficient to resolve the resonances. As shown in Eq. 1.19 for a parabolic profile, the $\eta(\beta')$ maximum at the largest β' corresponds to the $(p = 0, m)$ mode, with the maxima at decreasing β' corresponding to the $p = 1,2,3, \dots$ modes. Further information can be extracted from peaks in the η resonance. The full width at half maximum, $\Delta\beta$, of the resonance peaks around these maxima gives the attenuation length of each mode: $L_{1/e} = 2\pi/\Delta\beta$ [89]. The attenuation length generally increases for larger ΔN_e and w_{ch}, and for a given plasma profile, is always longer for modes with higher propagation numbers.
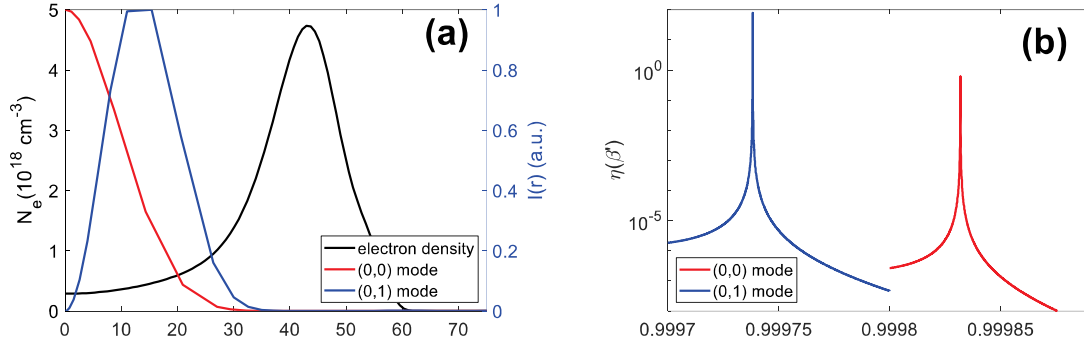
Figure 1.5: Example of quasibound mode calculation. **(a)** normalized (0,0) and (0,1) modes (red and blue lines) corresponding to the given plasma density profile (black line). **(b)** $\eta(\beta')$ resonance curves corresponding to each of the bound modes in panel (a). The plasma profile corresponds to the waveguide with on axis density $N_{e0} = 3.2 \times 10^{17} cm^{-3}$ generated in the experiments discussed in Chapter 3.

This process is illustrated in Figure 1.5(a), were we find the (0,0) and (0,1) modes for the plasma density profile plotted by the black curve in. In panel (b), the plot of $\eta(\beta')$ shows resonance peaks corresponding to these modes. The fundamental mode has a larger longitudinal propagation number than the $m = 1$ mode (and also a higher group velocity). However, both have long attenuation lengths $L_{1/e} \sim 2\,m, 1\,m$ for the (0,0) and (0,1) modes respectively [22]. This means that both modes will be

copropagating through the guide. Superposition of the fields propagating in the longitudinal direction with different wavenumbers β_j and β_k leads to interference called 'mode beating'. Mode beating is periodic with a spatial period $\Lambda = 2\pi/(\beta_j - \beta_k)$. The interference between the two modes causes oscillations in the maximum laser intensity and the electric field profile, both of which can have a significant effect on LWFA by altering the geometry and phase velocity of the wakes. When designing plasma waveguides for LWFA, the goal is to operate in a parameter space where $L_{1/e} \sim L_d$ for the fundamental mode, but $L_{1/e} \ll L_d$ for higher order modes to minimize the effects of mode beating. Chapter 4 will explore mode beating in LWFAs in more detail.

1.4.3 Propagation of relativistic pulses in waveguides

Thus far, we have only considered linear propagation in a plasma waveguide. For $a_0 \gtrsim 1$ drive pulses, it is important to consider non-linear propagation effects which may alter the guiding process. As an example, consider a long $(c\tau > \lambda_p)$ pulse propagating in a matched parabolic channel $N_e(r) = N_{e0} + \Delta N_{em}(r/w_{ch}^2)$. If the power is sufficiently high, $P \gtrsim P_c/4$, then the beam will experience a significant enough relativistic modification of the index for self-focusing to affect the guiding. This in turn alters the density channel requirements for matched guiding. In [95,96], it is shown that for a long pulse with $P/P_c < 1$, the required channel depth ΔN_e is less than the low power case, with $\Delta N_e/\Delta N_{em} = 1 - P/P_c$. If the pulse is sufficiently intense to ponderomotively excite plasma waves, then an additional term accounting

for the local density curvature of the plasma wave must be added to the index of refraction [48,84,85].

In practice, the guiding effects of non-linear pulse evolution are extremely difficult to model analytically. For ultrashort LWFA drive pulses ($c\tau \leq \lambda_p$), the amount of self-focusing and the plasma wave structure can vary significantly throughout the pulse, and the above modifications to the required waveguide structure are different for different parts of the pulse [48,82]. The modified matched propagation conditions are further complicated by self-steepening of the laser pulse, and erosion of the pulse head from exciting plasma waves. In the commoving coordinate of the pulse ξ, this means that the matched spot size varies throughout the pulse: $w_{ch} \rightarrow w_{ch}(\xi)$. In [97], it is shown that in the paraxial regime (neglecting self-steepening, pulse erosion, and ponderomotive modification of the guiding structure), matched guiding could be achieved by tailoring the waist size of the pulse: $w_0 \rightarrow w_0(\xi)$. It was also demonstrated that quasi-matched guiding could be achieved in a quartic channel with appropriate depth.

Matched propagation becomes increasingly difficult for more intense ($a_0 > 1$) pulses, where the pulse itself evolves dramatically during propagation and the ponderomotive modification of the waveguide is significant. We will look at this regime in more detail in Chapter 4. Another benefit of operating in the quasilinear regime ($a_0 \sim 1$) identified as optimal for high energy gain LWFA is the suppression of these non-linear effects and better conditions for matched guiding.

1.5 Generation of pre-formed plasma waveguides

Many different techniques have been developed to form plasma waveguides [98]. We will give an overview of the most successful approaches and introduce two techniques developed at the University of Maryland which enable the optical generation of meter-scale plasma waveguides suitable for multi-GeV LWFA.

1.5.1 Waveguides generated by the hydrodynamic evolution of a laser-ionized plasma

The first plasma waveguides were demonstrated at the University of Maryland in the 1990s [75,94,99,100]. These employed a 100 ps duration J_0 Bessel beam to ionize and heat a gas target to plasma densities $\sim 10^{19}$ cm^{-3} and temperatures ~100 eV. The long pulse duration promoted inverse Bremsstrahlung (IB) plasma heating. The ionization and heating were primarily driven by the high intensity central maximum of the J_0 beam, of radius $r \approx 1$ µm for the refractive glass axicon used which had an approach angle $\gamma = 25°$ (see Sec. 2.2). For a beam of radius R_b incident on the axicon, and axicon inner hole radius a_h (to allow injection of a driver pulse into the waveguide), the J_0 beam focus extended a distance $L_{focus} \approx (R_b - a_h)/\tan \gamma \sim 1$ cm, to form a ~ 1 cm long, hot, narrow plasma column that drove a cylindrical blast wave [100] in the surrounding gas as it expanded, forming the radially increasing plasma density profile needed for a plasma waveguide structure. In close analogy to a traditional graded index optical fiber [101], the radially increasing plasma density profile corresponds to a radially decreasing refractive index. Extending the analogy to a step-index fiber, the central region of the plasma acts as the waveguide 'core' region and the shock region performs the function of the 'cladding'. It is important to note that waveguides formed

28

this way necessarily have a coupling between the channel width and wall height, constraining the possible on-axis density for a given laser spot size.

For plasma waveguides in the density range of interest for multi-GeV LWFA acceleration ($\sim 10^{17}$ cm^{-3}), IB heating is orders of magnitude less efficient, as its rate is proportional to N_e. This means that additional heating is required to implement hydrodynamically generated waveguides with electron densities $\sim 10^{17}$ cm^{-3}. Several techniques were developed to improve the heating efficiency including use of an initial femtosecond laser pulse [102] for ionization and the use of clustered gases [103–105] which can be heated by femtosecond laser pulses. Unfortunately, none of these were able to efficiently reach the desired on-axis plasma densities over meter-scale distances.

Optical field ionization (OFI) [35] with femtosecond laser pulses has been explored as a method for hydrodynamic plasma waveguide formation [25,93,106–112] due to the fact that ionization of the working gas depends only on laser intensity and not on local gas density. OFI also significantly reduces the laser energy requirement compared to IB to reach fully ionized hydrogen, for example. The obstacle for relying solely on OFI as a heating mechanism is that electron temperature $k_B T_e$ in the OFI process is limited to approximately the ponderomotive energy U_p in the laser field at the ionization threshold of the gas, $k_B T_e \sim U_p = 9.3 \times I(10^{14}$ W/cm$^2)\lambda(\mu m)^2$. For hydrogen, the ionization threshold intensity is $I \sim 10^{14}$ W/cm^2 and $\lambda = 0.8$ μm for the Ti:Sapphire lasers typically used, giving $k_B T_e \sim 10$ eV, an order of magnitude lower than in the IB case. This results in an insufficient pressure gradient to drive the radial shocks needed to form a strongly confining waveguide with a sufficiently thick cladding [93,106].

1.5.2 Capillary discharge plasma waveguides

An alternative approach for generating plasma waveguides, capillary discharge [113,114], has been used successfully in LWFA experiments [115,116]. The plasma is formed by electric discharge and resistive heating along the axis of a long hydrogen-filled dielectric tube, typically formed from ceramic or sapphire. In the quasi-steady state phase of the discharge under plasma pressure equilibrium, the high temperature on the capillary axis and the lower temperature at the inner wall forms a plasma waveguide structure with low plasma density on axis and high density at the wall. Typical central waveguide densities are $N_{e0} > \sim 5 \times 10^{18}$ cm^{-3}. To further reduce N_{e0} to the $< 10^{18}$ cm^{-3} range needed for multi-GeV LWFA, a nanosecond laser IB heater pulse has recently been injected into a 20 cm long capillary discharge guide [23,117]. Nonetheless, capillary discharge waveguides still present multiple limitations for the development of high repetition rate LWFAs: (1) discharge-induced capillary erosion and laser damage, (2) lack of flexible control over the density, and waveguide structure (both transversely and longitudinally), limiting control over the guiding properties and LWFA process, and (3) lack of diagnostic access to the plasma waveguide structure and to the guiding and acceleration processes inside the capillary. A visual comparison of the style of discharge capillary used in [23,116] and the style of supersonic jet used by our group in [22,93,106] is shown in Figure 1.6.
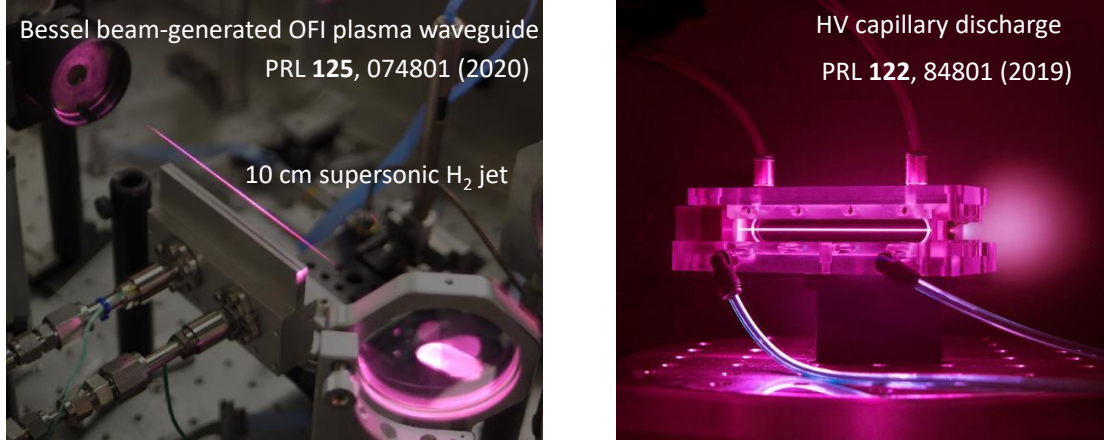
Figure 1.6: Comparison of plasma waveguides generated above a supersonic gas jet (left) and in a discharge capillary (right).

1.5.3 Plasma waveguides generated by ionization of tailored neutral gas density profiles

Two new laser-based methods [93,106] bypass the main limitations of capillary discharge waveguides: (1) Solid material structures are eliminated from the vicinity of plasma waveguide generation, especially using our novel meter-scale supersonic gas jets [93,106,118], eliminating plasma- and laser-induced damage and enabling high repetition rate operation, (2) OFI is used to generate the waveguide, a process that is density independent, and allows multiple laser pulses to separately "imprint" the waveguide core and cladding independent of longitudinal structure introduced by the gas jet, and (3) The free-standing waveguide structure enables unlimited diagnostic beam and imaging access to the full length of the plasma waveguide.

In both waveguide generation methods, the waveguide core is generated by a J_0 pulse sufficiently intense ($> 10^{14}$ W/cm^2 in the central peak) to generate a plasma column via OFI. Although an OFI-generated plasma column is not hot enough to generate a cylindrical plasma shock of sufficient amplitude to serve as a low loss plasma cladding (which had led to very weak guided laser confinement, with leakage attenuation lengths ~1 cm [93,106,107,110,112]), as it expands it drives a cylindrical

31

shock in the neutral gas at the plasma periphery. As this expansion proceeds, the on-axis plasma density drops by up to $\sim 10 \times$, with N_{e0} decreasing well below the initial hydrogen atomic density. We call this low density plasma core surrounded by a higher-density neutral gas the 'prepared index structure'. Our two methods discussed below differ by how the neutral gas is ionized to form the waveguide cladding.

Figure 1.7(a) plots the evolving plasma and neutral density profiles as a function of delay after ionization by a 75 fs FWHM J_0 pulse with mean intensity $\sim 4.9 \times 10^{15}$ W/cm^2 in the central maximum. The general form of the prepared index structure, a low density plasma core surrounded by a higher density neutral cylindrical shell, is well predicted by simulations [93], which show that the shell expands steadily at the local speed of sound, $c_s = (\gamma_s k_B T_g / m)^{1/2} \sim 7 \times 10^5$ cm/s , where $\gamma_s = c_p / c_v$ is the ratio of specific heats, T_g is the hydrogen gas temperature (elevated by conduction from the adjacent few eV plasma), and m is the H$_2$ molecular mass. The plasma and neutral expansion radii, as well as electron temperature, are plotted in Figure 1.7(b). Delaying the ionization of the outward propagating shell increases the waveguide core radius while minimally affecting the difference between core and cladding plasma densities, enabling control of the guided mode size.
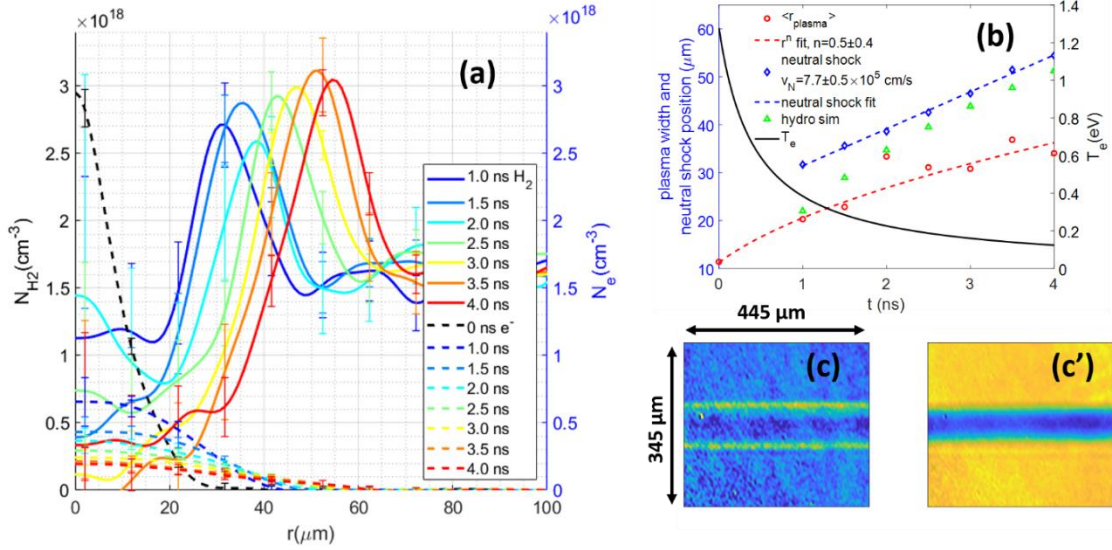
Figure 1.7: Expansion of the plasma and neutral gas around a plasma column ionized by a J_0 Bessel beam. **(a)** Hydrogen plasma and neutral gas profiles measured by two color interferometry [93] as function of delay after on-axis plasma generation by a 75 fs FWHM 100 mJ pulse with mean intensity 4.9×10^{15} W/cm^2 in the central maximum. The expansion of the neutral shell is nearly constant at $v_N \sim 7.7 \times 10^5 \ cm/s$. The neutral gas density profiles at different delays are plotted as solid lines (left axis scale) while the electron density profiles are plotted as dashed lines (right axis scale). **(b)** J_0 -induced rms plasma column radius (red circles) and neutral shock position (blue diamonds) with r^n plasma expansion fit (red dashed line) and constant $v_N \sim 7.7 \times 10^5 \ cm/s$ neutral expansion fit (blue dashed line). Calculated electron temperature (black line) and shock expansion (green triangles) from hydrodynamic simulation are also shown. **(c)-(c′)** Sample results from two-color interferometry of 'refractive index structure' induced by J$_0$ pulse. (c) Phase shift profile of neutral hydrogen, showing neutral shock at outside. (c′) Phase shift profile showing accompanying central plasma column.

The dashed curves in Figure 1.7(a) and sample transverse interferometry in Figure 1.7(c)(c') show that electron density expands from a peaked profile to a rather flat profile surrounded by a sharply rising neutral density shell. Once subsequent ionization of the neutral gas occurs, the overall plasma structure has a refractive index profile reminiscent of a step index optical fiber. For a step-index fiber, the fundamental mode radius is $w_{ch} \approx a(0.6484 + 1.619V^{-3/2} + 2.879V^{-6} + \cdots)$, where a is the core radius, k is the laser wavenumber, and $V = ka(n_{core}^2 - n_{cladding}^2)^{1/2}$ is the step index

fiber parameter [119]. For a plasma waveguide approximated as a step index fiber, $V = a(4\pi r_e \Delta N_e)^{1/2}$, where r_e is the classical electron radius and $\Delta N_e = N_e^{cladding} - N_e^{core}$ is the difference between the cladding and core plasma densities [106]. In general, the behavior of waveguides generated by of ionization the neutral shell around an expanding J_0 generated plasma will have characteristics that fall somewhere between the step-index and parabolic channel models.

In the two-Bessel method, the neutral gas outside the plasma core is optical field-ionized by a time-delayed higher order $J_{q>0}$ Bessel beam pulse whose maximum intensity ring overlaps the expanding neutral shell for a given delay. In effect, the J_q pulse imprints the plasma cladding around the core, producing a fully ionized plasma waveguide. For a fixed Bessel approach angle γ (see Sec. 2.2), a larger radius ring requires increased Bessel order q, or for fixed Bessel order q, a smaller γ will give a larger ring. In general, for small γ and $q > 1$, the radial position $r_{q,peak}$ of the intensity maximum of a J_q beam is $kr_{q,peak} \sin\gamma \approx 1.03q + 1.44$ [93]. Figure 1.8 shows varying w_{ch} obtained by changing $r_{q,peak}$ in plasma waveguides formed with the two-Bessel method. The choice of gas density in the jet, the values of axis approach angle γ and order q of the high order Bessel beam, and the post-J_0 delay of the J_q pulse are all 'knobs' for controlling the guided mode size w_{ch} and group velocity v_g of the LWFA driver pulse.
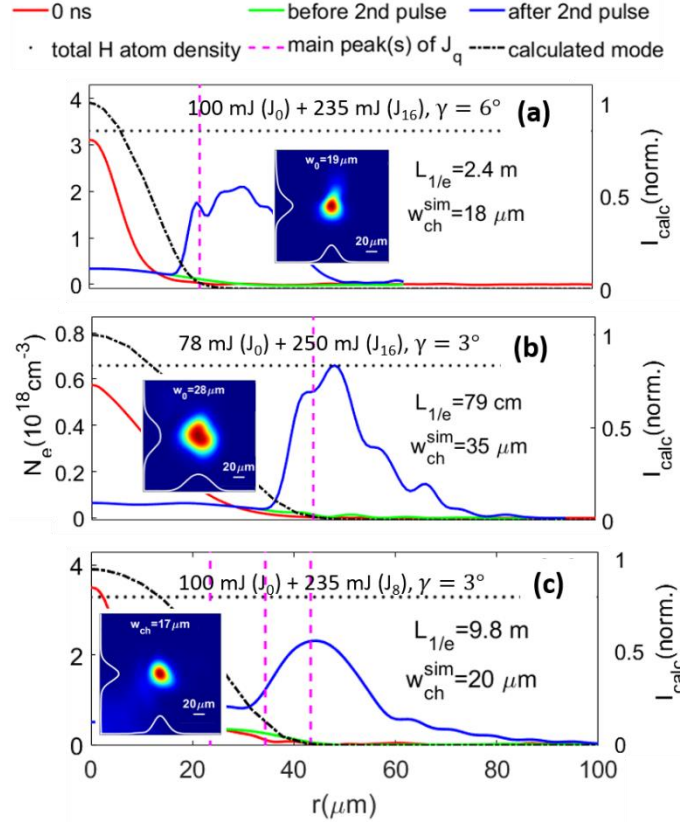
Figure 1.8: Plasma density profiles and guided modes from the two-Bessel method. **(a)-(c)** Measured density profiles generated using q^{th} order Bessel beams with varying position $r_{q,peak}$ of the maximum intensity ring, obtained by varying q and approach angle γ. The solid blue curves plot the density profiles after ionization of the neutral shell by the J_q pulse. The red and green curves plot the initial plasma column formed by the J_0 pulse, and the expanded plasma column immediately before passage of the J_q. The dashed pink line corresponds to the location of the first J_q maximum. The dash-dot black curve and w_{ch}^{sim} represent the calculated fundamental mode of the given plasma density profile [89] and $L_{1/e}$ is the calculated $1/e$ attenuation length of the guided mode. The dotted line denotes the background atomic density of the neutral gas. The insets in each panel are representative guided modes measured after propagation in (a) 15 cm, (b) 30 cm, and (c) 30 cm guides at the given conditions.

The self-waveguiding method relies on the drive pulse itself to ionize the neutral shell [93]. For a sufficiently intense pulse injected end-on into the refractive index structure, the radial wings of the pulse's leading edge field-ionize the neutral shell, generating the waveguide cladding for the remainder of the pulse. In effect, the drive pulse generates its own plasma cladding on the fly. This is seen in Figure 1.9(a),

which shows a snapshot from a PIC simulation (Sec 1.6, [120]) of a relativistic pulse self-waveguiding through a prepared index structure in hydrogen. Here, the injected 40 fs pulse has peak $a_0 = 0.3$ (corresponding to intensity 1.9×10^{17} W/cm^2) and its spot size is chosen to match the lowest order mode size of the self-waveguiding-generated plasma waveguide.

In practice, w_{ch} can be selected to match w_0 by adjusting the delay between the J_0 pulse and the self-waveguiding pulse injected into the refractive index structure. An example of the effect of $w_0 \neq w_{ch}$ on self-waveguiding is shown in Figure 1.9(b), which plots peak intensity vs. propagation distance for three mode sizes with $a_0 = 0.37$ injected into a waveguide with $w_{ch} = 20$ μm. Here the simulation code used is YAPPE [93]. This in-house code is based on the unidirectional pulse propagation algorithm [121] and gives good physical insight into propagation for $a_0 < 1$, where there are negligible relativistic effects and plasma wave excitation. The intensity oscillations for the non-matched injected beams are caused by beating of the lowest order and first order radial modes [89,93], an effect directly measured by imaging periodic intensity variations in plasma fluorescence after transmission of the self-waveguiding pulse (Sec. 2.4.2). Figure 1.9(e) shows an example of these oscillations from self-waveguiding of an 88 mJ pulse over a 10 cm long prepared index structure. In [93], the measured frequency of $2.3 \ cm^{-1}$ is shown to agree with the mode-beating frequency predicted in [89]. Under these conditions, the first-order mode leaks out of the guide, and the oscillations decay as the self-waveguiding pulse evolves into the fundamental mode of the waveguide. For higher intensity pulses, and higher density waveguides,

$L_{1/e}$ for higher order modes can be longer than L_{guide}, resulting in multimode transmission through the guide as discussed in Sec. 1.4.2.

In Figure 1.9(b), the energy decay is caused by leading edge erosion due to energy loss at the front of the pulse from diffraction, transverse leakage, and ionization. This loss is minimal for a high-energy LWFA drive pulse [93,122], where $a_0 > 1$. For the $a_0 \sim 2.5$ pulse used in the experiments discussed in Chapter 3 and Chapter 4 [74,122], the intensity exceeded the 10^{14} W/cm^2 hydrogen ionization threshold at the neutral shell position $r = 30$ μm, 100 fs before the peak of the pulse. The minimal self-waveguiding energy cost for a high-intensity LWFA drive pulse is illustrated by the YAPPE simulation curve in Figure 1.9(b) for a mode-matched pulse with $a_0 = 2$ and $w_0 = 20$ μm, showing almost 100% transmission, neglecting damping from plasma wave generation to highlight self-waveguiding erosion alone. In practice, for the ~10 J pulses recently used in multi-GeV LWFA experiments [74,122], we estimate that the small fraction of ~140 mJ was lost in far leading edge erosion from self-waveguiding. In LWFA experiments, however, the dominant guided pulse damping effect is plasma wave excitation. We have measured and simulated up to ~90% of the laser energy directed into this channel [22].
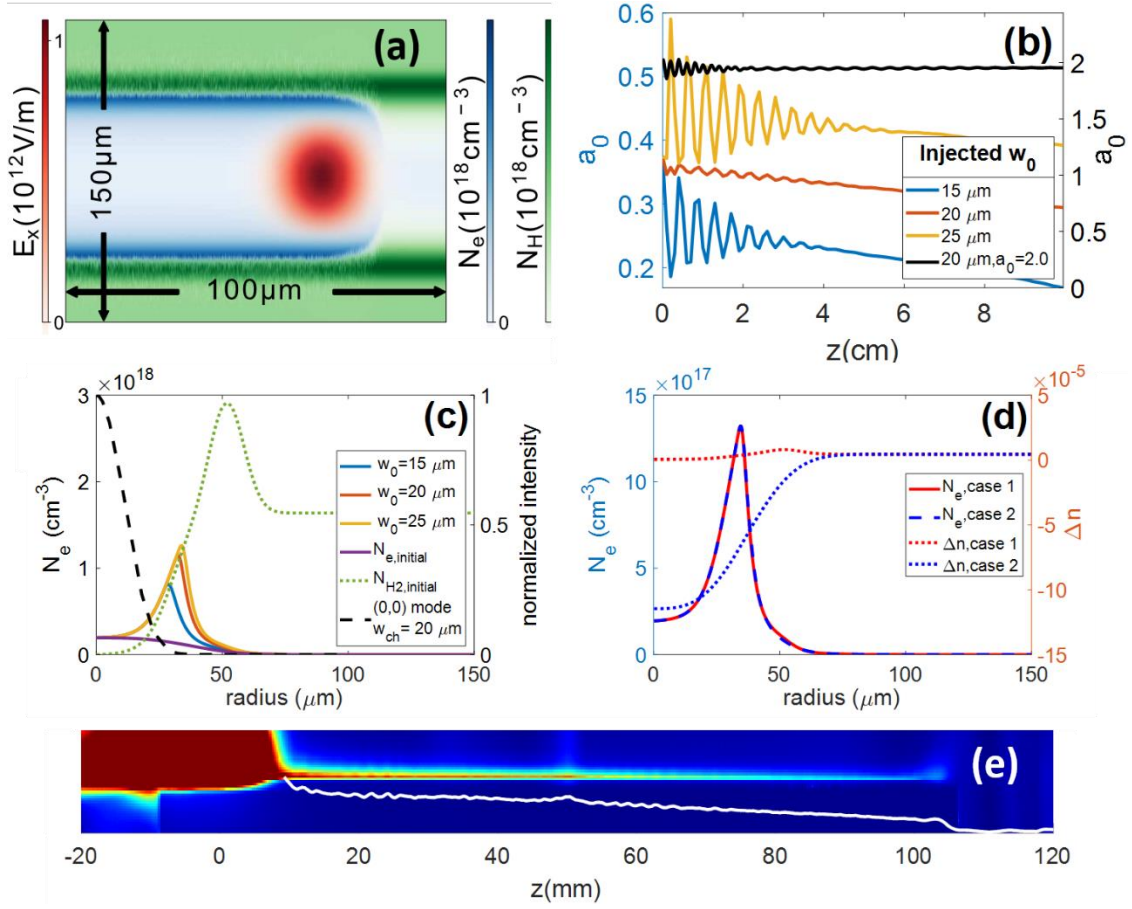
Figure 1.9: Self-waveguiding in prepared index structures. **(a)** Particle-in-cell simulation of the self-waveguiding process in hydrogen using the quasi-cylindrical code FBPIC [120] for pulsewidth 40 fs, $a_0 = 0.3$. **(b) (c) (d)** Propagation simulations ($a_0 = 0.37$) using the code YAPPE [93], illustrating (b) the effects of injection mode mismatch on the on-axis peak intensity as well as minimal energy loss from the self-waveguiding process for high intensity ($a_0 = 2$) pulses, (c) the minimal effect (at $z = 2$ cm) of mode mismatch on the downstream plasma waveguide transverse profiles after self-waveguiding, and (d) the necessary features of the prepared index structure to ensure self-waveguiding. **(e)** Imaged fluorescence profile after transmission of 88 mJ self-waveguiding pulse over 10 cm long prepared index structure, showing periodic fluorescence oscillations (column integration indicated by the white line) due to mode beating of the two lowest order guided modes. The laser is injected from the left and attenuates from self-waveguiding erosion as it propagates to the right.

Figure 1.9(c) shows that injection of pulses $w_0 \neq w_{ch}$ into the prepared index structure has little effect on the plasma waveguide generated once the mode-beating oscillations shown in Figure 1.9(b) damp out—at least when neglecting relativistic effects and ponderomotive channel modification (see Chapter 4). The necessary and

38

sufficient feature of a prepared index structure to guarantee self-waveguiding is illustrated by Figure 1.9(d): an on-axis neutral density minimum. Remarkably, neither a plasma core nor a neutral shock wall is necessary.

Measured density profiles of plasma waveguides generated by self-waveguiding pulses are plotted in Figure 1.10. Here, the injected pulse energy ranges over 11-88 mJ, the initial hydrogen density over $1.3 - 2.8 \times 10^{18}$ cm^{-3}, and injection delay $\Delta\tau_{inj}$ =1-5 ns. Figure 1.10(a) highlights the effect of varying injected pulse energy with a fixed refractive index structure. At low injected pulse energy (11 mJ), only part of the neutral shock region is ionized. As injected energy increases, the plasma density profile becomes fully ionized and converges to the underlying ion (proton) density profile. The effect of varying the initial H$_2$ density is seen in Figure 1.10(b), which shows that the radial position of the self-waveguiding-generated electron density peak is unchanged owing to the density independent expansion speed $c_s = (\gamma_s k_B T_g/m)^{1/2}$ of the neutral shell. Figure 1.10(c) shows that the waveguide structure can be modified to accommodate different mode sizes w_{ch} by varying the delay between the J_0 pulse and the self-waveguiding pulse. This allows for nearly independent tuning of the on-axis plasma density and guided mode size. We note that ionization by the wings of a guided pulse has been observed in a high density, several-millimeter long guide [123]. Early guiding results for OFI-heated plasma waveguides [107,110], which otherwise would have been quite leaky [93,106], have been more recently explained by self-waveguiding [124].

While both the two-Bessel and self-waveguiding techniques are attractive for generating highly confining, low density guides with attenuation lengths extending to

several meters and several hundred Rayleigh ranges [93,106], their different cladding formation mechanisms result in different laser energy costs per unit length of waveguide. Detailed comparisons for the two methods suggest that self-waveguiding may be more efficient for experiments requiring smaller guided mode sizes, while the two-Bessel method is more efficient for larger mode sizes [93].
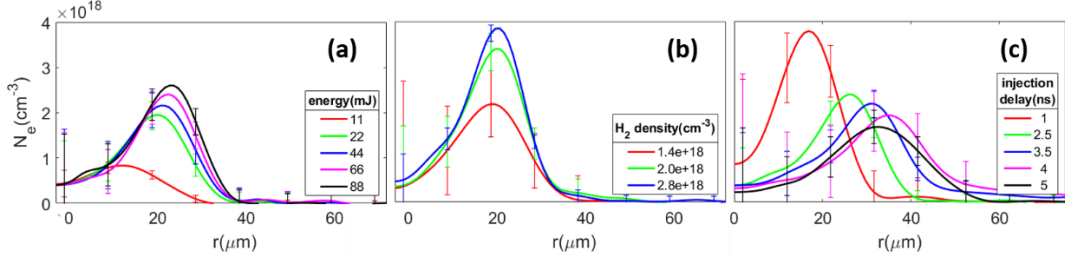
Figure 1.10: Transverse interferometry of plasma profiles generated by self-waveguiding at z = 20 cm from entrance generated by self-waveguiding pulses **(a)** of different energies injected $\Delta\tau_{inj} = 2.5$ ns after the J_0 index-structuring pulse with $N_{H2} = 1.6 \times 10^{18}$ cm^{-3} initial hydrogen density **(b)** of 88 mJ injected at $\Delta\tau_{inj} = 2.5$ ns into prepared index structure with different initial hydrogen densities **(c)** of 88 mJ injected with varied $\Delta\tau_{inj}$ intro a prepared index structure with initial $N_{H2} = 1.6 \times 10^{18}$ cm^{-3}.

1.6 Simulation methods

In this dissertation, we will primarily employ two computation techniques for studying laser evolution and LWFA dynamics. The beam propagation method (BPM, [125]) is a standard technique used to model propagation of electromagnetic waves in a medium with a linear index of refraction under the slowly varying envelope approximation. We implement a split step Fourier transform based approach which models diffraction spectrally and refraction spatially. The technique is limited to monochromatic and narrowband light, but is well suited for modelling diffraction and linear propagation through long plasma waveguides.

As discussed in Sec. 1.4, analytical descriptions of laser-plasma interaction are nearly impossible for relativistic laser intensities and physically realistic laser pulses and plasmas. This requires us to employ computational methods for solving the fluid and Maxwell's equations governing LWFA. The dominant approach for simulating intense laser-plasma interaction is through the use of PIC algorithms [126]. Computational algorithms are not the focus of this dissertation, but we will give a cursory introduction to the central ideas for the codes we have used.

There are far too many particles in even the least dense plasmas of interest for LWFA to track individual particle trajectories. And the disparate timescales of electron plasma motion and ultrashort laser pulses make traditional hydrodynamic simulations unsuitable. PIC codes solve the problem by partitioning a plasma into a collection of macroparticles on a grid. A single time step of a PIC algorithm generally has 4 key phases: calculation of the electromagnetic forces on each macroparticle (2) movement of the macroparticles according to the Newton-Lorentz equations of motion, (3) calculation the new charge and current distributions, (4) calculation of the corresponding electromagnetic fields. PIC algorithms generally require a tradeoff between accuracy and speed. Using a larger number of macroparticles reduces the likelihood of numerical instability, and using a higher grid resolution is important for modeling physics which occurs at smaller spatial scales (injection into the wake, for instance). Increasing both of these quantities can make the computational expense quite large. Improvement of the accuracy and efficiency of PIC algorithms is a crucial research area for LWFA development [127].

We employ two different codes in this work: FBPIC [120] and WarpX [128]. FBPIC (Fourier-Bessel Particle-in-Cell) enables faster computation of quasi-3D systems by implementing a PIC algorithm on a cylindrically symmetric grid. WarpX implements a PIC algorithm on a fully 3D grid. Both codes have the ability to compute particle evolution in a Lorentz boosted frame commoving with the laser pulse [129,130]. This can greatly reduce computation times required for simulating interaction over 10s of cm as in our experiments.

Chapter 2: Experimental considerations for LWFAs in meter-scale, optically-generated plasma waveguides

2.1 Introduction

Successful implementation of either of the waveguide formation techniques discussed in Sec. 1.5.3 in an accelerator relies on several key elements. In this chapter, we will discuss optical systems for generating extended plasma columns, design principles for long supersonic slit nozzles, and diagnostics for characterizing and operating meter scale waveguides. We will also discuss essential diagnostics for characterizing electron beams produced through LWFA in long plasma waveguides and their implementation in the experiments discussed in Chapters 3 and 4.

2.2 Bessel beam generation

Under the condition that solutions are of the form $E(r_\perp, z) = u(r_\perp)e^{ik_z z}$, the Helmholtz equation takes the form

$$(\nabla_\perp^2 + k_\perp^2)u(r_\perp) = 0, \tag{2.1}$$

where $k_z^2 + k_\perp^2 = k = 2\pi/\lambda = \omega/c$ are the longitudinal, perpedindicular, and vaccum wavenumbers, the vacuum wavelength, angular frequency and speed of light. Solutions of this form have the property that at different longitudinal positions $(z_1, z_2), |E(r_\perp, z_1)| = |E(r_\perp, z_2)|$, and are used to construct beams in which the field distribution is propagation invariant [131,132]. One such class of these are Bessel beams, which in cylindrical coordinates have the generalized form

$$E_\perp(r, \phi, z) = A_0 e^{ik_z z} J_q(k_r r)e^{\pm iq\phi}, \tag{2.2}$$

where for a given wavelength λ, $k_z^2 + k_r^2 = k^2 = (2\pi/\lambda)^2$ are the longitudinal and radial wavenumbers and J_q is the qth order Bessel function [133,134]. As seen in Eq.

2.2, the intensity $I \sim |E|^2$ is independent of longitudinal position (z). When viewed geometrically, the Bessel beam has the unique property that all the rays forming the beam approach the propagation axis at the same angle

$$\gamma = \arctan k_r / k_z. \tag{2.3}$$

Because of this property, even if the focus is obstructed at a certain longitudinal position, the focus can reform further along in the propagation. This has led some researchers to refer to Bessel beams as 'self-healing'[135].

A Bessel beam described exactly by Eq. 2.2 is not physically realizable since it would require infinite spatial extent (and therefore infinite energy). However, quasi-Bessel beams of finite spatial extent can be and have been generated. They are used in a wide array of fields including laser machining [136,137], optical coherence tomography [138], optical trapping [139,140], and the generation of plasma waveguides as discussed in this dissertation. For simplicity, we will refer to these quasi-Bessel beams as Bessel beams.

Generation of Bessel beams was first achieved by placing an annular aperture at the back focal plane of a converging lens [131]. This selected from an incident Gaussian beam an annular portion of the spatial frequency spectrum where $k_x^2 + k_y^2 = k_r^2$, forming a J_0 Bessel beam. J_q beams of arbitrary order can be generated by applying a conical phase to a Laguerre-Gauss beam of azimuthal order q. This can be done with an axicon [141,142], spatial light modulator (SLM) [143], or diffractive optical element (DOE, see 2.2.1) [144,145]. For a near-field beam of radius R_b, the approximate length of the Bessel beam focal line is given by

$$L_{focus} = \frac{R_b}{\tan \gamma}. \tag{2.4}$$

If there is a hole of radius a_h in the middle of the near field (as is required for coupling a drive pulse into a plasma waveguide), then $R_b \rightarrow R_b - a_h$ in Eq. 2.4.

Different applications on different laser systems are naturally suited to different beam apertures, focal lengths, and generation techniques. Since the experiments discussed in this dissertation which require high power, large aperture beams with shallow approach angles of <10°, reflective axicons [93,106] or diffractive axicons [22,118] were the most appropriate optics. For the experiments in [22,74], we found the beamline geometry for diffractive optics easier to implement. A schematic showing the generation of a J_q Bessel beam with a diffractive axicon (Sec. 2.2.1) is shown in Figure 2.1(a).
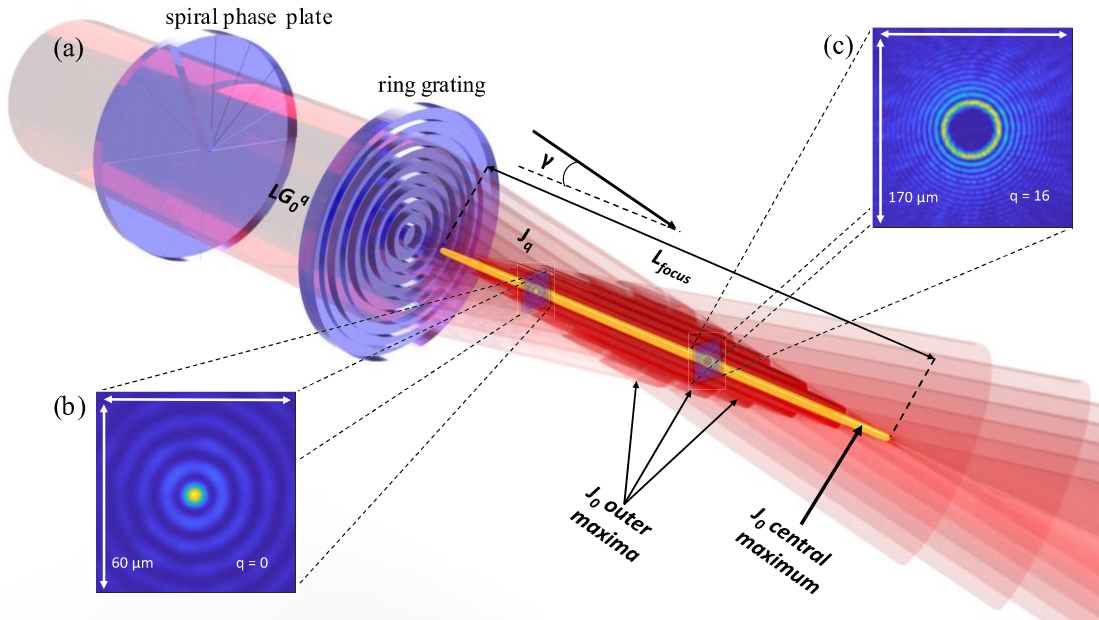
Figure 2.1: Bessel beam generation. **(a)** Cutaway schematic of Bessel beam formation. A collimated, finite aperture gaussian beam passes through a spiral phase plate (Sec. 2.2.2) and ring grating (Sec 2.2.1) to form a J_q Bessel beam. The radial phase applied by the ring grating causes each annulus of the incident beam to approach the transmission axis at an angle γ, generating the quasi-uniform, extended Bessel beam focus of length $L_{focus} \approx (R_b - a_h)/tan\,\gamma$, where a_h is the radius of a central driver beam access hole in the ring grating (not shown). **(b)**, **(c)** Measured intensity profiles of J_0 and J_{16} beams generated by this approach.

45

The cut-outs (b) and (c) show real J_0 and J_{16} profiles generated with this method.

2.2.1 Diffractive axicon design

Focusing of high-power lasers with refractive optics is generally difficult due to the non-linear focusing and temporal phase shift of the pulse inside the optic material. Reflective optics offer one solution, but have strict geometrical constraints. At a slight efficiency cost, diffractive optical elements (DOEs) enable transmissive beam geometries at high laser powers (<100 TW). Rather than applying a continuous phase $\phi(r, \theta) \in \mathbb{R}$ on an incident beam with a continuously varying surface thickness, DOEs apply the same relative phase. But they have discontinuities in the surface thickness so that $\phi_{DOE} = \text{mod}(\phi, 2\pi)$. Perfect DOE surface profiles are often impossible to accurately manufacture, but they can be approximated by discretizing the desired phase profile (and the depth of the corresponding surface features) into fixed levels [144,145]. An example of the difference in phase applied by a traditional plano-convex lens (PLCX), corresponding DOE (known as a Fresnel lens in this implementation), and a discretized DOE are shown in Figure 2.2.
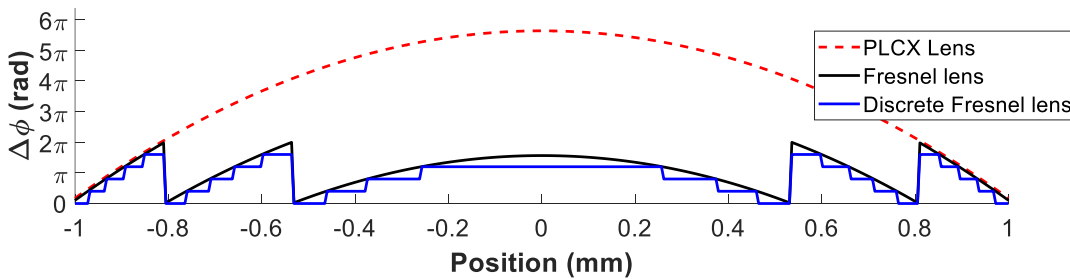
Figure 2.2: Comparison of phase applied by a traditional PLCX lens, Fresnel lens, and discretized Fresnel lens. The applied phase corresponds to an NBK-7 ($n \approx 1.515$) lens with a focal length of 1 meter at $\lambda = 537\ nm$.

For generation of a Bessel beam, the linear radial phase applied by a transmissive (refractive) or reflective axicon can be well approximated by a radial phase profile of *N*-steps per 2π phase increase. We will call this type of DOE a 'ring-

grating', or 'diffractive axicon'. Figure 2.3(a) demonstrates the surface profiles required in a fused silica diffractive axicon for an arbitrary wavelength λ_0 and approach angle γ. A perfect implementation of linear phase required to form a Bessel beam would be difficult to manufacture. But, the 2-step and 4-step discretizations are much more feasible. We note that the radial coordinate is normalized to the effective radial wavelength, $\lambda_r = 2\pi/k_r = \sin\gamma / \lambda_0$, indicating that the relative thickness required of the DOE steps only depends on the material and vacuum wavelength, while the width of the steps depends on the desired approach angle. Figure 2.3(b) gives an example of the phase applied by a 4-step diffractive axicon for use with wavelength $\lambda_0 = 0.8\ \mu m$ and an approach angle $\gamma = 3°$.

For coarser discretization of the ideal surface profile, more light is scattered into higher orders of diffraction. For our diffractive axicon, these higher orders correspond to Bessel beams with steeper approach angles. The first order diffraction efficiency η_1 of an N-step diffractive axicon is [146,147]

$$\eta_1 = \left| sinc\left(\frac{\pi}{N}\right) \right|^2. \tag{2.5}$$

We can see that for a continuous profile, $N \rightarrow \infty$, and $\eta_1 \rightarrow 1$. The predicted first order diffraction efficiency for a 2 step phase plate is just 40.5 %, while the efficiency for 4 steps is 81% [144]. Figure 2.3(c)(d)(e) show the simulated near field profiles 1 cm after transmission of a $\lambda_0 = 0.8\ \mu m$ plane wave through a $\gamma = 3°$ diffractive axicon with a perfect linear profile (c), 2-step discretized profile (d), and 4-step discretized profile (e). All panels are normalized to the maximum intensity of (c), and the middle values of the colorbars for (c) and (d) correspond their respective maximum intensities. This indicates good agreement with the theoretical diffraction efficiency limits.
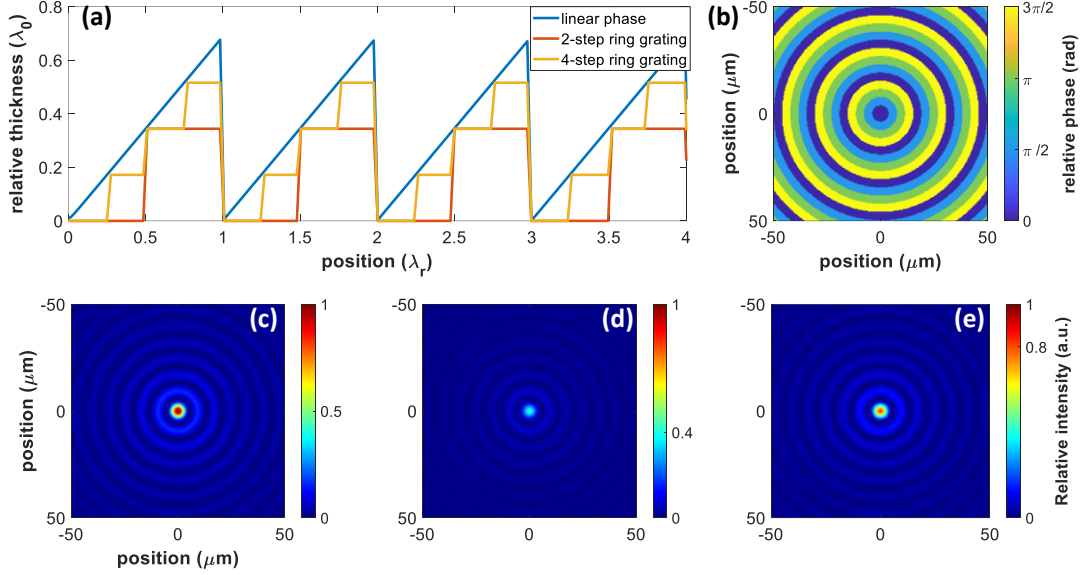
Figure 2.3: Diffractive axicon design. **(a)** possible surface profiles for a diffractive axicon made from fused silica ($n = 1.54$)..The radial position is normalized to the effective radial wavelength $\lambda_r = 1/k_r = \sin\gamma/\lambda_0$ and the thickness is normalized to the vacuum wavelength. **(b)** example of the phase applied by a 4-level diffractive axicon ($\gamma = 3°$) on a $\lambda_0 = 0.8\,\mu m$ beam. **(c-e)** BPM simulated profiles of Bessel beams generated by a $\lambda_0 = 3°$ plane wave passing through diffrative axicons with a perfect linear profiles (c), 2-step discretized profile (d), and 4-step discretized profile (e). (c-e) are normalized to the maximum intensity in (c), and the middle value on the colorbars for (d) and (e) denotes the maximum for each respective image.

The diffractive axicons and spiral phase plates used in [22,74,118] were manufactured in the FabLab at the University of Maryland, College Park through photo-lithography and plasma etching. The manufacturing process is detailed in [144,148]. Manufacturing error, most significantly alignment between the mask (which determines the phase pattern and the substrate), can also reduce diffractive axicon efficiency. For the 4-level ring gratings used in [22], we measured an efficiency $\eta_1 \simeq$ 55%.

48

2.2.2 Higher order Bessel beam generation and 'Binary' Bessel beams

In [106], the higher order LG beams required for higher order Bessel beam generation were formed by passing a zero-order LG beam through a spiral phase plate (SPP). The SPP is a DOE which applies an azimuthal phase of $2\pi q$ to the beam in Nq steps, with the phase increasing $2\pi/N$ per step. The winding direction of the phase determines the sign of q in Eq. 2.2. When $N = 2$, the winding is indeterminate, and the resulting beam can be viewed as a superposition of LG beams with azimuthal order $\pm q$. In turn, when focused with an axicon, this generates a superposition of $J_{\pm q}$ Bessel beams. Shutova *et. al.* have called this type of beam a 'binary Bessel beam' [149]. As shown in Figure 2.5 (c-d), the interference of the superimposed beams generates a nucleated focal ring with alternating regions of no intensity and double the intensity of a single J_q or J_{-q}.

These beams are potentially of interest in using the two-Bessel method in longer jets than [106]. Due to the shallow approach angle of the Bessel beams used in our experiments, longer gas jets will often block a portion of the focusing beam. For a Bessel beam with approach angle γ, located a distance D, away from a gas jet of length L and width W which sits a distance H below the optical axis, the near field beam is blocked when the radial coordinate $r(x, y)$ satisfies both of the following conditions:

$$r(x, y) < \sqrt{\left(\frac{W}{2}\right)^2 + y^2} + (D + L) * tan\gamma$$

$$r(x, y) > \sqrt{H^2 + x^2} + D * tan\gamma$$

(2.6)

An example of this masking effect is shown in Figure 2.4.
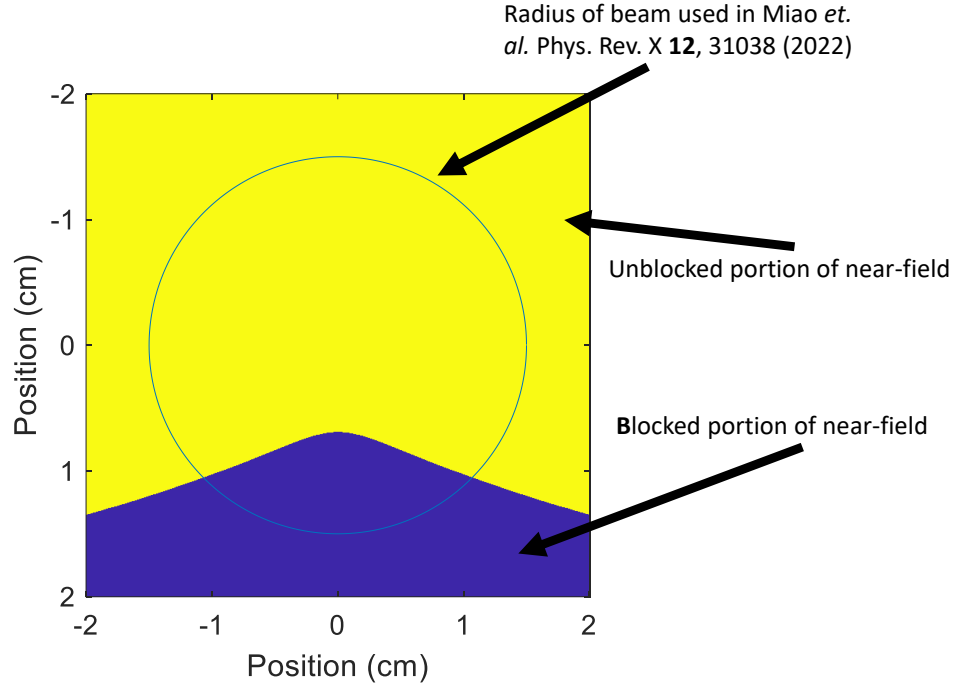
Figure 2.4: Near-field beam masking. The conical focus of a Bessel beam in the presence of an obstruction leads to blockage of the beam. The blocked portion of the near field can be calculated as described in Eq. 2.6. An example of this effect on the near field of the beam is shown for the experiments in [22].

This blockage naturally has a deleterious effect on the Bessel beam focus quality. For J_0 beams, this leads to slight asymmetry and lowered intensity in the central maximum (Figure 2.5(a,a')). So long as the central intensity remains above the OFI threshold, the deformation does not prevent the generation of a roughly cylindrical plasma column. We note that there will be less ionization in the wings of the maximum for the obstructed case. It is possible that this could result in less heating of the surrounding gas, which would reduce the local sound speed and expansion of the neutral shock, and in turn would result in some longitudinal dependence in the matched mode size: $w_{ch} \rightarrow w_{ch}(z)$. Further study is needed to quantify the effect of focal line deformation on waveguide uniformity, particularly in long (>20 cm) gas jets. Our initial assumption was that beam obstruction did not significantly alter the guiding properties of the

channels in [22,93,106,118], but recent measurements [150] of plasma channel expansion suggest there may have been non-negligible longitudinal variation in channel parameters.

For $J_{q>0}$ beams, the obstruction leads to significant deformation of the focus. As seen in Figure 2.5 (b',c') the focal ring is completely broken in the presence of the jet. This limited us the use of a short, 5 cm jet in the high power experiments of [106]. To implement this technique in a meter scale, high-power guide would require either a significant redesign of the jet allowing operation over a centimeter above the nozzle (which would require a significantly larger volume of gas and introduce longer ramps at the entrance and exit of the jet), or a solution to the focal deformation problem.

Fortunately, there is a possible optical solution. As shown in Figure 2.5(b'c'), the effect of the focal aberration is rotated 90° (counter)clockwise depending on the direction of the winding. For a binary Bessel beam, where $J_{\pm q}$ are superimposed, this means that the catastrophic deformation of the focus is significantly mitigated. Figure 2.5(d',e) shows that despite some variation in the intensity, the nucleated focal ring is still fully formed. And, with sufficiently high intensity, the obstructed focus will still be able to generate a similar plasma to the unobstructed beam. It is not clear exactly how the waveguide with a nucleated cladding will perform compared to those in [106]. Preliminary BPM simulations using a low-power beam suggest the nucleated cladding performs similarly to the continuous cladding. Air waveguides generated by filamenting higher order LG beams have also successfully used nucleated index structures [151,152]. It is also possible that plasma expansion will lead to the formation of a complete ring, or that ionization by the leading edge of the pulse (as in self-

waveguiding) could assist in formation of the cladding. Future experiments will investigate further.
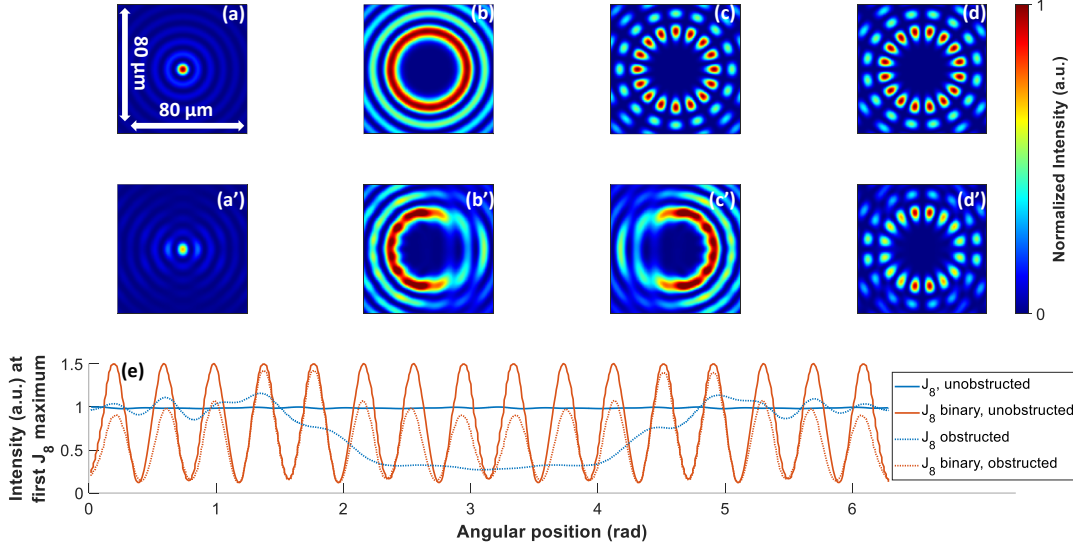
Figure 2.5: Far field effects of obstruction on Bessel beam formation. Pulse evolution is simulated with BPM (Sec. 1.6) and the gas jet profile used is the same as in [22] and Figure 2.4. All beams are formed by applying the appropriate azimuthal and radial phase profiles to a plane wave with $\lambda = 0.8\ \mu m$ and have an approach angle $\gamma = 3°$. **(a-d)** Intensity profiles after 8 cm of propagation without the gas jet for a J_0 Bessel beam (a), J_8 Bessel beam (b), hybrid $(J_8 + J_{-8})/2$ superposition of Bessel beams (c), and binary J_8 Bessel beam formed with a π-step phase plate. Each frame is normalized to its maximum. **(a'-d')** Intensity profiles after 8 cm of propagation with the gas jet obstructing the beam for a J_0 Bessel beam ('a), J_8 Bessel beam (b'), J_{-8} Bessel beam (c'), and binary J_8 Bessel beam formed with a π-step phase plate (d'). (a') and (d') are normalized to the maxima of (a) and (d). (b') and (c') are normalized to the maximum of (b). (e) lineouts of the intensity vs. angular position at the position of the first J_8 maximum for the profiles shown in (b),(d),(c'), and (d').

2.2.3 *In Situ* wavefront correction of Bessel beams

When applying Bessel beams to plasma waveguide generation, it is important that the highest intensity for a given pulse energy be generated in the central maximum of a J_0 beam, or uniformly around the first ring in a $J_{q>0}$ beam. This is equivalent to maximizing the fidelity of the near-axis portion of the beam to the Bessel functional form over the full length L_{focus}. As shown in Figure 2.6, the fidelity can be significantly

diminished by wavefront aberrations on the focusing beam. This aberration often has two dominant components: (1) wavefront aberrations imparted by the Bessel beam generating element, and (2) those already present and unavoidable in a high power laser. While correction of wavefront aberration is a common procedure in optics, and real-time correction of aberrations in Gaussian beams has been well-studied [153–155], these techniques are not readily applicable to the *in situ* wavefront correction of Bessel beams needed for plasma waveguide generation.
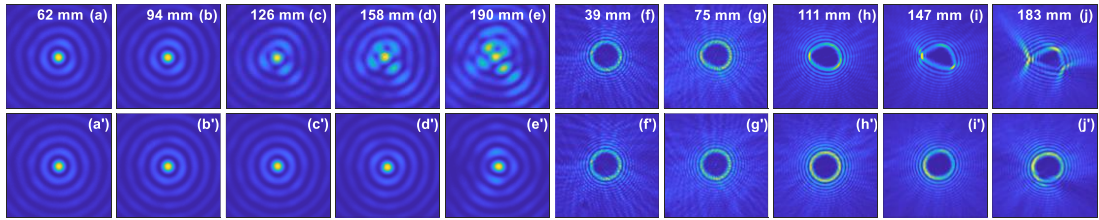
Figure 2.6: *In situ* correction Bessel beam wavefront aberration. **(a)-(e)** and **(a′)-(e′)** show the uncorrected and corrected intensity profiles for a J_0 Bessel beam formed with a reflective axicon at different points along the focal line. **(f)-(j)** and **(f′)-(j′)** show the same for a J_{16} beam.

To solve this problem, we have developed a technique to directly retrieve the complex amplitude of a Bessel beam from intensity measurements only [156]. In conjunction with a deformable mirror, this allows for reliable correction of standard Zernike aberrations [155] encountered in our use of axicons and ring gratings. For either of these focusing elements, the radial phase profile imparted to the incident beam results in the mapping of each differential annulus of the incident beam to a point along the Bessel beam focal line. By resolving the measured field profile at a point along the focal line into a Bessel function basis and then comparing it with an ideal Bessel beam, we can find the phase aberrations in the corresponding azimuthal slice of the incident beam. Using images at different points along the focal line, we are able to generate a

full phase map of the aberrations from the retrieved near field phase maps for each azimuthal slice, and correct any aberrations with a deformable mirror. The uncorrected and corrected J_0 beam focus along z is shown in Figure 2.6(a and a′ through e and e′). Note that for $z > 150$ mm (farther from the axicon, toward the end of the focal line), the uncorrected focal intensity profile is substantially deteriorated from the desired form, and would generate a highly asymmetric initial plasma. Deterioration of the focal profile is even more pronounced for high order Bessel beams, as shown in Figure 2.6(f and f′ through j and j′) which shows an uncorrected and corrected J_{16} beam. This correction was employed in the experiments described in [22,74,93,106,118]. Though the technique allows for complete reconstruction of the near-field phase by recording the focus at many points along the focal line, we found in practice that measurement of the dominant error components and correction at a single point near the end of the focal line was often sufficient for correction of the entire focus.

2.3 Meter-scale supersonic gas jets

2.3.1 Gas jets vs. gas cells

A suitable laser-generated plasma waveguide for a high-repetition rate, ~10 GeV LWFA module requires a gas profile which is low density ($\sim 10^{17}$ cm^{-3}) and long (up to tens of cm so that $L_{guide} \lesssim L_d$), with controllable longitudinal density variation (down to scales $\sim Z_R$) and is accessible for diagnostic measurements of the waveguide and the LWFA process [157]. While some of these criteria can be achieved with gas cells [107], gas flow through the required large-aperture laser access pinholes significantly limits the sharpness of the gas density ramps at the entrance and exit of

the waveguide. They also limit the minimum steady state operating density of the gas. Gas cells offer no control over longitudinal density variation, and their required laser access pinholes are susceptible to damage and widening by both the waveguide generating pulse and the guided LWFA driver pulse. The structural requirements of a gas cell can also limit diagnostic access to the waveguide and the LWFA process.

However, using a gas jet, a free-standing plasma waveguide can be generated in the gas plume away from the jet nozzle, and the full length of the waveguide is accessible for diagnostics. When operated in the steady-state flow regime, the repetition rate is limited only by the available vacuum pumping speed (assuming a high repetition rate laser is available to generate the waveguide). The gas density ramps at the ends of the jet can be significantly sharpened by supersonic flow, while the transverse gas density local profile is nearly uniform on the small transverse scales required for LWFA.

2.3.2 Design of meter-scale gas jets

We have implemented all of these features into the jets used in [22,74,93,118,122]. Though the specifics vary in each of these experiments, the general design was the same: high-pressure gas backs multiple solenoid valves and flows into a small reservoir beneath a narrow throat. The flow becomes supersonic as the gas moves into the wider region above the throat and then out into the chamber. These key features are identified in Figure 2.7, which shows the interior structure of the jet used in the experiments of Chapter 4, [74]. Design of the interior features is assisted by fluid simulations performed in Fluent. These simulations model flow in two dimensions, and employ a boundary layer based on the model in [158].

55
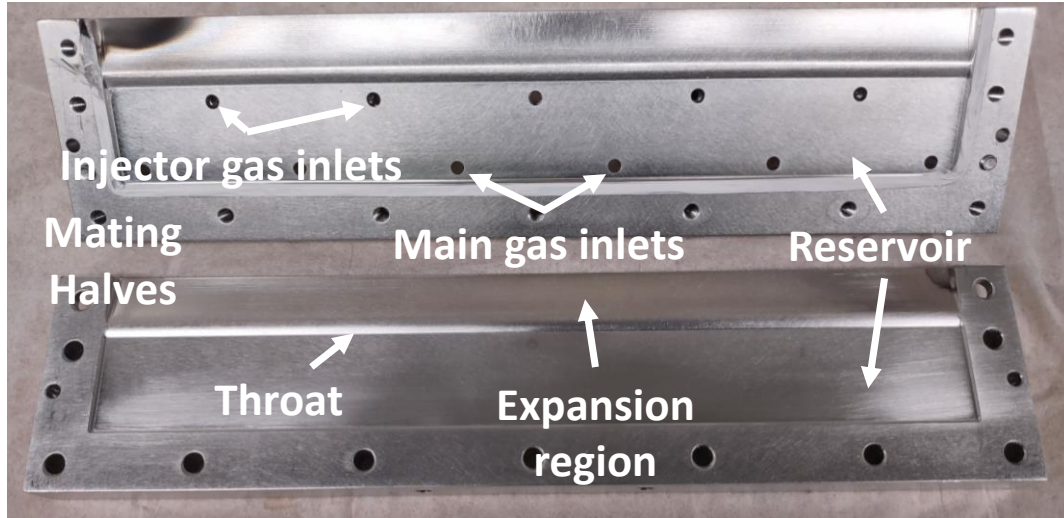
Figure 2.7: Gas jet interior structure with essential features identified. This version of the jet (used in [74] and the experiments discussed in Chapter 4) features injector gas inlets, which allow for localized regions of a second gas to be inserted into the density profile generated by the main gas filling the reservoir.

We have developed jets up to 50 cm in length. The versions used in experiments [22,93,106] achieved RMS longitudinal variation <25%, with variation due to manufacturing issues. Typically, imperfection in the throat width results in high spatial frequency variations, while mechanical stress between the two halves leads to low frequency variations. An example of these features in the longitudinal density profile at different heights above the jet used in [22] is shown in Figure 2.8(a). The technique for this characterization measurement is discussed in detail in section 2.4.2. The transverse density profile is extracted from interferometry (Sec. 2.4.1) in Figure 2.8(b). The supersonic flow ensures that the gas density gradient is flat on the short transverse scales of a LWFA drive pulse. Figure 2.8(c)(c') show the jet in operation.
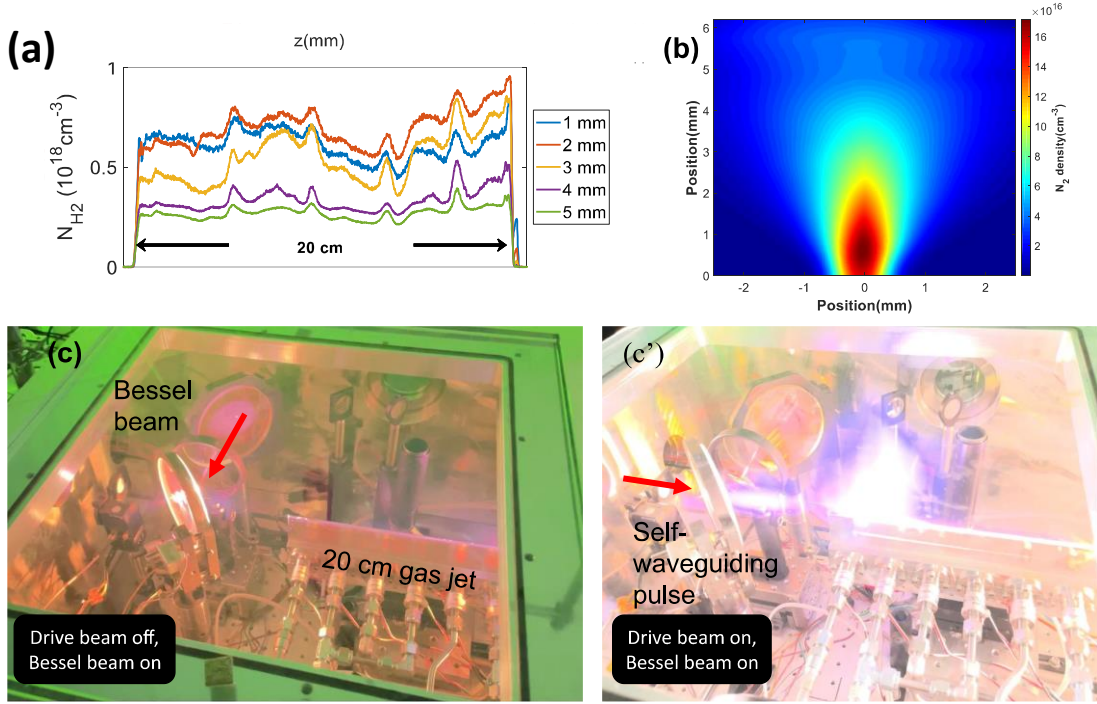
Figure 2.8: 20 cm supersonic gas jet. **(a)** characteristic longitudinal density profiles at different heights above the jet used in [22]. **(b)** characteristic transverse density profile of the jet extracted from longitudinal interferometry. **(c)** jet *in situ* for LWFA experiments with J_0-ionized plasma above. **(c')** jet *in situ* for LWFA experiments with fluorescence from self-waveguiding above.

The most recent jet implementation (used for the experiments in [74] and Chapter 4) has improved the RMS longitudinal variation to <10-15%, depending on the operating conditions. This jet was also the first version to include the secondary set of gas inlets marked as 'injector gas inlets' in Figure 2.7. Measurements of the density profiles are found in Figure 4.12. Though not successfully implemented in experiment, the jet used in [22] featured two separate reservoirs, allowing for different gases to be used in the first 5 mm and following 195 mm of the jet. A future design goal is to implement longitudinal control over the density profile. This could potentially aid in both controlling in injection, and reducing dephasing effects as discussed in Sec. 1.3.3.

2.4 Optical and plasma Diagnostics

Our diagnostics for plasma waveguide LWFAs fall into three main categories: (1) plasma channel diagnostics, (2) LWFA drive pulse diagnostics, and (3) electron bunch diagnostics. Here will discuss the essential diagnostics for operating and understanding the LWFAs discussed in Chapters 3 and 4.

2.4.1 Interferometry

In our experiments, plasma and neutral gas densities are measured via two-color interferometry [93,106]. Density profiles can be measured by passing an ultrashort probe pulse ($\lambda = 400\ nm$ or $\lambda = 800\ nm$, 10s μJ energy) transversely through the plasma structure at a known delay from its formation. The relative phase shift is then measured by splitting and interfering different portions of the probe beam in a shearing interferometer [159]. Since the index of refraction in plasma and neutral gas has different dependences on wavelength, comparing the phase shift for the two different colors allows extraction of separate plasma and neutral gas density profiles [93,106]. We note that the phase shift may also be measured through other techniques, such as wavefront sensing [160]. Once a measurement of the phase has been retrieved, the respective density profiles can be extracted through Abel inversion, which reconstructs the cylindrically symmetric density profile corresponding to the measured phase shift [161]. Though the technique introduces some uncertainty for plasma structures with a significant difference between on and off-axis plasma densities [93,106], the method has been frequently applied to measurement of plasma waveguide density profiles [22,93,106,107,110,112,124]. A variation of the technique has also been developed which allows extraction of asymmetrical density profiles [106,161].

Phase measurement may also be applied to probe pulses propagating longitudinally with respect to the plasma/gas structures. While the technique has been successfully used for characterizing gas jets [106,118] and short plasma waveguide structures [110], there are limitations on its application. If the accumulated phase in some parts of the beam is such that the phase difference over a small region is $> 2\pi$, interference fringes are broken and reconstruction of the true phase is difficult. For the cm scale plasmas used for waveguides, large phase shift is unavoidable, requiring much smaller 'test' structures to be measured. For these test structures, the density ramps at the beginning and end of the structure can provide significant contributions to the overall phase shift, requiring further measurement and analysis to infer the correct density profile.

2.4.2 Fluorescence measurement of longitudinal uniformity

Longitudinal uniformity of waveguides generated in our experiments is closely tied to the longitudinal uniformity of the gas flow out of the supersonic jets used in those experiments. The longitudinal density profile of the extended gas plume is characterized through a novel fluorescence measurement technique [22,118].

A J_0 pulse is focused in the H_2 jet, generating a plasma column via OFI. The recombination fluorescence is imaged through a 656 nm bandpass filter, which restricts the measurement to the H-alpha line (Figure 2.9). The abrupt ends in the fluorescence image of Figure 2.9(a) are determined by the sharp ~ 2 mm falloff in gas density at the ends of the jet. While the fluorescence intensity is proportional to the z-dependent H_2 density at given location, an absolute calibration of this measurement decoupling the longitudinal intensity profile of the laser is still needed. This is accomplished by filling

59

the experimental vacuum chamber with variable known pressures of hydrogen and generating OFI plasmas with the jet nozzle still in place but with the valves closed (Figure 2.9(a')). Since the gas now uniformly fills the region around the gas jet, any z-dependence in fluorescence intensity is caused by longitudinal variation in the J_0 beam profile over the focal length, L_{focus}. Therefore, in regions where the fluorescence above the pulsed jet does not have the same shape as the backfill fluorescence, the gas density is non-constant. The gas density at a longitudinal position z is then found by interpolating the density as a function of backfill fluorescence intensity at the same z, and calculating the density corresponding to the measured jet fluorescence. Figure 2.9(a'') plots the column-averaged fluorescence at different backfill pressures and above the pulsed jet, illustrating how the jet pressure may be inferred from the fluorescence intensity.
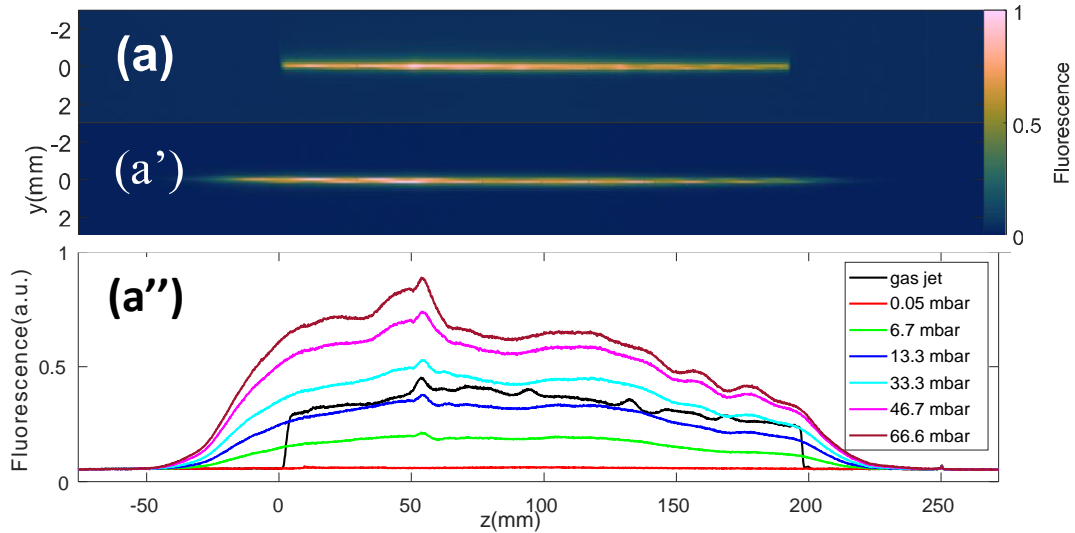
Figure 2.9: Fluorescence measurement of longitudinal uniformity. **(a)** example of H2 fluorescence above the 20 cm jet used in [22]. **(a')** example of fluorescence in backfill. **(a'')** lineouts comparing fluorescence response above jet and in backfill of different pressures

2.4.3 Exit mode analysis

Collection of the waveguide exit mode can be used to recover key information about both the waveguide structure and evolution of the guided pulse. Imaging of the exit mode (as in Figure 3.4)is essential for determining the presence of multimode guiding and the fundamental mode structure for monomode guiding. If the imaging system is calibrated to an unguided pulse, mode imaging can be used to estimate the throughput of the guide [22,93,106]. Mode imaging has also been used to calculate the attenuation lengths of plasma waveguides generated in adjustable length gas cells [107] and to determine discharge capillary waveguide structure by varying the coupling alignment and recording effects on the exit mode [162]. Light collected at the waveguide exit may also be sent to a spectrometer. In particular, this diagnostic is important for verifying red-shifting of the pulse related to driving plasma wakes [22,46].

2.5 Electron bunch diagnostics

Diagnosing electron beam properties requires a different set of tools than those used for diagnosing optical systems. The key parameters of an electron bunch are its charge, energy distribution, and emittance. Naively, these quantities look at how many electrons are in a given bunch, how fast they are moving, and how quickly they are moving away from each other. Since the beam physics of LWFAs is not yet as mature as for conventional accelerators, optimization and understanding of these quantities is an open research area [157].

Due to the sensitive nature of the injection process, accelerated bunch charge is typically highly variable in LWFAs. Better diagnosis and control of injected charge is

key for future applications of LWFA electron beams [9,12,32]. For conventional RF accelerators, the energy distribution is monoenergetic, with very small spread ΔE around a central value, E. This is not necessarily the case for LWFAs, which can generate electron beams with continuous energy spectra, multiple 'quasi-monoenergetic' peaks, or more tightly controlled energy spreads. Emittance is a measure of the area of an electron beam in momentum-position phase space. Large, divergent beams have high emittance. Small, collimated beams have low emittance. For LWFA-generated electron beams with a small initial beam size, it is common to refer to the divergence in place of the full emittance. We will use this convention in this dissertation.

2.5.1 Electron beam mode imaging

For applications (such as staged particle acceleration or as the driver for an FEL), it is important to understand the full phase space of an electron beam. This is difficult to measure simultaneously for beams from LWFAs. However, some of the information can be gathered by looking at the time-integrated signal from passing the beam through a fluorescent sheet (or image plate or film) [157,163–165]. Though this measurement is independent of electron energy and integrated over the entire temporal duration of the bunch, it can be useful for estimating beam quantities such as the divergence or total charge. Images of the beam profile have also been used to identify characteristic beam features indicative of relativistic filamentation and other electron beam propagation instabilities [166–168].

In the experiments of [22] and [74], electron beam profiles were collected via imaging of fluorescing Lanex (LA1 in Figure 3.1, details of the response calibration

are discussed in Sec. 2.5.2) [163]. The Lanex screen was located outside the experimental chamber in order to enable simultaneous collection of the electron beam profile and transmitted laser mode. We will refer to this diagnostic as the 'electron beam mode imaging system'. Though the configuration of the electron beam mode imaging system allowed for flexibility, the setup faced some clear accuracy limitations. An example of the limitations of this diagnostic is shown in Figure 2.10. When the optical end mode imaging mirror is out of place in panel (a), the electron beam is tightly focused and causes bright enough Lanex fluorescence that the imaging camera is saturated. When the mirror is in place (b), the electron beam propagates through it, and experiences a significant increase in beam divergence due to scattering in the bulk material. The effect increases for beams with lower energy and larger initial divergence. Scattering effects can modelled through simulations which combine ray tracing with low-resolution PIC techniques [169]. Electron-neutral collisions can also emit x-rays which cause the Lanex to fluoresce. The combination of these two effects results in the roundness of the Lanex fluorescence imaged in (b). Given these limitations, we have not used the electron beam mode imaging system for charge measurement.
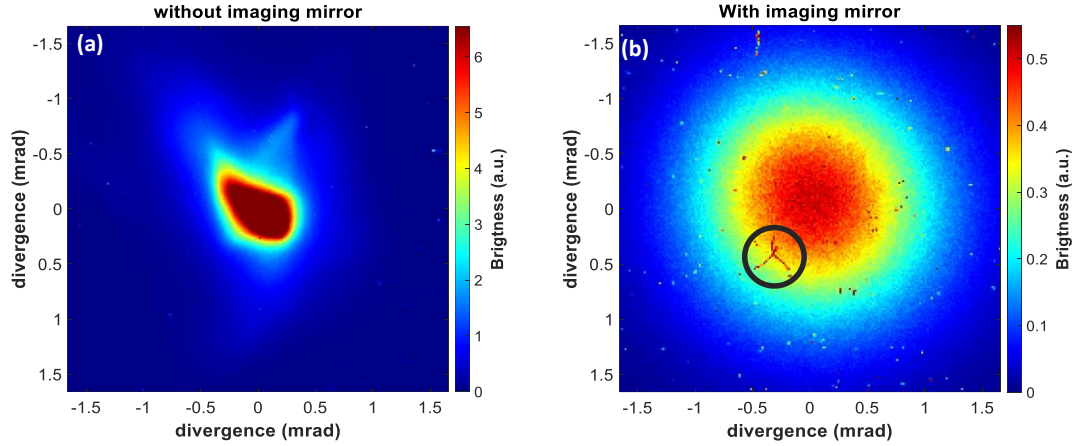
Figure 2.10: Comparison of electron beam profiles recorded **(a)** with and **(b)** without end mode imaging mirror in place. On panel (b), characteristic high-energy photon noise is circled.

Both images display the same type of characteristic high (spatial) frequency noise, an example of which is circled in Figure 2.10(b). This is caused by the interaction of high-energy photons both with the Lanex and directly with the CCD of the imaging camera, and must be removed for accurate image processing. This includes interpolation of spectra and calculating summed values such as the charge or angle-integrated spectra. The problem is similar to the removal of cosmic ray events in long exposure CCD images collected by telescopes [170–172].
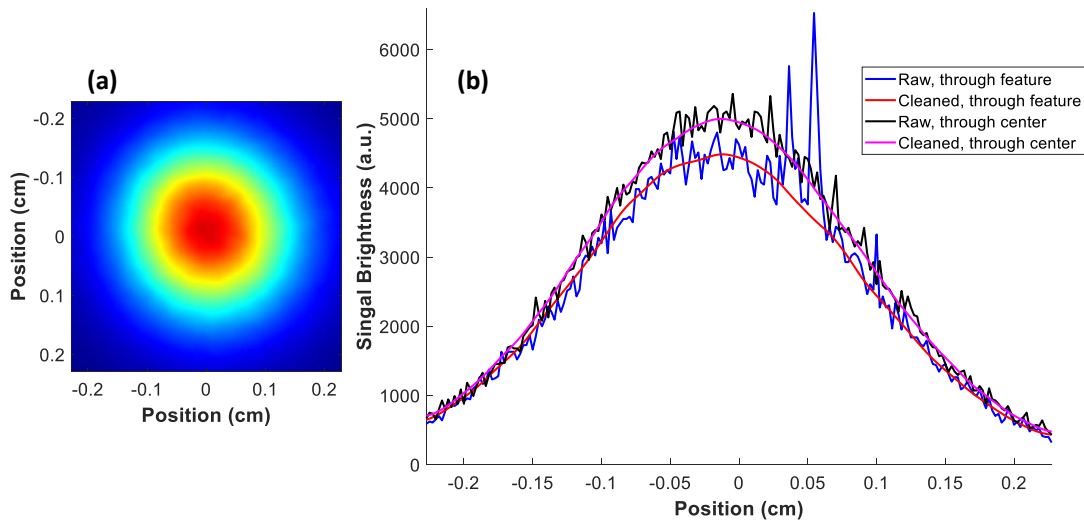
Figure 2.11: Example of gradient-based edge detection cleaning for Lanex image of electron beam mode. **(a)** cleaned image of raw signal shown in Figure 2.10(b). **(b)**

64

lineouts of the raw and corrected signals through the noise circled in Figure 2.10(b) and through the center of the beam.

We have employed two methods for removing this type of noise for our data. For high signal images, where the underlying signal is more continuous, gradient-based edge detection and replacement has been sufficient. Figure 2.11(a) shows the image in Figure 2.10(b) cleaned by this technique. It has been smoothed with a Gaussian kernel over a 15 pixel window as a part of the cleaning processing. The lineouts in Figure 2.11(b) correspond to the clean and raw signal both through the noise circled in Figure 2.10(b) and through the center of the electron beam, and demonstrate that the magnitude and structure of the underlying signal are preserved through this method.

For low signal images, there is more pixel-to-pixel variation in than real signal than in the noise, so we use a Density-Based Spatial Clustering of Applications with Noise (DBSCAN, [173]) algorithm to detect clusters of noise pixels. An example of the different results using the gradient descent and DBSCAN methods is shown in Figure 2.12. Panel (a) shows the raw Lanex image collected after electrons have been dispersed by the spectrometer, (b) shows the result after cleaning by the gradient algorithm, and (c) shows the result after cleaning with the DBSCAN algorithm. Angle integrated spectra for each frame are shown in panel (d).
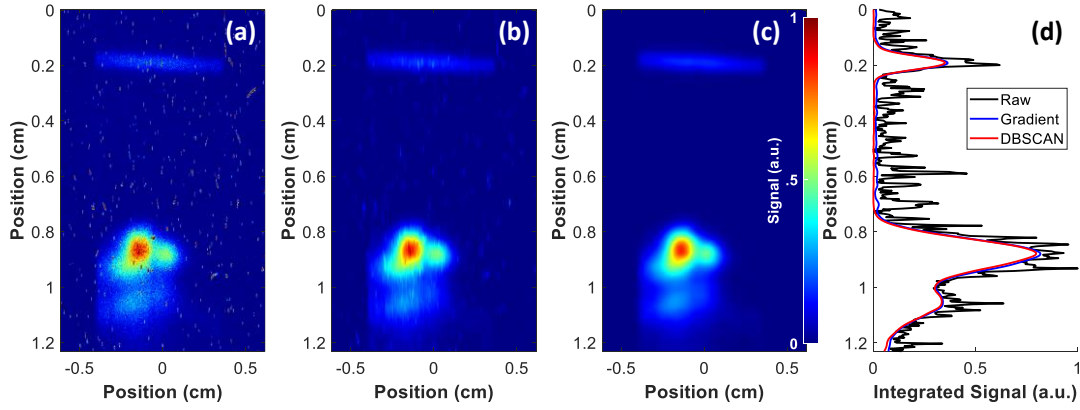
Figure 2.12: Comparison of noise removal methods for electron spectrometer images. **(a)** raw image. **(b)** correction using gradient edge detection. **(c)** correction using the DBSCAN method. (a)-(c) are normalized to the same arbitrary value. **(d)** angle-integrated spectra for (a)-(c), normalized to the maximum of the integrated raw image.

These angle integrated spectra show that both methods conserve the underlying signal

and dispersion reasonably well. However, it is clear in Figure 2.12(b) that the gradient

detection method does not fully remove noise. Even though the residuals are small,

they introduce significant error during further processing (Sec. 2.5.2).

2.5.2 Electron spectrometer

Electron spectrometers are the primary tool for diagnosing the energy content

of electron beams [157,174–176]. They rely on the natural deflections of charged

particles moving in magnetic fields to disperse electrons spatially according to their

energy. Electrons travelling with a velocity $\boldsymbol{v}$ in a magnetic field $\boldsymbol{B}$ are deflected

through the Lorentz force:

$$\boldsymbol{F} = q\boldsymbol{v} \times \boldsymbol{B}/c. \tag{2.7}$$

For a known magnetic field, this means that the electron velocity can be calculated if

the particle trajectory is known. For a single particle, this is straightforward with a static

magnetic field. But, for an electron bunch containing many electrons with different

energies and transverse momenta, trajectories can overlap, and it can be difficult to

66

accurately infer the range of electron energies. This difficulty can be alleviated (and the concomitant measurement uncertainty) by choosing a spectrometer with magnetic fields that are nearly constant across the whole deflection region and ensuring good alignment to the electron beam. Using an aperture on front of the spectrometer can also reduce uncertainty in analyzing the spectra of spatially large beams.

Once the beam has been dispersed by the magnets, the position of the deflected electrons needs to be recorded with some sort of scintillator, fluorescence screen, or image plate. The differential charge can possibly be inferred from the magnitude of this signal, although that requires a calibration of the material response and does not provide an absolute measurement of the charge if an aperture is used.

In the experiments discussed in Chapters 3 and 4, we employed a modular permanent magnet spectrometer. Each module consisted of two 4″x 2″ x 1" grade N52 neodymium magnets in a square yoke configuration. The central deflecting field strength was measured to be 0.93 T ($\pm$ 0.005 T), with ~5% variation in the direction of the field, and the non-deflecting field components <1% the strength of the deflecting component. For the experiments in this dissertation, we used a three-module assembly with magnetic steel caps placed on the ends of the magnets at the entrance and exit to mitigate the fringing fields outside of the spectrometer. The entrance of the magnets was placed outside the vacuum chamber, 2.85 m from the end of the waveguide, with a 10 cm deep, .25-1 mm tall adjustable lead slit. Electrons were deflected in the field onto a Lanex screen placed at the end of the magnet (13″ from the entrance). The screen was imaged with a f=25 mm, $f/1.4$ lens from 10.75 cm away with a beam path that included a 7.62 cm $\times$ 7.62 cm silver mirror at 45° and a 546 nm bandpass (FWHM=10

nm) filter to protect the imaging camera and filter out extraneous laser light. Measured

signals were deconvolved and interpolated onto a linear energy scale using an energy

calibration calculated from simulations of electron deflection in the measured field

[22,169]. As referenced in Sec. 2.5.1, the deconvolution and interpolation process is

highly sensitive to image noise. Since the energy dispersion curve is non-linear, noise

in the high energy portion of the spectrum can be amplified by interpolation onto a

linear axis.
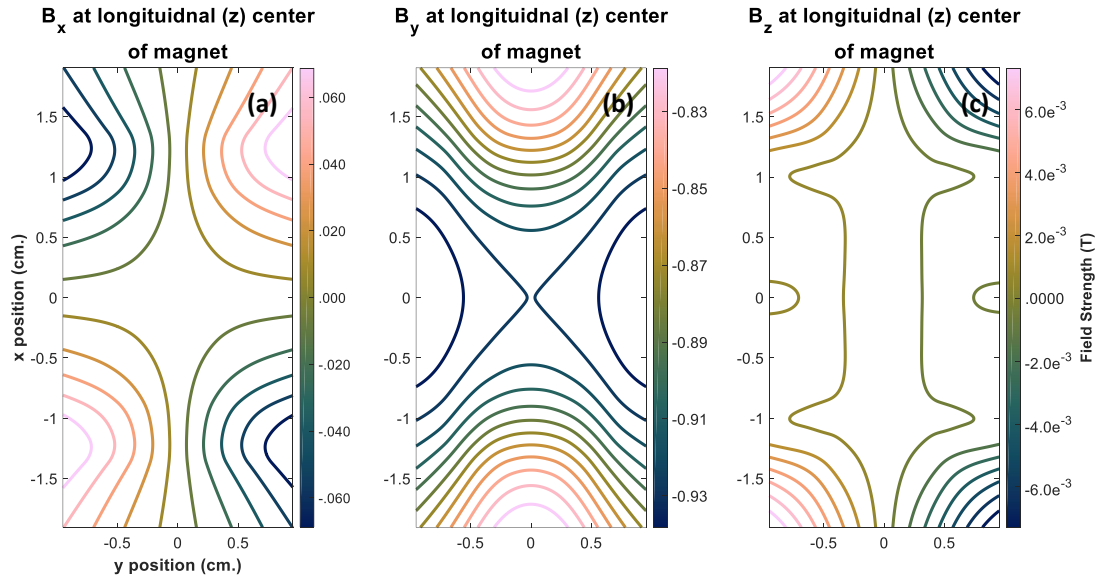
Figure 2.13: Contours permanent magnet field components. Electrons propagate in the longitudinal ('z') direction, and are deflected down (the 'x' direction) by the transverse magnetic field component along the 'y' direction. **(a)-(c)** the x,y and z components of the magnetic field.

Figure 2.13 shows the measured field strength at the center transverse plane of

a module. Since the modules are of identical construction and the ends of the magnets

are brought into contact in the full assembly, this is assumed to be the field

configuration throughout the central longitudinal region when multiple modules are

used (excluding the 'upramp' and 'downramp' at the entrance and exit). This

assumption was corroborated by longitudinal measurements of the field in the three-module configuration. Figure 2.14 shows the limited effect of the non-deflecting fields during the 'upramp' of the field.

We obtained an energy calibration by simulating the deflection of collimated electron beams of different energies in this field using the ray tracing program CyberRay [169]. Figure 2.13 shows that the deflecting field in the axial center of the magnet is concave, which results in greater deflection of electrons at the edges of the magnet than at the center. An example of this is shown in the raw spectrum in Figure 2.15(a) and Figure 2.15(b) shows the spectra mapped onto a linear energy axis using the calibration calculated with CyberRay. This accurately accounts for the position-dependent deflection and removes the bowing from the spectrum.
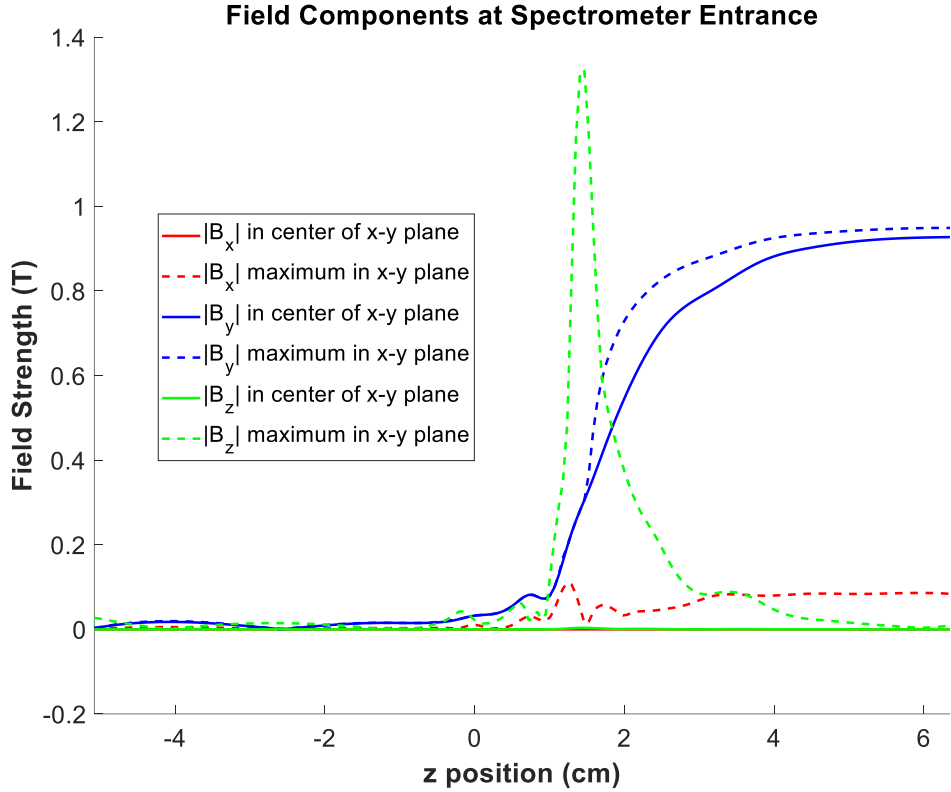
Figure 2.14: Lineouts of the fringe field values during the magnet upramp. The steel caps are located at z = [0, 1.27] cm and the magnets z > 1.27 cm. The solid lines represent the field values at the center of the magnet (in x and y), while the dashed lines correspond to the maximum values of the respective fields at the magnet boundaries.

Due to the placement of the magnet outside the chamber, the spectrometer has a narrow acceptance angle of 0.35 mrad (full angle divergence) for the 1 mm tall slit used in [22]. This is even smaller for the .5 and .25 mm slits employed in [74]. Use of a slit introduces an absolute energy uncertainty, which arises from the difference between possible measured energy values for an electron of a given energy with +/- maximum divergence accepted by the slit. As shown in Figure 2.16, this leads to, at worst, an uncertainty <130 MeV for the 1 mm slit and decreases roughly linearly for the smaller slits. The resolution limit describes the measured energy span of a monoenergetic beam which has been apertured by the slit (this includes deconvolution of the signal). The resolution limits imposed by the different slits are shown in the same

70

figure. The 10-15% limit for the highest measured energies suggests that our measured

(with the 1 mm slit) energy spreads in [22] are indeed resolution limited.
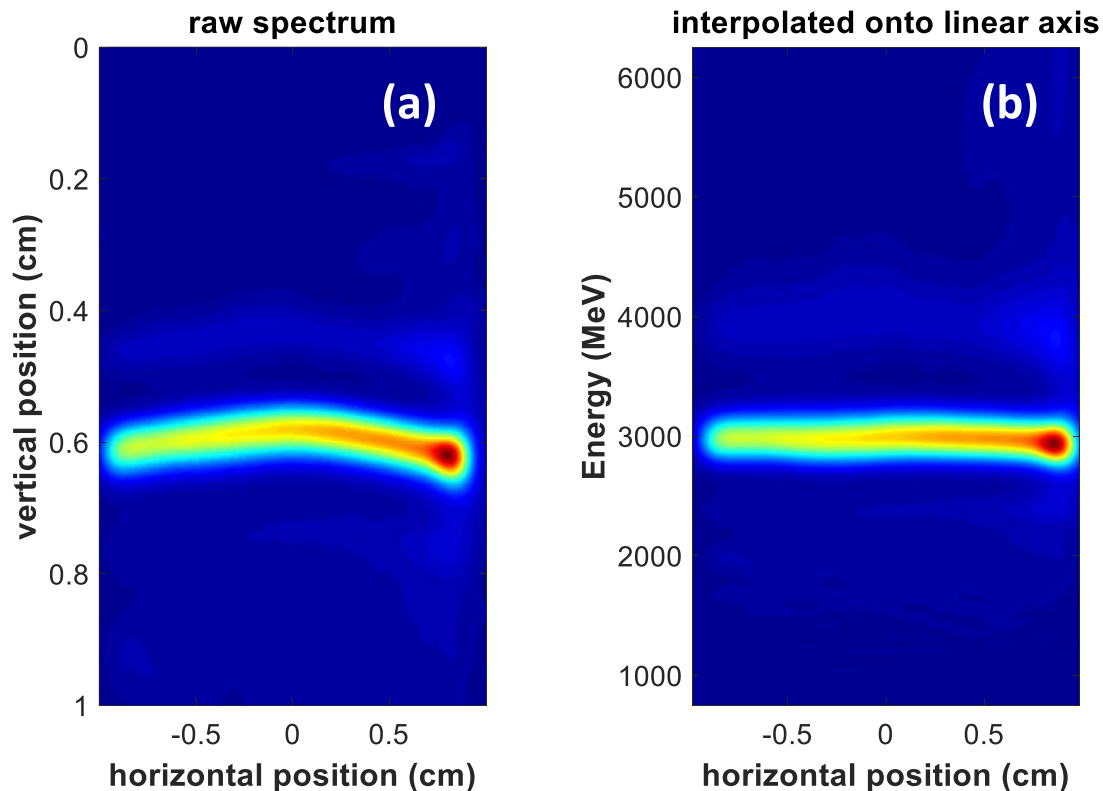
Figure 2.15: Example of spectrum interpolation onto a linear energy axis. **(a)** Raw spectrum showing position-dependent deflection. **(b)** The same spectra plotted on a linear energy axis using the calibration from the measured field.

Electron beams pass through the magnetic spectrometer's adjustable entrance

slit and are deflected through the 33 cm magnet. Kodak Biomax MS Lanex [163] was

used as the scintillating screen (LA2 in Figure 3.1), with the fluorescence imaged by a

Andor Zyla 4.2 camera. We note that the Lanex response has been observed to decrease

approximately linearly with electron energy up to 1.5 GeV [177]. However, we did not

have the means to verify the calibration for our Lanex screen at multi-GeV electron

energies, so we used the low-energy (40 MeV) calibration from [163]. Assuming the

Lanex response trend of [177] leads to undercounting of the signal and a conservative estimate of the bunch charge. The measurements in [164,177] suggest the calibration in [163] may be undercounting the charge by as much as a factor of 2.

Another important limitation on the measurement of bunch charge is our use of the narrow ≤ 1 mm, ≤ 0.35 mrad slit to aperture the beam. With ~milliradian divergence, the electron bunches produced in our experiments overfill even the 1 mm slit aperture. Furthermore, as can be seen in the electron spectra presented in Chapters 3 and 4, there is shot-to-shot variation in the individual electron bunch pointing (and also sometimes within the same shot), as demonstrated by the different horizontal (long dimension of slit) locations of spectral peaks. In some cases, this pointing variation is so extreme that peaks are seen to be cut off by the edges of the magnets.
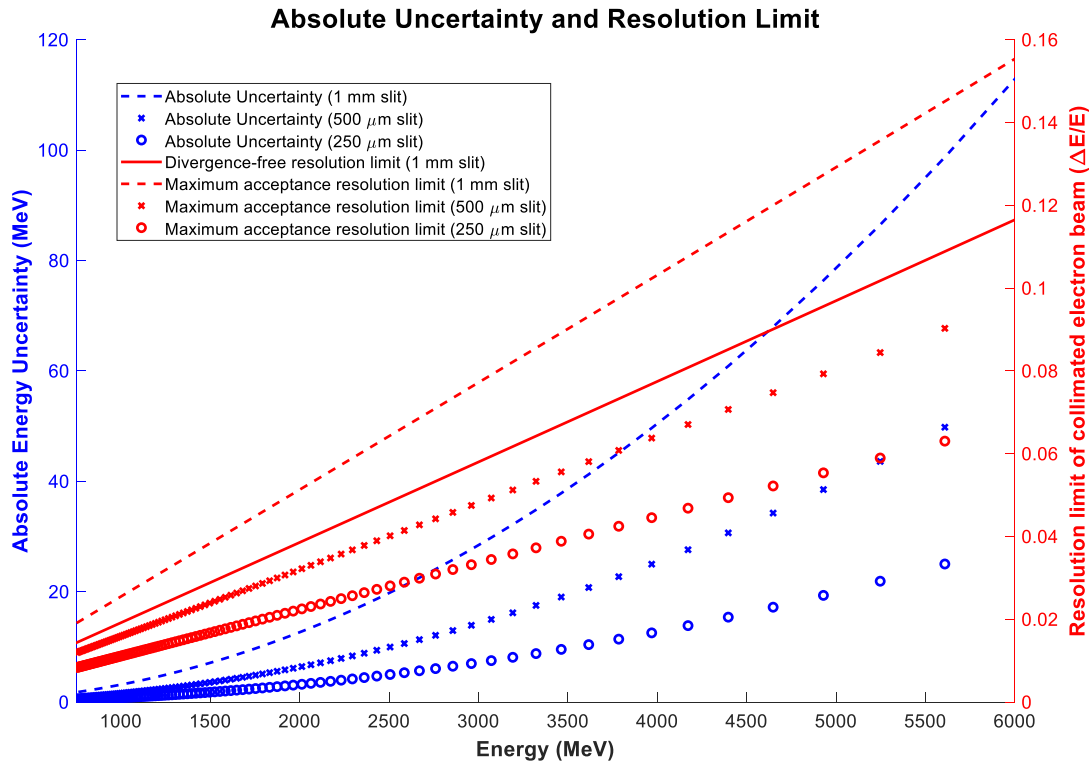
Figure 2.16: Absolute uncertainty and resolution limit of electron spectrometer with variable width collimating slits. Left axis: the absolute energy uncertainty is shown in

the blue dashed lines. Right axis: the solid line is for a divergence-free beam (only for the 1 mm case) and the dashed lines are for a beam with the maximum accepted divergence.

While a precise measurement of the charge was not possible with our setup, we did improve the lower bound on the charge estimate by using the measured beam divergence to estimate the percentage of the beam blocked by the slit. For a given shot, we assumed the electron beam profile was Gaussian, then used the measured divergence (from the non-deflected dimension on LA2) to calculate the beam size. From this, we found the percentage of the charge that would be transmitted into the spectrometer for a perfectly aligned electron bunch. This ratio is used for each shot as an additional calibration factor to estimate the actual charge. We note that if the bunch pointing variation in the short dimension of the slit is similar to the long dimension, it is possible for bunches to only slightly coincide with (or miss entirely) the narrow <1 mm slit. This means that only a few electrons far from the spatial center of the bunch would be coupled through the slit into the spectrometer. The correction assumes that the brightest portion of the electron beam is sampled, and so can still massively underestimate the charge for bunches which nearly miss the slot.

2.5.3 Electron bunch charge measurement

As mentioned in the previous two sections, estimates of the charge can be gathered directly from the calibrated responses of fluorescent sheets/image plates. These measurements are, however, limited in the different ways discussed above. Time-dependent measurements of the current can be achieved with use of an integrated current transformer (ICT) [157,177]. These are commonly used on conventional RF-driven linear accelerators, but have several challenges for use with LWFAs: they are

sensitive to RF noise, a large amount of which is produced in LWFAs, and they measure charge independent of energy. However, the RF sensitivity can be overcome with specialized electronics [178], and ICTs have been successfully employed in concert with broadband electron spectrometers [23].

Chapter 3: First demonstration of multi-GeV LWFA in a fully optically generated plasma waveguide

3.1 Introduction

In this section we will discuss the first demonstration of multi-GeV laser wakefield acceleration in a fully optically formed plasma waveguide [22]. The guide was formed via self-waveguiding of <15 J, >45 fs ($< \sim 300$ TW) pulses over 20 cm in a low density gas jet, with accelerated electron bunches driven up to 5 GeV in quasi-monoenergetic peaks of relative energy width as narrow as $\sim 15\%$, with divergence down to ~1 milliradian and charge up to tens of picocoulombs under optimum conditions. The accelerating gradient was as high as 25 GeV/m, and we observed that energy gain was inversely correlated with on-axis waveguide density in the range $N_{e0} = (1.3 - 3.2) \times 10^{17}$ cm^{-3}. We will present experimental and simulation results which show that shot-to-shot stability of bunch spectra and charge are strongly dependent on the pointing of the injected laser pulse and gas jet uniformity. We will also present evidence of pump depletion-induced dephasing, a consequence of the long optical guiding distance.

3.2 Experimental setup

The experimental setup is shown in Figure 3.1. The laser used in the experiments is the ALEPH laser at Colorado State University [179]. A LWFA drive pulse P1 ($\lambda = 800$ nm, $\tau = 45$ fs FWHM, energy <15 J) was focused by an $f/25$ off-axis paraboloid into the refractive index structure generated in a 20 cm long gas jet by a 0.5 J, 75 fs, J_0 Bessel beam pulse, P2, which was phase corrected by a deformable mirror [93,106,156] and then compressed by a separate pulse compressor.
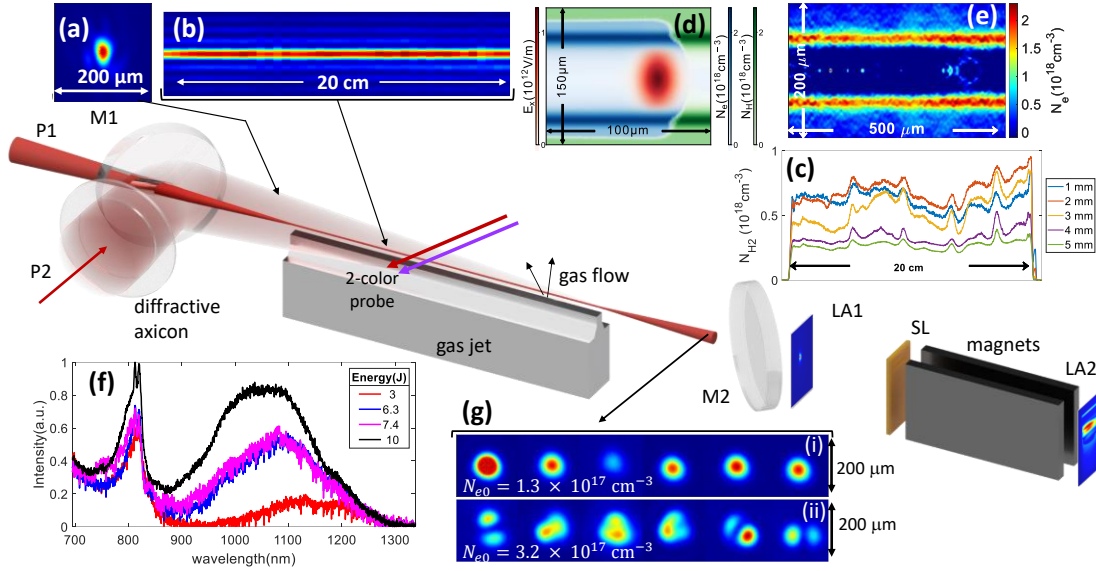
Figure 3.1: Experimental setup. LWFA drive laser pulse (P1): ($\lambda = 800\ nm$, τ_{FWHM} =45 fs, energy <15 J), focused by an $f/25$ off-axis paraboloid through a 9.5 mm diameter, 45° hole in mirror M1. Index-structuring pulse (P2): ($\lambda = 800\ nm$, τ_{FWHM} =75 fs, energy 0.5 J) J_0 Bessel beam pulse formed by 4-level transmissive/diffractive axicon, forming a 20 cm long plasma by OFI in the working gas 2.5 ns in advance of P1. The plasma expands radially, forming an elongated refractive index structure: a low density plasma on axis surrounded by an enhanced density annular shell of neutral gas. Two colour interferometer probes: for measuring N_e and neutral gas density profiles (see Sec. 2.4.2). M2: pickoff mirror for guided mode imaging. LA1: Lanex fluorescing screen for full electron beam profile imaging. Magnetic spectrometer (Sec. 2.5.2 and online supplement of [22]): 1 mm entrance slit (SL), 30-cm long permanent magnet array (field 0.93 T), Lanex fluorescing screen for electron energy spectrum (LA2). Gas jet: Mach 4 supersonic nozzle, orifice length 20 cm, fed by 5 solenoid valves backed by pure H_2 or a 95/5% H_2/N_2 mixture at backing pressure 13.8-34.5 bar. Inset panels: **(a)** Focal profile of P1. **(b)** Longitudinal scan of the J_0 Bessel beam (P2) focus. **(c)** Axial profiles of gas density vs. height above the nozzle (Appendix A)**. (d)** Simulation using the particle-in-cell code FBPIC ([120], Appendix C) of self-waveguiding in hydrogen refractive index structure. **(e)** Plasma waveguide profile interferometrically measured $\sim1\ ps$ after passage of self-waveguided pulse. **(f)** Guided laser spectra at waveguide exit vs. input pulse energy (and injected peak a_0). **(g)** Effect of shot-to-shot P1 pointing fluctuations on guided mode for (i) low density guide and (ii) higher density guide. The root-mean-square pointing jitter is (i) $\sigma_x = 4\ \mu m$, $\sigma_y = 6\ \mu m$, and (ii) $\sigma_x = 7\ \mu m$, $\sigma_y = 7\ \mu m$.

The drive pulse P1 is focused through a hole in mirror M1, with the beam waist

located at the entrance of the index structure. A vacuum mode image is shown in Figure

3.1(a). P2 is generated by passing a 5.5 cm diameter super-Gaussian pulse through a 4-level [144,180] diffractive axicon (fused silica substrate, 0.5 mm thick, see Sec. 2.2.1) which converts the 0.9 J input to a J_0 beam of energy 0.5 J. The beams forming pulses P1 and P2 are split upstream in the laser chain, prior to their respective compressors, using several fixed ratio beam splitters. An axial (z) imaging scan of the J_0 beam intensity profile is shown in Figure 3.1(b). The diffractive axicon simplifies the experimental geometry and enables co-propagation of P1 and P2, in contrast to counter-propagation necessitated by our prior use of reflective axicons [93,106]. The rays of the J_0 pulse approach the optical axis at angle $\gamma = 2.3°$; the 65cm long focus longitudinally overfills and fully ionizes (via OFI) a 20 cm long column in the gas sheet 3 mm above a Mach 4 supersonic nozzle fed by 5 high pressure pulsed solenoid valves fed with different working gases. The J_0 beam's average on-axis intensity over the gas jet is $\sim 8 \times 10^{15}$ W/cm^2, well in excess of the $\sim 10^{14}$ W/cm^2 OFI threshold for hydrogen. Axial profiles of H$_2$ density are shown in Figure 3.1(c) for various heights above the nozzle, measured as described in Sec. 2.4.2. The gas density at the ends of the jet sharply transitions to vacuum over ~ 3 mm. The bumps in the density profiles are due to slight variations in the nozzle orifice width along z and structural obstructions inside the nozzle. Electron spectra are measured by a $0.75 - 6.5$ GeV range magnetic spectrometer consisting of a 30-cm long permanent magnet array (field 0.93 T) with a 1 mm entrance slit 3 m from the plasma waveguide exit (see Sec. 2.5.2).

Figure 3.1(d) shows a particle-in-cell simulation using the code FBPIC ([120], Sec. 1.6) of the self-waveguiding process: the leading edge of the pulse injected into the index structure forms the plasma waveguide cladding as it propagates (left to right)

into the index structure. An interferometric measurement of the plasma density profile ~ 1 ps after self-waveguiding is shown in Figure 3.1(e), where the enhanced plasma density shell is the cladding generated by the self-waveguided pulse. The P1 injection delay of 2.5 ns after P2 is chosen so that the $1/e^2$ intensity radius of the lowest order mode of the formed plasma channel matches P1's $1/e^2$ intensity spot radius. The P1 energy leakage from the index structure before self-waveguiding is established is small: for a ~10 J, ~50 fs pulse, the hydrogen ionization threshold of 10^{14} W/cm^2 is reached at $r = w_{ch} = 30$ µm, ~100 fs before the peak of the pulse. For the guides generated by self-waveguiding in these experiments, we estimate a total cost (in the J_0 beam and the self-waveguiding beam) of 15-20 mJ/cm, based on scaling from [93] and simulations. We note that this is the energy cost of the interaction itself, not the total cost when accounting for energy loss during transmission through the beam line.

While the self-waveguiding energy cost is small for a 10 J-scale pulse, the laser energy invested in plasma waves can be substantial. The experimental signature of energy deposition into plasma waves is increasing energy in the red shifted wings [16,17] of guided pulses at increasing energy. This signature is seen in the guided mode optical spectra of Figure 3.1(f). The peak of the red wing trending bluer with higher laser pulse energy may be due to pulse lengthening accompanying depletion (see Sec. 3.5.2).

For fixed nominal laser and waveguide parameters, a major source of shot-to-shot variation in accelerated electron bunches is fluctuating alignment of the drive pulse P1 into the refractive index structure generated by P2. The index structure's transverse position is relatively stable from shot to shot (centroid standard deviations

78

$\sigma_x \sim \sigma_y \sim 2$ μm), as it is mainly determined by transverse positioning of the diffractive axicon and not by variations in P2 pointing. P1 pointing fluctuations are $\sigma_x \sim \sigma_y \sim 9$ μm owing to a longer effective lever arm. These fluctuations result in increased energy coupling into the higher order modes of the waveguide, which either leaks away leading to variable intensity transmission of the fundamental mode of the guide or leads to multi-mode propagation through the guide (see secs. 1.4.2 and 3.3). Figure 3.1(g) shows some examples of monomode and multi-mode guiding collected on the end mode imaging camera.

3.3 Guiding of > 100 TW pulses

Measurements of the guiding properties of >100 TW self-waveguiding pulses were performed in H_2 working gas in order to suppress electron injection. No evidence of an electron beam was observed on the electron beam diagnostics for these experiments, indicating ionization injection of N^{5+} electrons as the primary injection mechanism for our acceleration experiments.

3.3.1 Guided mode spectra and transmission

Waveguide throughput (laser energy exiting the waveguide divided by energy in the P1 focal spot) was measured by integrating CCD camera images of the P1 and guided modes, with the camera energy response calibrated by imaging the P1 focus with known laser energy and calibrated neutral density filters, then adjusted for the pixel spectral response. In this experiment, throughput could be measured only for P1 shots of energy >1.4 J because of several fixed P2/P1 energy ratios and the need for ~2 J of pre-compressed laser energy for the index-structuring (P2) beam. Under these

conditions, we measured guided pulse throughputs of $< 40\%$, and as low as $\sim 10\%$, depending on laser energy, waveguide density, and P1 pointing. Plasma wave excitation was responsible for most of the reduced transmission. This is demonstrated by simulations presented in Figure 3.3.
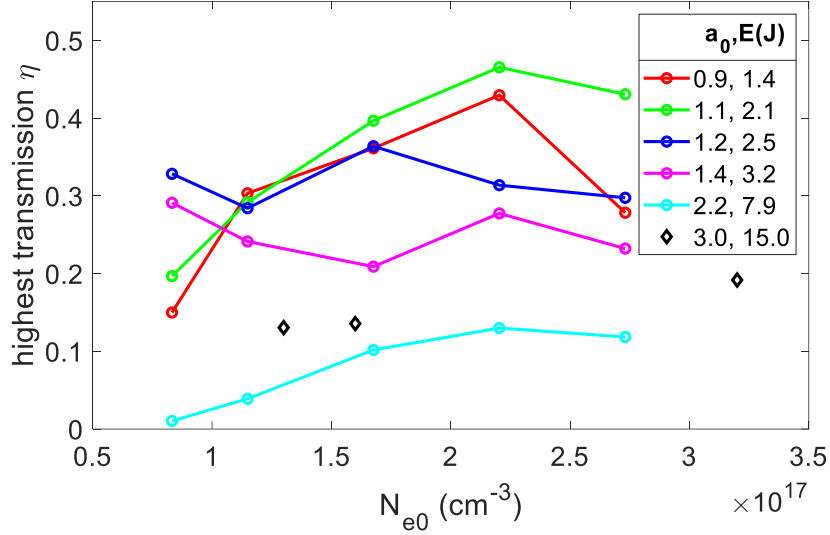
Figure 3.2: Self-waveguided transmission of P1 at different energies and on-axis plasma densities.

Figure 3.2 plots measured transmission versus waveguide central density N_{e0} for P1 energies in the range 1.4 - 15J (accompanying a_0 values were calculated using $\tau = 45$ fs FWHM and the P1 focal profile of Figure 3.1(a)). This shows a maximum transmission of $\sim 40\%$ for $a_0 \sim 1$ (P1 energy $\sim$ 1.4 J), with transmission decreasing to $\sim 10 - 15\%$ for $a_0 \sim 2 - 3$ (P1 energy $\sim$ 15 J). Experimental evidence of plasma wave excitation is shown in Figure 3.1(f), where an increasing fraction of the pulse spectrum is red-shifted for increasing a_0, signaling that the decreased transmission is due to energy being coupled into plasma waves.
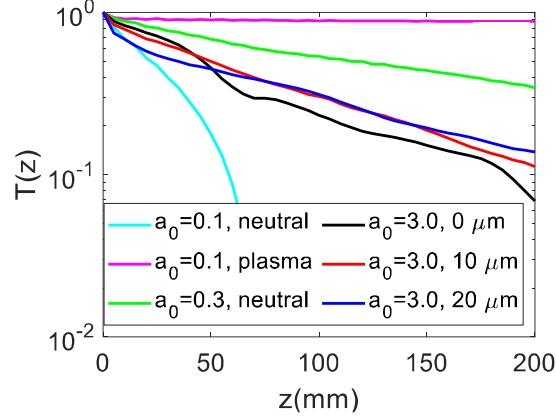
Figure 3.3: Simulated transmission curves. All simulations performed in WarpX with on-axis electron density $N_{e0} = 3.2 \times 10^{17} \, cm^{-3}$. 'neutral' indicates that the prepared index structure is formed by an expanded J_0-ionized plasma and the resultant neutral gas shock. 'plasma' indicates that the neutral shock has been pre-ionized. The offsets are transverse between the center of the drive pulse and center of the index structure.

The same dependence of transmission on laser intensity is observed in WarpX simulations of the experiment. In Figure 3.3 we consider P1 transmission for different drive pulse intensities and transverse offsets from the prepared index structure. We can see three key results in the transmitted pulse energy fraction $T(z)$ vs. propagation distance for $a_0 = 0.1, 0.3,$ and 3.0: (1) poor transmission for a laser intensity ($a_0 = 0.1$) insufficient to support self-waveguiding, but greatly improved for $a_0 = 0.3$, (2) high transmission even at low a_0 for pre-ionized index structures, and (3) significant laser pulse energy depletion into plasma waves, showing transmission consistent with our measured throughput down to $\sim 10\%$ at high energy. For the $a_0 = 3.0$ curves, the simulations show reduced transmission for the zero offset case owing to the higher on-axis laser field, resulting in greater self-steepening [47] and greater laser attenuation from plasma wave excitation.

81

3.3.2 Monomode and multimode guiding

We found that the range of accessible laser intensities and plasma density supported both monomode and multimode guiding. Figure 3.4(a)-(h) plot representative guided modes for various experimental conditions. The drive pulse profile is pictured in Figure 3.4(i) on a larger scale. The transmission from monomode to multimode guiding occurs with increases in injected pulse energy, waveguide density, or Bessel beam energy. The first two quantities lead to more tightly confining guides: increased drive pulse energy enables more complete ionization of the neutral shell and surrounding background neutrals, while increased waveguide density corresponds to a higher background gas density and a greater difference between core and cladding density. The tighter confinement means that higher order modes decay over $L_{1/e} > L_{guide} = 20$ cm, and survive to the waveguide exit [22]. Though the waveguide fundamental mode size w_{ch} is matched to the injected pulse, slight variations in alignment between the drive pulse and the J_0 beam lead to coupling into these higher order modes. Increasing Bessel beam energy well beyond that required for OFI in the central maximum leads to ionization in the secondary rings of the Bessel beam and a larger initial plasma column. As shown in [106], a larger diameter initial plasma column alters the expansion of the neutral shell, leading to a larger fundamental mode size. This means that the guide is no longer matched to the injected pulse, resulting in significant coupling into higher order modes (see panel (h)). We note that this interpretation is complicated by recent simulation results. This is discussed further in Sec. 4.2.
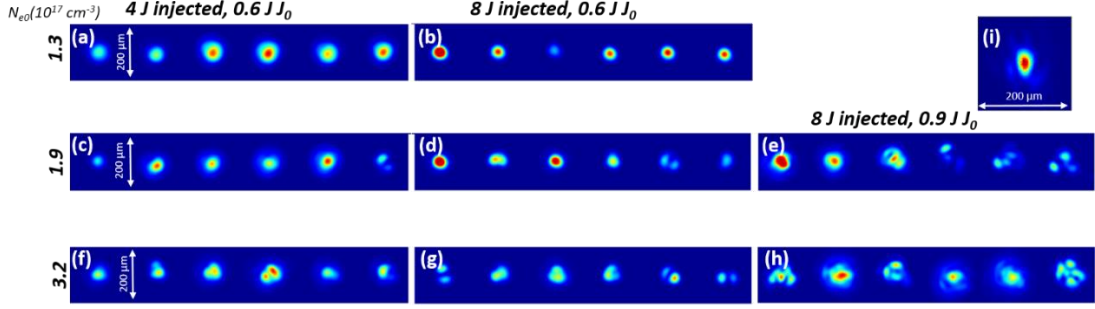
Figure 3.4: Guided modes at different conditions. **(a)-(h)** Guided modes for varying laser and plasma conditions, showing the transition from monomode to multimode guiding. All images were taken at the exit of a 20 cm waveguide, formed by self-waveguiding in prepared index structures in pure hydrogen. Although the self-waveguiding pulse was intense enough to excite plasma waves in the guide, there was no electron injection source for these measurements such as the N_2 ionization injection source demonstrated in [22]. All exit modes are plotted on the same spatial and intensity scales. **(i)** $f/25$ focal spot of injected drive pulse.

3.4 Dephasing limited shots with correlated diagnostics

The effects of P1 pointing variation on the accelerated electron bunch beam profile and energy spectrum are shown in Figure 3.5 for 43 consecutive shots with pulse energy 15 J $\pm$ 10%. Here, $N_{e0} = 3.2 \times 10^{17}$ cm^{-3} (as in Figure 3.1(g)(ii)) which using Eq. 1.12 corresponds to a dephasing length $L_d = \lambda_p/2(1 - \beta_\phi) \sim 10$cm, shorter than $L_{guide} = 20$ cm [47]. For the plasma waveguides of Figure 3.5, this dephasing length estimate is negligibly affected by the waveguide curvature's contribution ([89], Sec. 1.4.2) to the laser propagation wavenumber.
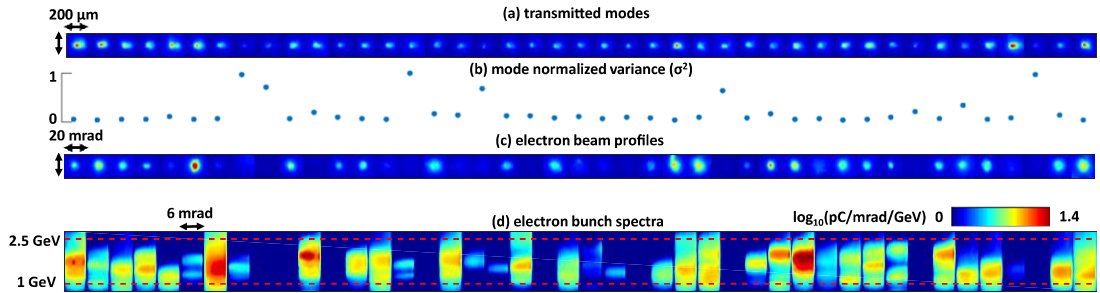
Figure 3.5: Mode and electron beam data for 43 consecutive shots at 1/8 Hz repetition rate. Laser 15 J, $\tau = 45\,fs$, plasma waveguide density $N_{e0} = 3.2 \times 10^{17}\,cm^{-3}$.**(a)** transmitted modes. **(b)** Normalized mode second moment σ^2 for each shot. **(c)**

Associated electron beam profiles measured at Lanex screen LA1 in Fig. 1, and **(d)** associated angle resolved electron bunch spectra plotted on a log energy scale.

While most injected pulses are guided (row (a)), the presence of a transmitted mode does not guarantee generation of a high quality electron beam. Beam generation is much more closely related to the quality of guiding, which we assess by the second moment $\sigma^2 = (\int dA\, I(\mathbf{r}))^{-1} \int dA |\mathbf{r} - \mathbf{r}_c|^2 I(\mathbf{r})$ of the transmitted intensity profile over the guide cross section, where $\mathbf{r}_c$ is the mode centroid. These are normalized and plotted in row (b), showing a clear correlation to the electron bunch quality variation in beam profile (row (c)) and energy (row (d)). For this run, the pickoff mirror M2 (see Figure 3.1) was placed in the beam path in order to enable simultaneous measurement of the waveguide laser exit mode and the electron beam profile and spectrum. Scattering in the ~1 cm path through the glass of M2 is calculated [169] to increase the beam divergence of the measured 1-2 GeV electron beams by ~4 mrad. It is important to emphasize that for all experiments discussed in this dissertation, there was no observed electron acceleration for waveguides generated in pure H_2 gas; only the H_2/N_2 gas mix yielded LWFA bunches, showing that our accelerator is purely ionization-injected.

3.4.1 Simulated effects of P1 coupling on injection and acceleration

While the data in Figure 3.5 give us some insight into shot to shot variations in guided mode and accelerated beam properties, they do not indicate the physical effects of shot to shot coupling variation on LWFA dynamics. In Figure 3.6, we look at PIC simulations to try and better understand the injection and acceleration process for drive pulses with different offsets. Panel (a) shows that increasingly off-axis P1 coupling

leads to increased guided mode centroid oscillation and reduced accelerated charge. We will discuss the dynamics of centroid oscillation and injection further in Chapter 4, but for this laser intensity and plasma density, we can see that the dominant effect is slight suppression of injection. Panel (b) shows simulated accelerated bunch spectra. While all are in the range $\sim 1 - 2.5$ GeV (limited by dephasing, since $L_d < L_{guide}$), and consistent with the measurements of Figure 3.5, the accelerated charge (integral of the spectra) decreases significantly with P1 coupling offset, as also seen in Figure 3.6(b) and in the measurements (Figure 3.5(a)-(d)). Interestingly, while the measured electron spectra (Figure 3.5(d)) show multiple peaks, the simulations show wide, continuous— spectra except for the 20 µm coupling offset case. The disparity between continuous spectra predicted by simulations and multi-peaked spectra observed experimentally will be discussed further below and Chapter 4.

(a)   **(b)**
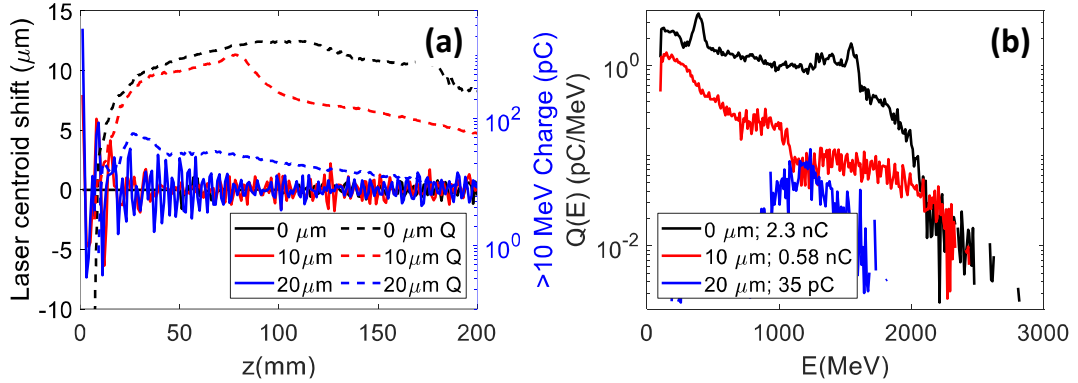
Figure 3.6: Offset coupling effect on injection and acceleration in dephasing-limited LWFA **(a)** Guided mode centroid oscillation and accelerated charge > 10 MeV for three P1 coupling offsets ($a_0 = 3.0$). **(b)** Accelerated bunch spectra for three P1 coupling offsets ($a_0 = 3.0$).

3.5 5 GeV electron acceleration

We achieved electron bunch acceleration up to a maximum of ~5 GeV by operating at lower plasma density. In this experiment, the mirror M2 was removed.

Figure 3.7 shows results from a plasma waveguide central density scan for $N_{e0} = (1.3 - 3.2) \times 10^{17}$ cm^{-3} and laser energy 11 J, spanning the transition from monomode to low order multimode guiding shown in Figure 3.1(g) and Figure 3.4. Notably, using higher laser energy of 15 J under these conditions resulted in the reduced peak electron energies seen in Figure 3.5, as will be further explained below and in Chapter 4. Figure 3.7(a) plots peak bunch energy and associated charge (in the highest energy peak) for all shots (92) in the density scan. This is overlaid by average peak energy vs. N_{e0}, showing good agreement with the expected $\Delta W \propto N_{e0}^{-1}$ scaling [16,40,181]. The charge measurements in all panels represent a lower bound due to the 1 mm entrance slit on the magnetic spectrometer (~0.3 mrad acceptance), employed to increase the energy resolution. The actual accelerated charge on a given shot could be up to ~100 times higher ([182], see Sec. 2.5.2). Angle-resolved spectra are shown in Figure 3.7(b), while spectrum lineouts and angle-resolved spectra for the highest energy shots (for $N_{e0} < 2 \times 10^{17}$ cm^{-3} , where $L_d > L_{guide} = 20$ cm) up to ~5 GeV are plotted in Figure 3.7(c).

The narrowest beams have ~milliradian divergence and the narrowest quasi-monoenergetic peaks have relative energy width of ~15%, the resolution limit of the spectrometer. The stability of P2 ensures a 5 μrad maximum tilt of the plasma waveguide axis and electron beam source (at the waveguide exit), while the spectrometer slit acceptance of 0.3 mrad × 6 mrad (slit width × slit length) gives an energy uncertainty of ~3% at 5 GeV ([182], Sec. 2.5.2). While the highest energy peaks in Figure 3.7(c) have comparable energy spreads, the shot-to-shot variation of charge and divergence is significant. Over all shots, we see no evidence of a trade-off among

the different beam parameters. We attribute the beam variations to fluctuations in P1 pointing and electron injection, as in Sec. 3.4 and discussed below. Some shots (panels 1-2) demonstrate $< \sim$pC charge bunches with $< \sim$mrad divergence and $\sim$15% energy spread, while others demonstrate greater than mrad divergence for bunch charges either $> \sim$10 pC (panel 4) or $< \sim$10 pC charge (panel 7).

While electron beam pointing into the spectrometer does not affect measured energies [182], it does affect the measured charge. Inspection of Figure 3.7(b-c) shows that the electron beam is often clipped at the ± 3 mrad edges of the lengthwise slit acceptance, suggesting >6 mrad variation in beam pointing along and across the slit. One possible explanation of this pointing variation is that deformation of the Bessel beam focus due to obstruction by the nozzle (Figure 2.5(a,a'), Sec. 2.2.2) may lead to a slight asymmetry in the prepared index structure, which slightly changes the matched mode size, inducing slight mode beating and wake oscillation at the end of the guide.
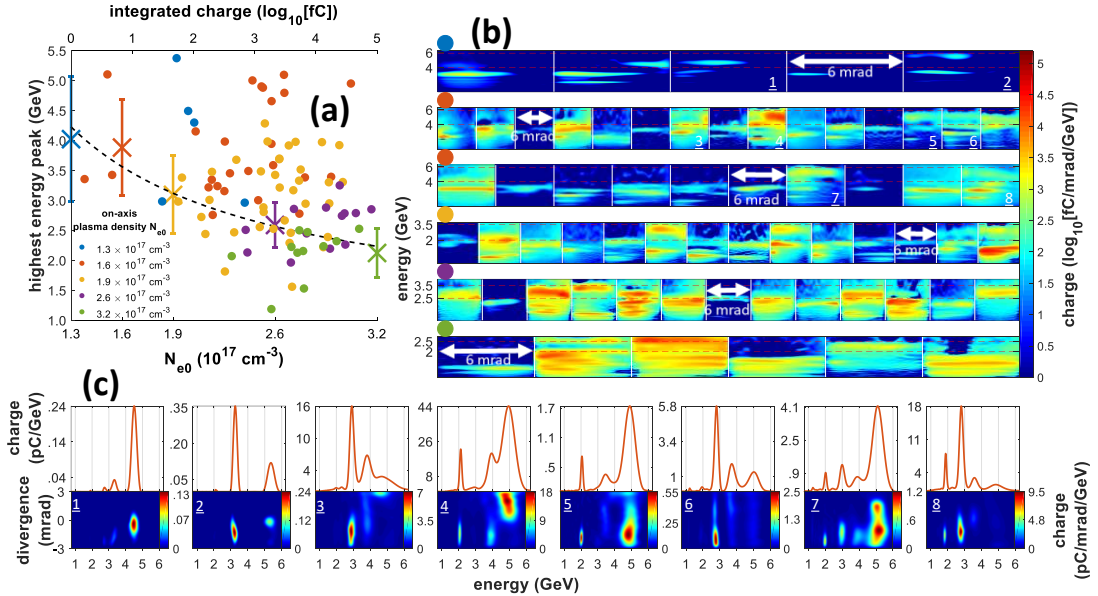
Figure 3.7: Density scan of 20 cm plasma waveguide showing increasing peak bunch energy for decreasing on-axis waveguide density N_{e0}. **(a)** Peak bunch energy and

associated charge in the highest energy peak for each shot (colored dots, plotted vs charge) and average peak energy (crosses, plotted vs. N_{e0}). The vertical bars are the standard deviations in energy. The dashed curve is a fit to $\Delta W \propto N_{e0}^{-1}$. **(b)** Angle-resolved electron spectra plotted on a linear energy scale corresponding to colored dots in (a). Each row represents all shots from a 20 shot series at each N_{e0} yielding acceleration. The energy scales are varied to allow closer inspection of the specific features. **(c)** Spectrum lineouts and angle-resolved spectra for shots with highest energy bunches. The two leftmost panels are for $N_{e0} = 1.3 \times 10^{17}$ cm^{-3} and the rest are for $N_{e0} = 1.6 \times 10^{17}$ cm^{-3}.

Electron bunches then reach the end of the guide at different phases in the wake on different shots, and exit the guide with trajectories at varying angles to the waveguide axis. This pointing variability contributes to the large measured charge fluctuations: even >1 mrad pointing fluctuations perpendicular to the slit would result in sampling of low intensity portions of the electron beam. However, even aside from instrumental effects of electron beam pointing, it is clear that there should be shot-to-shot bunch spectrum and charge variations for fixed nominal waveguide and laser parameters. As illustrated by the higher density experiment of Sec. 3.4, these variations are partially attributable to fluctuations in P1 pointing. But, in the low density experiments of Figure 3.7, where $L_d \gtrsim L_{guide}$, the highest energy electron spectra are significantly more sensitive to the axial location of electron injection, which is itself affected by the laser coupling offset and the details of the longitudinal variation of the plasma waveguide.

3.5.1 Causes and effects of localized injection

Insight into the effects of beam pointing and axial waveguide non-uniformity on electron injection is obtained from the WarpX particle-in-cell simulations [128], as shown in Figure 3.8. Accelerated bunch spectra for an axially uniform waveguide with $N_{e0} = 1.7 \times 10^{17}$ cm^{-3} ($L_d = 27$ cm, accounting for etching [40] as discussed earlier) are shown in Figure 3.8(a) for on-axis coupling of P1 with $a_0 = 2.0 - 3.0$. Broad,

88

relatively flat spectra are seen with highest energy in the range ~4-5 GeV. While this agrees with the maximum energy of the experiments, the experimental spectra show multiple peaks with quasi-monoenergetic structure. The broad spectra observed in the simulations originate from continuous ionization injection during guided propagation in the uniform waveguide, while more localized injection occurs in the experiment. The reduction in peak electron energy in going from $a_0 = 2.5$ to $a_0 = 3.0$ in Figure 3.8(a) is consistent with our observations of reduced acceleration at higher laser energy. This is likely due to laser depletion-induced dephasing, as discussed in Sec. 3.5.2.
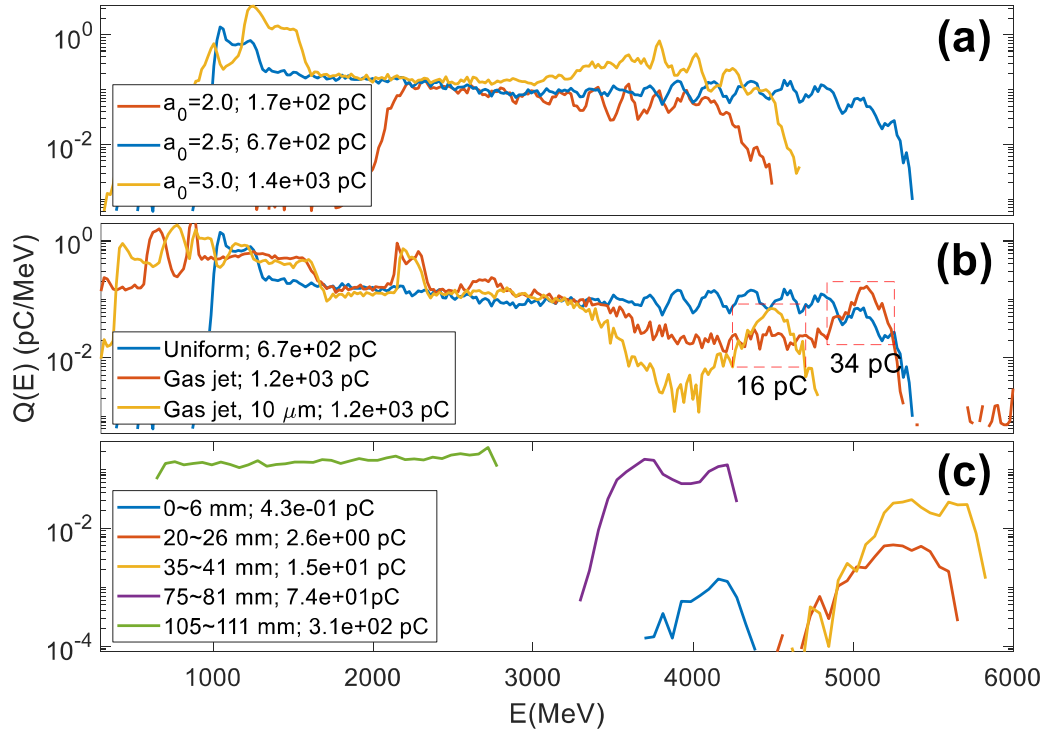
Figure 3.8: Particle-in-cell simulations using WarpX [128] of electron acceleration in 20 cm long plasma waveguide formed in 95% H_2 and 5% N_2. The guide is initialized with hydrogen fully ionized and nitrogen ionized to N^{5+} (see Appendix C). The charges shown are for electrons with energy > 300 MeV. **(a)** On-axis coupling of $a_0 = 2.0, 2.5, and 3.0$ pulses into axially uniform waveguide with $N_{e0} = 1.7 \times 10^{17} \ cm^{-3}$ ($L_d = 27 \ cm$). **(b)** Coupling of $a_0 = 2.5$ pulse (i) on-axis into uniform waveguide with $N_{e0} = 1.7 \times 10^{17} \ cm^{-3}$, (ii) on-axis into waveguide with on-axis waveguide density N_{e0} proportional to the longitudinal gas jet profile of Fig. 1(c) at 3 mm above the nozzle, and (iii) 10 μm off-axis into the same profile as (ii). Also shown is the charge

in the peaks of (i) and (ii), bounded in energy by the dashed boxes. **(c)** On-axis coupling of $a_0 = 2.5$ pulse into uniform waveguide with $N_{e0} = 1.7 \times 10^{17} \, cm^{-3}$ with restricted 6 mm sections of 5% N^{5+} placed successively at locations shown in the legend. The short 5% dopant region consists of a 1-mm upramp, a 4-mm plateau and a 1-mm downramp.

Shot-to-shot variation in localized injection likely occurs from a combination of P1 pointing fluctuations and axial nonuniformity of the plasma waveguide, with the latter originating from axial nonuniformity in the jet's gas density (as discussed in Sec. 2.3). As OFI-driven plasma ionization and heating is independent of gas density, the plasma waveguide transverse shape is z-invariant but the waveguide on-axis density N_{e0} (and the He-like nitrogen density) varies, and this affects electron injection. This is seen in Figure 3.8(b), where the electron spectra are different for a uniform guide and one where the on-axis density follows the measured gas jet density profile of Figure 3.1(c) (at 3 mm above the nozzle). Off-axis coupling of P1 by 10 μm into the gas jet index structure changes the electron spectrum even more substantially. Both the distribution and maximum energy are different than when the pulse is well-aligned, with the appearance of a quasi-monoenergetic peak centred near 4.5 GeV with ~10% spread, suggesting localized injection in this case. The tens of pC charges in these peaks are consistent with our measurements.

Detailed inspection of the simulation results shows that localized injection can be triggered by multiple contributing factors during the experiment. First, non-uniformity along the waveguide can lead to ionization injection assisted by sharp density gradients [73]. Second, toward the end of the plasma channel, laser pulse depletion may decrease the peak intensity below the barrier-suppression-ionization threshold of N^{5+} of $a_0 \sim 2.2$. Third, transverse offset coupling of the drive laser pulse

into the plasma waveguide can have several effects. One effect is that the transverse oscillation of the laser pulse centroid at the beginning of the waveguide will drive transverse oscillating plasma wakes, suppressing electron injection (see Figure 3.9 and discussion). Another is that the beating of the multiple transverse modes excited by off-axis injection can result in intensity spikes that trigger localized ionization injection and minima that suppress it. The dynamics of mode beating induced ionization injection are discussed more fully in Chapter 4.

The effect of mode oscillation on the wakes driven by pulses with coupling offset is shown in Figure 3.9. The conditions are those of Figure 3.8(b) (gas jet waveguide, $a_0 = 2.5$). Snapshots of the wakefield and its projections simulated using WarpX are shown at $z = 15$ mm and $z = 55$ mm for the cases of on-axis coupling and a transverse coupling offset of 10μm. Here $(x, y, \xi) = (0,0,0)$ corresponds to the laser beam axis and the centroid of the laser pulse in the simulation window moving at the laser pulse group velocity. On-axis coupling leads to transversely symmetric wakefields, with the symmetry persisting over the full length of the waveguide. This is seen most clearly in the projection into the xy plane of the symmetric plasma wake density near the back of the first potential bucket at $\xi = 53$ μm, the centre of the accelerated electron bunch (Figure 3.9(a) and (c)). A coupling offset of 10 μm, however, leads to transverse wake asymmetry that persists as long as higher order mode(s) are confined (here, mainly the (0,1) mode), as seen in the same xy projection (for $\xi = 53$ μm) at $z = 55$ mm (Figure 3.9(b) and (d)). Also notable is the presence of an on-axis electron bunch of much larger charge in the case of zero P1 coupling offset (compare panels (c) and (d), where in (d) the lower charge bunch is located off-axis).

91

These cases correspond to the two "gas jet" electron spectra shown in Figure 3.8(b). This is consistent with the electron bunch fluctuations associated with P1 pointing variations discussed throughout this dissertation. The specific dynamics of electron injection due to mode beating are explored in more detail in Chapter 4.
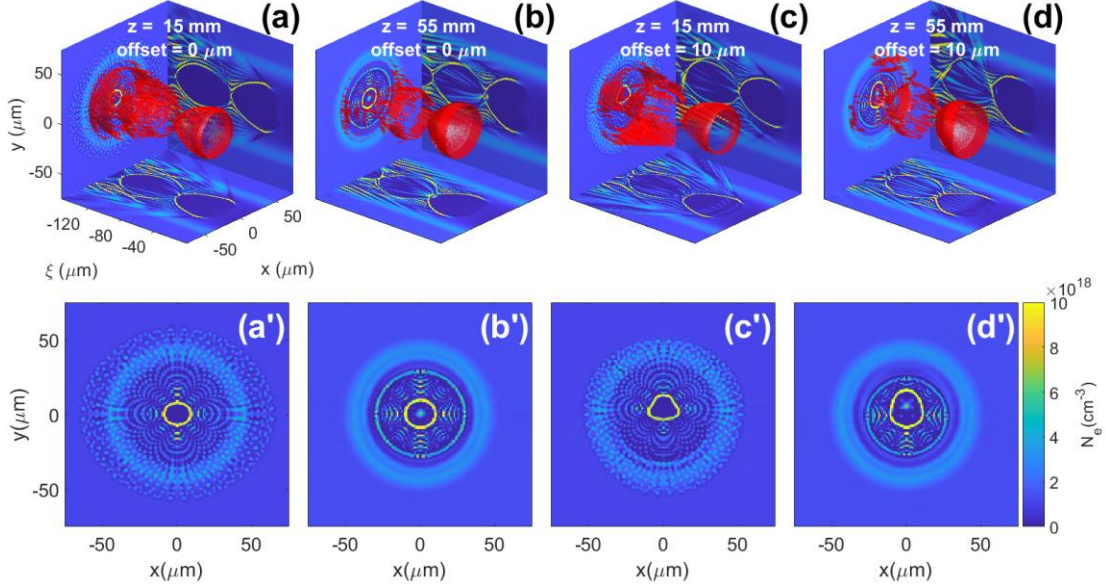
Figure 3.9: Asymmetric wakes driven by off-axis coupling. WarpX simulation assessing the effect on the plasma wake of off-axis drive pulse (P1) coupling, using the parameters of Figure 3.8(b). Here $(x, y, \xi) = (0,0,0)$ corresponds to the laser beam axis and the centroid of the laser pulse. The red contours are for $N_e = 9.4 \times 10^{18} \, cm^{-3}$, the xy projection is for $\xi = 53 \, \mu m$ (centre of the accelerated electron bunch), and the $x\xi$ and $y\xi$ projections are for $y = 0$ and $x = 0$ respectively. **(a)** No P1 coupling offset, $z = 15 \, mm$, **(b)** 10 μm P1 offset, $z = 15$ mm, **(c)** No P1 coupling offset, $z = 55 \, mm$, **(d)** 10 μm P1 offset, $z = 55 \, mm$. **(a')-(d')** xy projections of electron density in (a)-(d).

Though incorporations of some real-world non-idealizations in Figure 3.8(b) leads to results which slightly better line up with experimental observations, the best replication of experimental results occurs when electrons are injected over a restricted longitudinal region. In Figure 3.7(c), electron bunches are accelerated at multiple energies, with final electron energy spread in each peak <10% and total charge on the

order of 10 pC. Here, localized injection is forced by confining nitrogen dopant to short 6-mm sections successively placed at 5 locations along an axially uniform plasma waveguide. Note that the maximum energy of $> \sim 5$ GeV occurs for electron injection 2-4 cm after the beginning of the waveguide rather than near the guide entrance. This is because some propagation distance is needed for stabilization of the injected mode and its driven wakefield, and for intensity enhancement by self-steepening, which triggers ionization injection. The short section length is chosen to correspond to the smallest scale of axial gas density variation in Figure 3.1(c), qualitatively modeling the effect of axial gas density variations on producing quasi-monoenergetic structure in our measured electron bunches. It is also the spatial scale associated with mode beating between the fundamental and first azimuthal mode (see Chapter 4).

3.5.2 Simulated pulse evolution and depletion

To visualize the evolution of the laser pulse and acceleration process along the waveguide for continuous versus localized ionization injection, we examine further the simulation results of Figure 3.8. Figure 3.10(a) plots the electron energy spectrum, peak normalized vector potential a_0, and total accelerated charge (at >300 MeV) vs. z for the case of Figure 3.8(a) (injected $a_0 = 2.5$, continuous ionization injection). Figure 3.10(b) plots the same quantities for the case of Figure 3.8(c) (injected $a_0 = 2.5$, ionization injection restricted to $z = 35 - 41$ mm). In both cases (Figure 3.10(a) and (b)), the slight mismatch between the injected mode and the waveguide (including the effect of the abruptly excited plasma wake on guiding) causes oscillations in a_0 that settle down by $z \sim 35$ mm, after which the stabilized mode undergoes steady self-steepening, reaching $a_0 > 3$ near $z = 10$cm. Figure 3.10(a) (N$_2$ dopant everywhere),

little charge is injected in the oscillation region and then charge is injected continuously. The injection rate increases near $z = 10$ cm (peak of self-steepening) and then turns off near $z = 16$ cm when depletion and beam loading causes a_0 to dip below ~ 2.2, (the ionization threshold for N^{5+}). Continuous ionization injection over most of the waveguide results in a large energy spread to ~ 5.5 GeV with a beam divergence of ~ 1 mrad and a total charge >0.5 nC.
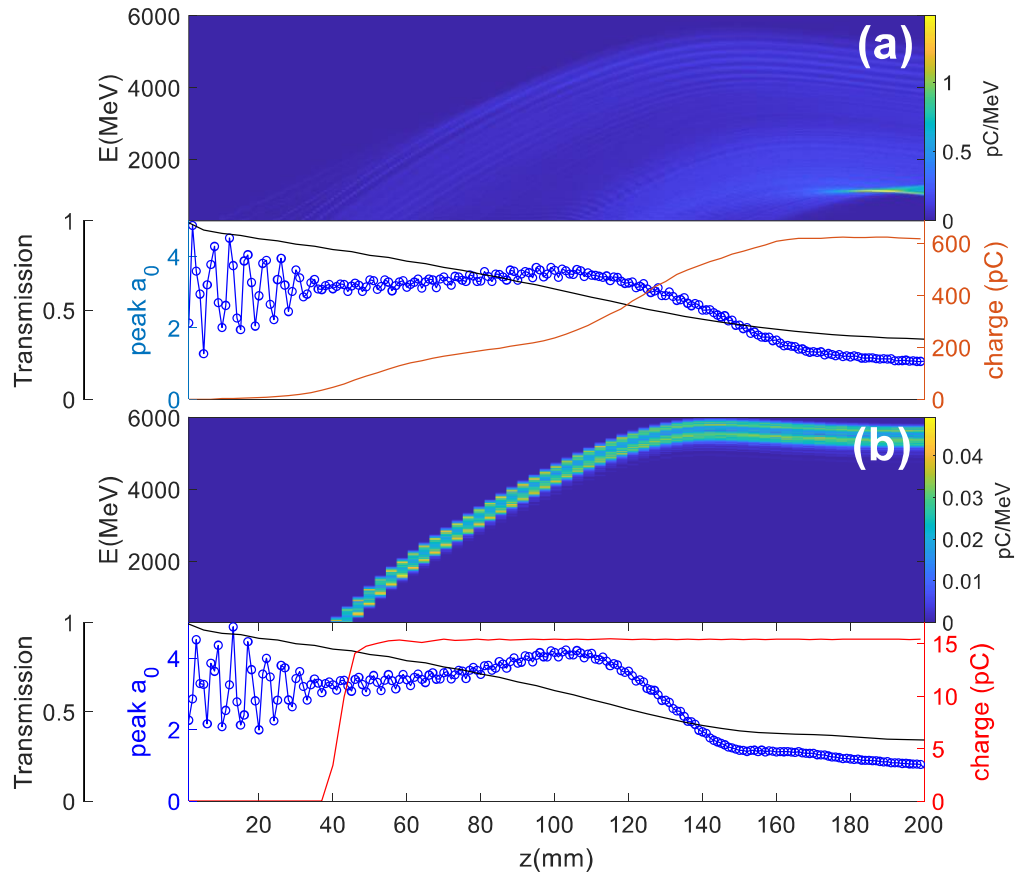
Figure 3.10: Laser spot and accelerated charge evolution for global vs. localized dopant. Electron spectrum, normalized vector potential a_0, total accelerated charge (>300 MeV), and guided pulse energy transmission $T(z)$ vs. z for **(a)** injected $a_0 = 2.5$, continuous 5% N_2 dopant, $N_{e0} = 1.7 \times 10^{17}\ cm^{-3}$, and **(b)** injected $a_0 = 2.5$, 5% N_2 dopant in $z = 35 - 41\ mm$, $N_{e0} = 1.7 \times 10^{17}\ cm^{-3}$.

By contrast, with the N_2 dopant restricted to $z = 35 - 41$ mm, injection occurs only near the end of that range after the mode stabilizes. No further injection occurs

downstream in the pure hydrogen plasma waveguide, even as the laser continuously self-steepens to $a_0 > 3.5$ near $z = 10$ cm. The pulse amplitude then drops, owing to depletion. The locally injected bunch is continually accelerated to ~ 5.5 GeV until depletion-induced dephasing occurs by $z = 14$ cm. The output bunch is in a ~10% FWHM quasi-monoenergetic peak with beam divergence ~0.25 mrad and charge ~15 pC. From the scalings in [40], the peak a_0 curves of Figure 3.10 suggest that injection and acceleration is initially in the nonlinear regime, followed by acceleration and dephasing in the quasi-linear regime once pump depletion reduces a_0.

As discussed in prior work, pump depletion can effectively shorten the dephasing length in LWFA [16,17,44,47,183]. This is caused by the wake-induced laser red shift that slows down the pulse group velocity and therefore the plasma wake phase velocity. The group velocity of an undepleted laser pulse in a plasma waveguide is [89,93] $v_{g0}/c \approx 1 - \omega_{p0}^2/2\omega_0^2 - 1/(k_0 w_{ch})^2$, which corresponds to the plasma wake phase velocity v_{p0}/c in the undepleted case. By replacing the initial central laser frequency ω_0 and wavenumber k_0 by their instantaneous average in the co-moving simulation frame, $\langle \omega \rangle$ and $\langle k \rangle$, one can account for the pump depletion-induced slowdown of plasma wakes in the plasma channel [16,17,44,47,183]. We demonstrate this correction by 3D PIC simulation in WarpX and show that pump depletion can reduce the effective dephasing length during propagation in long plasma waveguides.
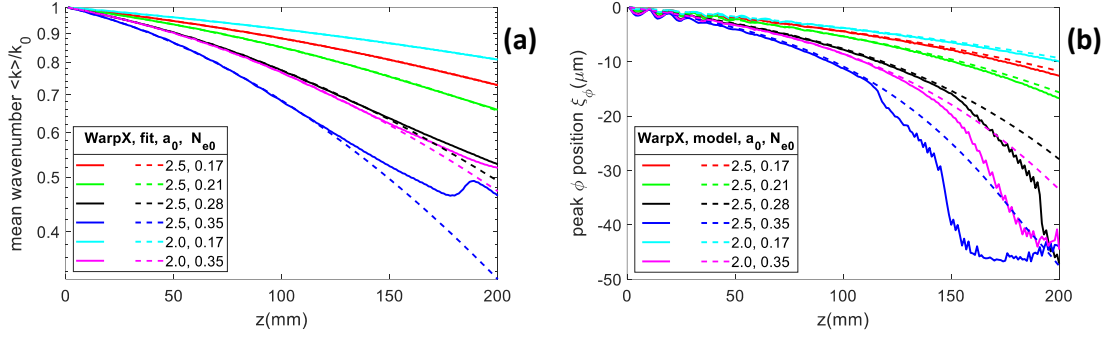
Figure 3.11: Depletion induced dephasing. (a) Mean normalized wavenumber $\langle k \rangle / k_0$ of the laser pulse along the plasma waveguide. The solid lines are simulation results and the dashed lines are exponential fits $\langle k \rangle = k_0 \exp(-z/L_{pd1} - z^2/L_{pd2}^2)$. N_{e0} is in units of $10^{18} cm^{-3}$. (b) Position ξ of the peak potential of the plasma wake bucket following the laser pulse in a frame moving at the group velocity v_{g0} of the undepleted laser pulse. The reduced plasma wave phase velocity effectively shortens the LWFA dephasing length. Solid curves: WarpX simulation. Dashed curves: model fit.

Figure 3.11 shows the mean normalized laser wavenumber $\langle k \rangle / k_0$ in the moving simulation window along the waveguide for several laser and plasma conditions (solid lines). It is seen that for a given waveguide central density N_{e0}, $\langle k \rangle / k_0$ drops increasingly with propagation for larger a_0 (increased red shifting), with saturation occurring for the blue curve and incipient saturation for the black and pink curves. Those curves correspond to the higher N_{e0} cases. To establish the connection between $\langle k \rangle / k_0$ and pump depletion, we fit $\langle k \rangle$ as $\langle k \rangle = k_0 \exp(-z/L_{pd1} - z^2/L_{pd2}^2)$ and compare with the simulation result from WarpX. The result is plotted as dashed lines in Figure 3.11(a). The quadratic term in the exponent is to account for faster depletion due to pulse steepening, which is not included in the quasistatic approximation in [44]. We take L_{pd1} as the depletion length and in all the cases $L_{pd1} \sim 10 k_0^2 / k_p^3$, consistent with Eq. (10) in [44], where k_p is the plasma wavenumber in each case.

96

This reduction of the drive pulse wavenumber results in a reduced wake phase velocity. To see the depletion-induced plasma wake slowdown, in Figure 3.11(b) we plot the wake position (taken as the location ξ_ϕ of the peak wake potential after the laser pulse) in the co-moving simulation window with $v_{window} = v_{g0}$. Increasing a_0 from 2.0 to 2.5 for fixed waveguide density is seen to increase the wake lag, as does increasing the plasma density for fixed a_0. We model this wake lag as a correction

$$\Delta v_p/c = (v_{p0} - v_p)/c = \omega_{p0}^2/2\omega_0^2 \left(1 - \omega_{p0}^2/\langle\omega\rangle^2\right) + 1/(k_0 w_{ch})^2 \left(1 - k_0^2/\right.$$

$\left.\langle k\rangle^2\right) + \alpha\sqrt{a_0}(\omega_p/\omega_0)^{3/2}$, with fitting parameter $\alpha = -0.022$. As the laser pulse self-steepens along propagation, the energy depletion rate increases and $\langle k\rangle$ drops faster. This, combined with the $\langle k\rangle^{-2}$ dependence in the correction term, causes ξ_ϕ to decrease faster along propagation. The model fits best for the lower N_{e0} or a_0 cases (cyan, red, and green curves), where the accelerated charge is low and the beam loading effect is not significant over the whole propagation length. For the higher a_0 or N_{e0} cases (black, blue and magenta curves), the model still fits well until beam loading effect significantly affects the wake structure. In summary, we show through PIC simulations that pump depletion contributes to dephasing during laser propagation over long distances and the depletion length is a function of both a_0 and N_{e0}.

Chapter 4: Guided mode evolution and localized ionization injection in meter-scale multi-GeV LWFAs

4.1 Introduction

In Chapter 3, we discussed the first implementation of self-waveguiding pulses in all-optical laser wakefield accelerators (LWFAs) to produce multi-GeV electron bunches with quasi-monoenergetic peaks of >15% energy spread and ~mrad divergence. We presented evidence that electron injection into the wake via ionization injection of N^{5+} occurs over short ($\lesssim$ cm) longitudinal regions multiple times during propagation. Further study reveals that the mechanism behind this localized injection is longitudinal variation in drive pulse intensity due to both linear and nonlinear effects.

In this chapter we present experiments and simulations demonstrating that the laser intensity oscillations, which are responsible for repeated ionization injection and the multi-peaked electron spectra shown in Chapter 3, arise from a universal mode beating effect—active whether or not the injected laser is mode matched to the guide. The spectra have no extended low energy tails containing most of the charge as in comparable capillary-based multi-GeV experiments [23].

From PIC simulations of self-waveguided LWFAs with various laser-plasma conditions, we identify three phases of pulse propagation [74]: (I) coupling mismatch induced mode beating resulting in high amplitude intensity variations, (II) mode beating arising from ponderomotive channel modification resulting in low amplitude intensity variations, and (III) depletion and nonlinear deterioration of the pulse. Periodic injection during the first two phases results in a stratified electron energy distribution within the wake, and can produce an electron beam comprised of multiple

bunches with narrow energy spreads at different energies dependent on the injection location. Depending on the extent of propagation during phase III, this structure can either be preserved until the end of the waveguide, resulting in the characteristic multiply peaked spectra recorded in our experiments, or it can be distorted, resulting in broad, continuous spectra.

We demonstrate that this picture is well matched to experiments performed under a broad range of conditions (including those discussed in Chapter 3). Furthermore, we present experimental results showing that localizing a short (~ cm-scale) dopant region within phase I or II can dramatically reduce the number of periodic injection locations. This has been achieved to produce electron beams with single monoenergetic ($\Delta E/E \gtrsim 7\%$) peaks with central energy $\lesssim 2$ GeV. We also present evidence that plasma channel properties can be used to modify guided pulse properties such as waist size and intensity thereby inducing ionization injection when it otherwise might not have occurred.

4.2 Three phase model of intense pulse evolution in a low-density plasma waveguide LWFA

To identify the important physical effects for ionization injection and acceleration, Figure 4.1 presents results from a representative WarpX particle-in-cell (PIC) simulation [128] for the parameters of our experiments, using a 95%/5% H_2/N_2 gas mix. The figure shows pulse evolution and electron acceleration for a LWFA drive pulse (blue curve: $a_{0i} = 2.0, \tau_{FWHM} = 35$ fs, $w_0 = 30$ μm) injected into a 20 cm waveguide with on-axis plasma density $N_{e0} = 2.0 \times 10^{17}$ cm^{-3} and $w_{ch} = (\pi r_e \Delta N_e)^{-1/2} = 20$ μm. Here w_{ch} is the $1/e^2$ intensity radius of the lowest order self-

waveguided mode of the structure shown in Fig. 1(d) [89,90,93], $r_e = e^2/mc^2$ is the classical electron radius, and $\Delta N_e = N_e(w_{ch}) - N_e(0)$. The injected pulse is therefore mode-mismatched. Figures 4.1(a) and 4.1(b) plot the peak normalized vector potential and electron energy spectrum vs. z. The spectrum shows a striated energy structure caused by periodic ionization injection of electrons from N^{5+}; by comparing panels it is seen that the individual striations are correlated with the a_0 oscillations. With increasing z, the striations bend over as dephasing begins, and by $z = 20$ cm the final spectrum of Figure 4.1(c) shows multiple quasi-monoenergetic peaks.
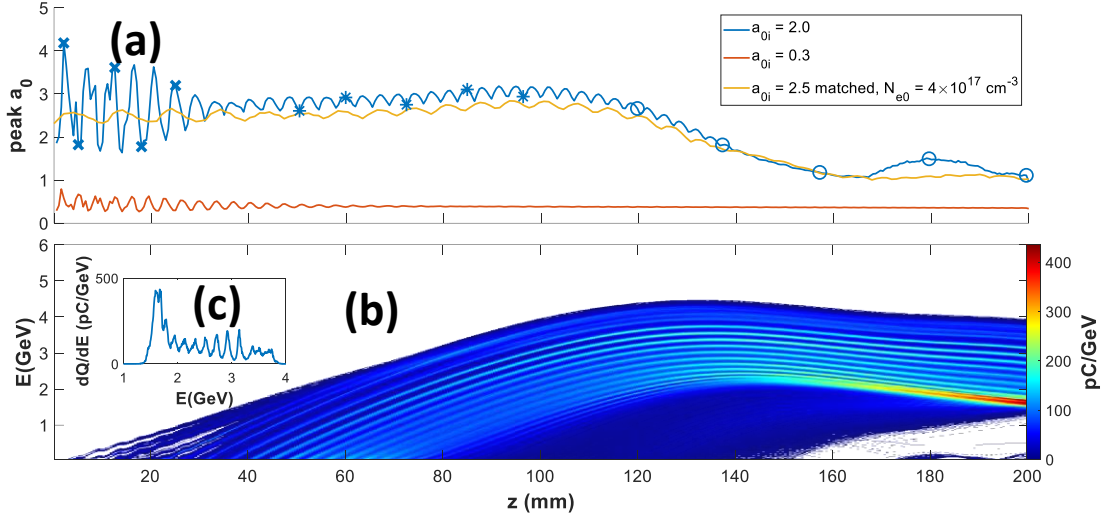
Figure 4.1: WarpX [128] particle-in-cell simulations of drive pulse evolution in a waveguide with $w_{ch} = 20\ \mu m$. Gas composition is 95%/5% H_2/N_2 and the simulation xyz grid is 256×256×4096 (256μm×256μm×204.8μm). **(a)** Peak laser field a_0 vs. propagation distance for: (i) mismatched input field $a_{0i} = 2.0$, $w_0 = 30\ \mu m$, $\tau_{fwhm} = 35\ fs$, $N_{e0} = 2.0 \times 10^{17}\ cm^{-3}$ (blue line), (ii) mismatched $a_{0i} = 0.3$, $w_0 = 30\ \mu m$, $\tau_{fwhm} = 35\ fs$, $N_{e0} = 2.0 \times 10^{17}\ cm^{-3}$ (orange line), and (iii) matched $a_{0i} = 2.5$, $w_0 = 30\ \mu m$, $\tau_{fwhm} = 35\ fs$, $w_{ch} = 30\ \mu m$, $N_{e0} = 4.0 \times 10^{17}\ cm^{-3}$ (gold line). Labels I, II, and III denote the three characteristic propagation stages. Labels (×), (∗), and (o) denote the locations of the frames displayed in Figure 4.6(a)-(c). **(b)** Electron spectrum vs. propagation distance corresponding to the blue curve of (a). **(c)** Final integrated spectrum.

We identify three phases of pulse evolution as marked on the blue curve: (I) large amplitude intensity oscillations during early propagation, which quickly

transition to (II) sustained oscillations at lower amplitude, followed by (III) rapid intensity decline and cessation of oscillations. Periodic ionization injection and the striated bunch energy structure occurs during stages I and II; the degree of dephasing between the electron bunches and the plasma wake during stage III determines whether or not this structure is preserved.

This characteristic behavior is observed in simulations for a wide variety of laser and plasma conditions. Figure 4.2(a)-(d) plots the integrated spectrum vs. propagation distance for several different sets of laser-plasma parameters. In panel(a), the prepared index structure is the same as in Figure 4.1, but the drive pulse intensity is lowered to $a_0 = 1.8$. Despite the lower intensity, the behavior is largely similar to Figure 4.1: some electrons are successfully injected during the early portion of propagation, but most are injected from $z \approx 5 - 10 \ cm$, where there is clear periodic enhancement and suppression of injection. After $z \approx 10 \ cm$, injection decreases and the accelerated bunches begin to dephase after the intensity begins to dramatically decrease at $z \approx 13 \ cm$. As with the slightly higher intensity drive pulse in Figure 4.1, this leads to some blurring of the stratified spectra, but multiple quasi-monoenergetic peaks are still present in the spectrum at the end of propagation.

In Figure 4.2(b), where the drive pulse intensity is $a_0 = 1.5$ and on-axis plasma density is $N_{e0} = 4.0 \times 10^{17} \ cm^{-3}$, the contrast between enhancement and suppression of injection is quite stark for $z \approx 2 - 6 \ cm$. However, at the higher density, injection stops and dephasing begins much earlier during the propagation (before $z \approx 10 \ cm$). This leads to significant distortion of the stratified energy distribution. At the end of

propagation, only one clear quasi-monoenergetic peak remains on top of a much broader pedestal.

Introducing spatial offset between the drive pulse and prepared index structure increases coupling into higher order azimuthal modes and affects the process of periodic injection during phase I. In Figure 4.2(c), the laser intensity and plasma density are the same as (b), but there is a $6\ \mu m$ transverse offset between the drive pulse and prepared index structure. This results in a later onset of high-contrast periodic injection ($z \approx 4 - 6\ cm$), with lower maximum energy gain before dephasing leads to blurring of the stratified spectrum. Figure 4.2(d) features the same plasma density and transverse offset, but with a lower intensity drive pulse ($a_0 = 1.3$). There is less periodic injection with the lower intensity and the structure is quickly lost as the electrons dephase.

Surprisingly, transverse offset can enable injection under conditions for which it does not otherwise occur. Figure 4.2(e) plots the evolution of a_0 and injected charge vs. propagation distance for the same laser intensity and plasma density as panel (d), but with no transverse offset between the drive pulse and prepared index structure. There is no significant injection observed during the well-aligned case, for which maximum a_0 and electrons with energy between 5-25 MeV (as an analogue for injected charge) are plotted in panel (e).
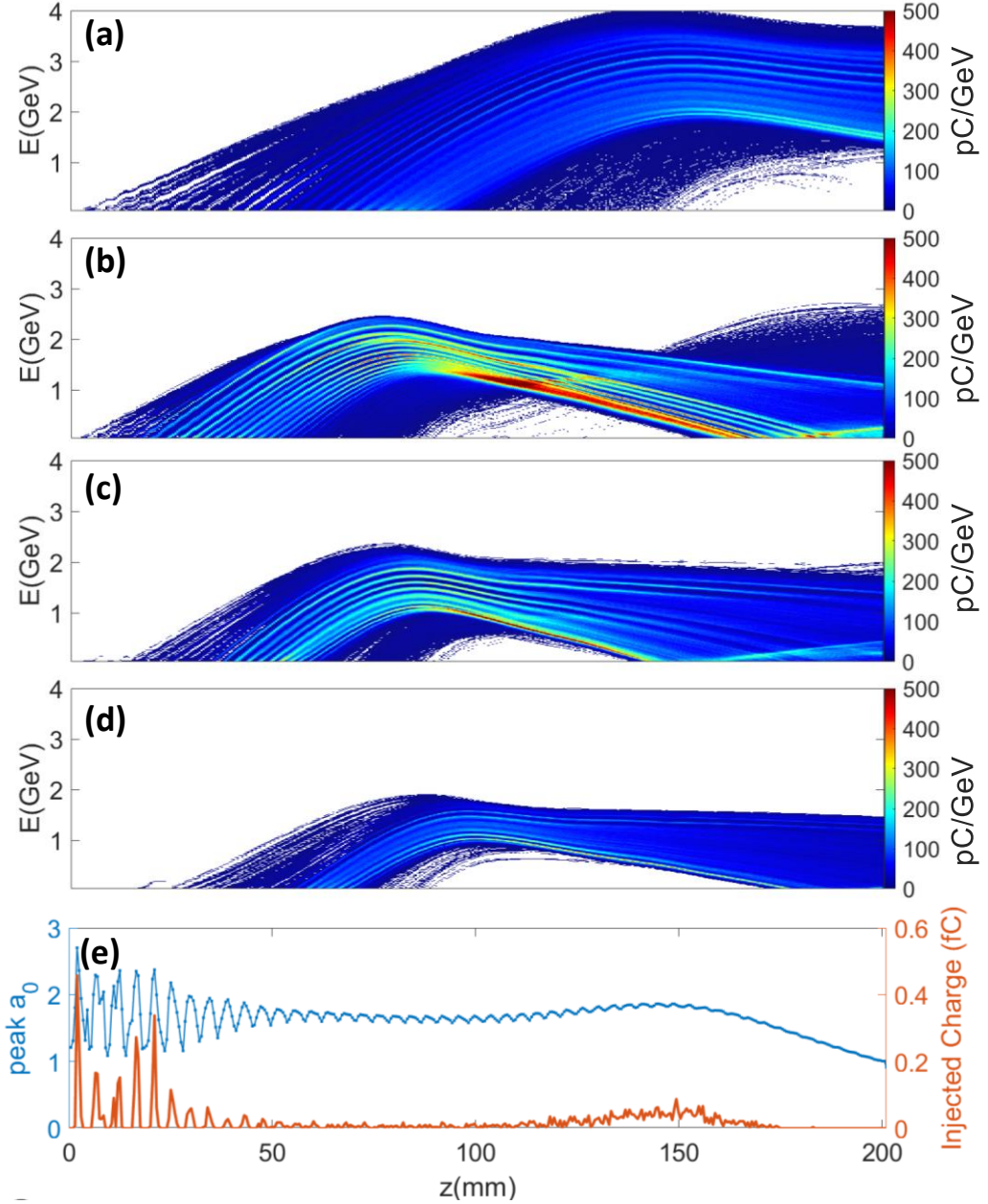
Figure 4.2: Accelerated electron and intensity evolution for different accelerator conditions. **(a)** $a_0 = 1.8, N_{e0} = 2.0 \times 10^{17} \, cm^{-3}$ with a uniform longitudinal prepared index profiled. **(b)** $a_0 = 1.5, N_{e0} = 4.0 \times 10^{17} \, cm^{-3}$ with a uniform longitudinal prepared index profile. **(c)** $a_0 = 1.5, N_{e0} = 4.0 \times 10^{17} \, cm^{-3}$ with a uniform longitudinal prepared index profile with the drive pulse offset $6 \, \mu m$ from the center of the structure. **(d)** $a_0 = 1.3, N_{e0} = 4.0 \times 10^{17} \, cm^{-3}$ with a uniform longitudinal prepared index profile with the drive pulse offset $6 \, \mu m$ from the center of the structure. **(e)** peak a0 (left axis) and injectable charge (right axis) vs. propagation distance for) $a_0 = 1.3, N_{e0} = 4.0 \times 10^{17} \, cm^{-3}$ with a uniform longitudinal prepared index profile and no offset. For all conditions the drive pulse has $w_0 = 30 \, \mu m, \tau_{FWHM} = 35 \, fs$ and is mismatched to the $w_{ch} = 20 \, \mu m$ channel.

103

Figure 4.3 plots a_0 vs z for several drive pulses with varied a_{0i} ($w_0 = 30\ \mu m, \tau_{FWHM} = 35\ fs$) propagating in pure H$_2$ channels with $N_{e0} = 3.4 \times 10^{17}\ cm^{-3}$ and $w_{ch} = 20\ \mu m$. For these simulations, there were no electrons injected into the wake, indicating that ionization injection of N^{5+} was indeed the source of accelerated electrons in the simulations for Figures 4.1 and 4.2. Despite the lack of injection, the drive pulse clearly undergoes the same characteristic evolution as in Figures 4.1(b) and 4.2(e).
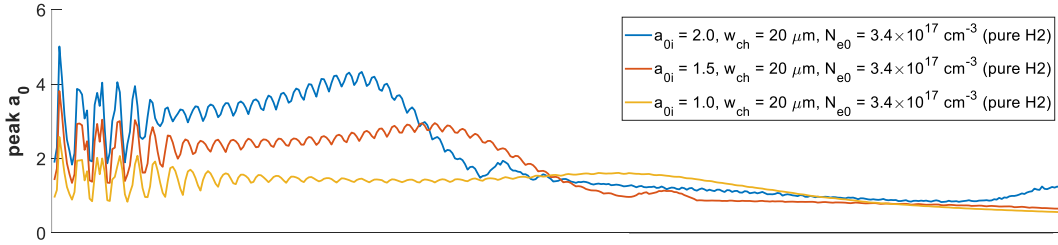
Figure 4.3: Peak a_0 vs. z for mismatched injection of varying intensity pulses with $w_0 = 30\ \mu m,\ w_{ch} = 20\ \mu m,\ and\ \tau_{fwhm} = 35\ fs$ in a pure hydrogen plasma waveguide.

The periodic oscillations in stages I and II are highly suggestive of beating between different plasma waveguide modes . However, the stark shift in the amplitude and uniformity of the oscillations suggest that there is a difference in the specific modes which are involved during each phase. Secs. 4.2.1 and 4.2.2 will explore the origin of the beating in each phase.

4.2.1 Phase I mode beating due to pulse and channel mismatch

For the blue curve in Figure 4.1(a), the $w_0 = 30\ \mu m$ Gaussian drive pulse is mismatched to the prepared index structure, which after ionization of the cladding supports a fundamental mode of $w_{ch} = 20\ \mu m$ [89], resulting in coupling into higher order modes of the waveguide. An obvious explanation for the initial intensity

oscillations is beating between the fundamental and higher order modes propagating

through the waveguide. Since the pulse is well-aligned to the waveguide, this coupling

will strongly favor higher order radial modes over azimuthal modes [89,184]. To

examine the mode structure of the waveguides generated by self-waveguiding pulses,

we employ the technique discussed in Sec. 1.4.2 and [89,90].
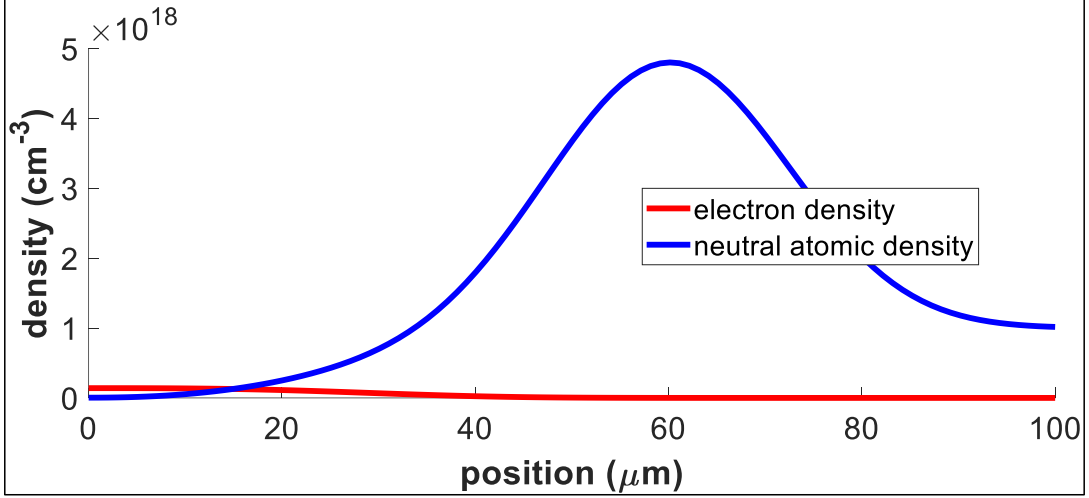
Figure 4.4: Electron and neutral density profiles forming the prepared index structure corresponding to the plasma waveguide structure used in our simulations.

In Figure 4.4, we plot the electron and neutral density profiles forming the

prepared index structure used for the simulations discussed in this chapter. The profile

has a higher magnitude neutral shock with the peak located at a larger radius than that

employed in the experiments discussed in this chapter and in Chapter 3. However, for

$r \lesssim 40 \, \mu m$, it is a reasonable approximation, with similar mode structure.

Unfortunately, for the high intensity of the self-waveguiding pulses used in our

experiments, ionization extends far outside the neutral column and makes direct

extraction of the plasma density profile via Abel inversion of interferograms difficult.

So we are forced to model ionization of the neutral gas in the prepared index structure.

Assuming a Gaussian drive pulse with peak intensity $I \sim 10^{19} \, W/cm^2$, we expect

sufficient intensity for OFI of hydrogen out to $r \simeq 100 \, \mu m$. Thus, we model ionization of the neutral gas out to this radius in the fully ionized profile for mode calculation. All of the PIC simulations and mode analysis is performed using a plasma profile derived from the prepared index structure in Figure 4.4 under this assumption.

As described in Sec. 1.4.2, the bound mode spectrum is calculated by identifying peaks in the resonance function, η. Figure 4.5 plots the η vs. β curves for $m = 0$ and $m = 1$ modes of the channel used in the blue curve of Figure 4.1(a). The spatial period of mode beating between different modes, $\Lambda = 2\pi/(\beta_{\rho_1,m_1} - \beta_{\rho_2,m_2})$, is shorter when the propagation numbers are further apart, and longer when they are close together. The beating periods for different modes are listed in the inset table. Each mode is labelled with its attenuation length. The calculated $\Lambda = 4.4 \, mm$ beating period between the $(0,0)$ and $(1,0)$ modes is in good agreement with the $\Lambda_I = 4.5 \, mm$ period observed during phase I, but not for the beating period of $\Lambda_{II} = 3.5 \, mm$ during phase II.

Given the long attenuation lengths identified in Figure 4.5, we might expect significant beating throughout the entire propagation length. However, in Figure 4.1(a), the characteristic large-amplitude variations in intensity present during phase 1 dissipate after just a few centimeters of propagation, yielding to the more constant and lower-amplitude phase II beating (which has a different period than the $(0,0) - (1,0)$ beating frequency observed during stage I). We note that the intensity evolution during phase I is undersampled in Figure 4.1(a) and similar plots due to memory constraints, and so some of the highest frequency variations in pulse intensity are poorly resolved.
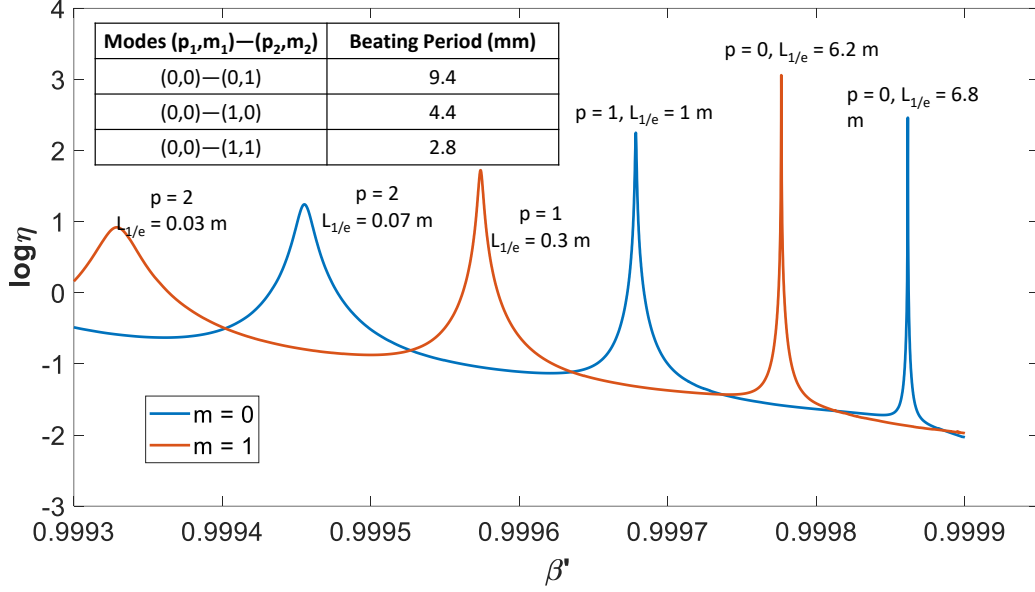
Figure 4.5: Calculated η $vs.$ β curves for $m = 0$ and $m = 1$ for the channel employed in the blue curve of Figure 4.1(a). The $\rho = 0$ mode for each case has the highest β value, with the peaks at decreasing β corresponding to modes of increasingly higher radial number. The modes are labelled with their attenuation lengths and the table in the upper right gives the beating period between the indicated modes.

The rapid dissipation of phase I beating is explained by group velocity walk-off between the different modes. Eq. 1.20 gives the group velocity for different modes of a parabolic waveguide, and shows that higher order waveguide modes propagate more slowly than the fundamental. This will eventually result in group velocity walk-off and spatial separation of the different modes. Using Eq. 1.20 and our channel parameters, we see that after 3 cm of propagation, the $(1,0)$ mode has propagated $\sim 5 \ \mu m$ less than the $(0,0)$ mode, with the other higher radial modes having fallen p times further behind. For the $\tau_{FWHM} = 35 \ fs$ pulse used in our simulations, $c\tau_{FWHM} \approx 10 \ \mu m$, and so the separation is significant enough to dramatically reduce the interference effects which

produce mode beating. This is further evidence the beating during phases I and II is a result of different effects.

The phase I beating and walk-off can be clearly seen in Figure 4.6 which presents a more detailed picture of pulse evolution. Panels (a)-(c) show the laser field magnitude a_0 in the $x\xi$ plane; the right column in (a) shows the field profile in the transverse (xy) plane integrated over the pulse envelope. All plots are normalized to the peak value in the upper left panel of (a). The panels are ordered vertically by the z-locations marked in Figure 4.1(a). The large amplitude oscillations of phase I manifest in Figure 4.6(a) as mode shape and size oscillations corresponding to the (0,0) and (1,0) modes. By $z = 25$ mm, as the phase I beating is fading, a small intensity tail has split off, lagging the main pulse. By $z = 50$ mm, the result of group velocity walk-off is seen in the sequence of evenly spaced high order pulselets which has increasingly separated from the main pulse, with the highest order modes the most delayed. Despite the walk-off, the (1,0) structure remains tethered to the (0,0) structure by a long tail, sustaining the beating until $z > \sim 110$ mm, whereupon the stage II oscillations decay

as the wake weakens. This provides key insight into the origin of phase II beating and will be discussed further in the next section.
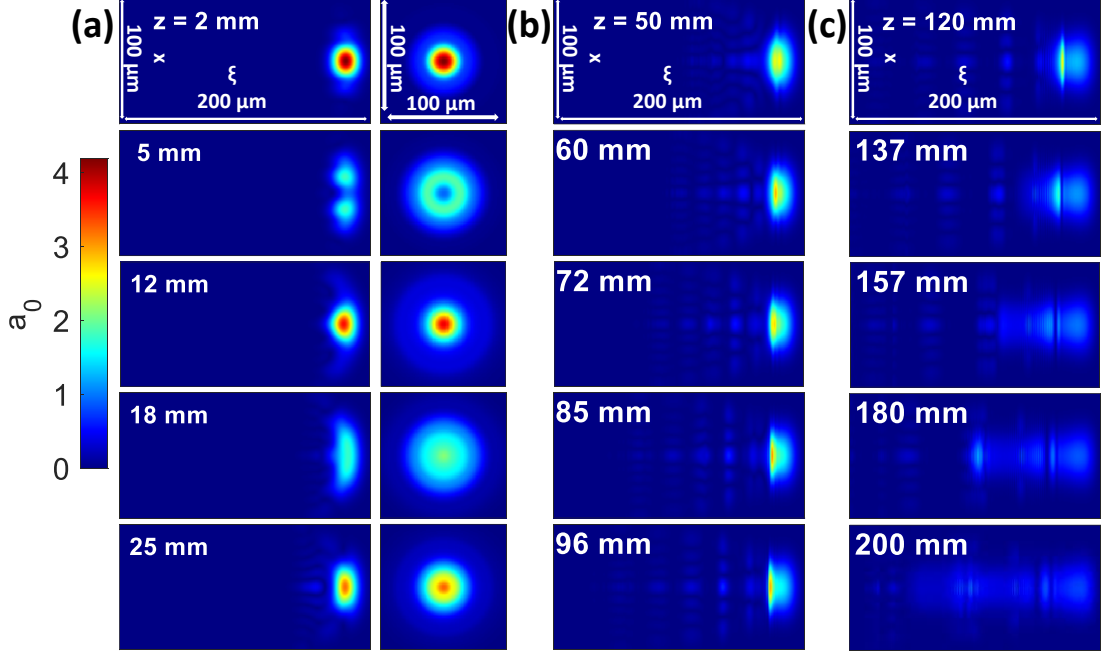
Figure 4.6: Evolution of LWFA drive pulse with $a_{0i} = 2.0, w_0 = 30\ \mu m, \tau_{fwhm} = 35\ fs$ in a prepared index structure with $w_{ch} \approx 20\ \mu m$ and on axis plasma density $N_{e0} = 2.0 \times 10^{17}\ cm^{-3}$. Column (a) for stage I, plots $x\xi$ slices of the field magnitude a_0 on the left and the ξ-integrated mode on the right. The longitudinal positions denoted on the frames are marked by the blue crosses in Fig. 1(a). Column (b), for phase II, plots $x\xi$ slices of a_0 for the longitudinal positions marked by the blue stars. Column (c), for phase III, plots $x\xi$ slices of a_0 for the longitudinal positions marked by the open circles in Fig. 1(a). All slices and profiles are normalized to the maximum at $z = 2\ mm$.

We note that for larger channel sizes (such as $w_{ch} \approx 60\ \mu m$ in [23]), the relative velocities of different modes are much closer together, and separation may not fully occur over the guide length. Suppression of multimode propagation has been identified as a key piece in improving the controllability of LWFA in a plasma waveguide. Proposed solutions rely on the natural leakiness of plasma waveguides to filter out higher modes [91,92]. Mode separation may provide an attractive alternative approach for smaller channels. One potential path to study this effect experimentally is through

spectrally filtering the end mode during imaging. As the higher order modes retreat from front of the bubble, they will experience significantly less redshifting than the fundamental mode which is driving the wake. Application of a simple spectral filter in the imaging system should reveal proportionally more higher order content at the nominal wavelength of the laser, and proportionally more fundamental mode content at longer wavelengths. This measurement is being implemented in current experiments both on the ALEPH laser system at CSU and BELLA Petawatt at Lawrence Berkeley National Laboratory [185].

Another effect of mode separation is that the decoherence of the modes could make direct measurement of multimode guiding difficult: each mode reaches the camera CCD at a different time and so the integrated signal could be dominated by the fundamental mode. This is not apparent in the observed multi-mode propagation in Sec. 3.3. One possible explanation is that much of the energy in the fundamental mode was redshifted beyond the detection limit of the imaging camera. For the camera used in those experiments, the quantum efficiency is nearly zero for wavelengths beyond 1 μm. The spectra in Figure 3.1(f) show redshifting beyond this point for a drive pulse with

just 3 J. We note that in Figure 3.4, multimode guiding is only observed for conditions where redshifting is increased (higher plasma density and higher drive pulse intensity).
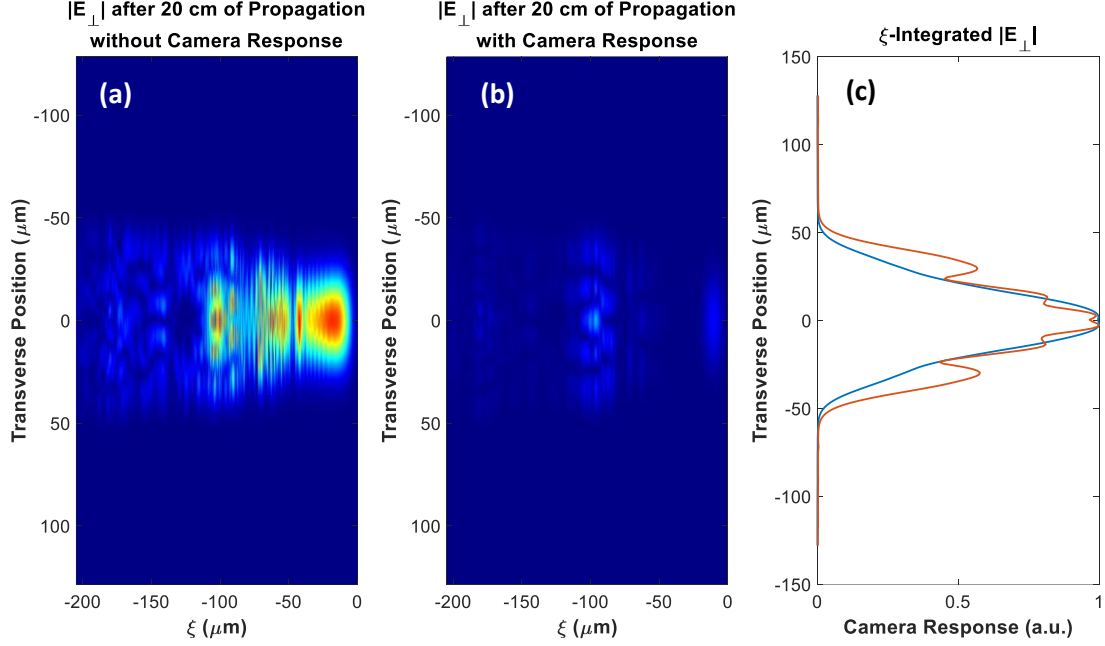
Figure 4.7: Effect of redshift on collected mode measurements. **(a)** slice of $|E|$ after 20 cm propagation for an $a_0 = 1.8$ drive pulse self-waveguiding in a prepared index structure with $N_{e0} = 2.0 \times 10^{17} \ cm^{-3}$. The pulse is initially transversely offset from the structure by $10 \ \mu m$. **(b)** the same slice after spectral filtering corresponding to the endmode imaging camera spectral response. **(c)** integrated signal (as would be measured by the CCD) for the unfiltered pulse (blue line) and filtered pulse (orange line).

This effect is readily observed in PIC simulations as demonstrated in Figure 4.7. Panel (a) shows a slice of the electric field after a drive pulse ($a_0 = 2.0, w_0 = 30 \ \mu m, \tau_{FWHM} = 35 \ fs$) has propagated 20 cm in a prepared index structure with on-axis plasma density $N_{e0} = 2.0 \times 10^{17} \ cm^{-3}$ and $w_{ch} = 20 \ \mu m$. The pulse is offset $10 \ \mu m$ from the structure to increase coupling into higher order modes. The same slice is presented in panel (b), but with spectral filtering corresponding to the imaging CCD spectral response. Panel (c) plots the integrated signal (equivalent to what the CCD would record) for each slice. It can be seen that much of the on-axis laser energy in the

drive pulse has redshifted and so can no longer be recorded by the camera. Though the simulation results are suggestive, it is unfortunately not possible to determine whether this explanation is correct for prior experiments. Future experiments will employ some combination of spectral filtering and IR sensitive cameras in order to better study this inconsistency.

4.2.4 Phase II mode beating induced by ponderomotive channel modification

Separation of higher order modes means that the low amplitude intensity variations during phase II of propagation are due not a continuation of the same beating observed during phase I. We can gain insight into the origin of phase II beating from the additional simulations in Figure 4.1(a) reproduced below. Figure 4.8 (orange curve in Figure 4.1(a)) plots peak a_0 vs propagation distance for a self waveguiding pulse with $a_0 = 0.3$ and $w_0 = 30 \, \mu m$ in a prepared index structure with on-axis density $N_{e0} = 2.0 \times 10^{17} \, cm^{-3}$ and $w_{ch} = 20 \, \mu m$. The intensity is still sufficient to ionize hydrogen beyond $100 \, \mu m$, so the mode structure and attenuation lengths are similar to that for the blue curve in Figure 4.1(a). The drive pulse is not, however, sufficiently intense for nonlinear plasma interaction. The resulting plot of laser intensity evolution in Figure 4.8 demonstrates clear beating between the waveguide modes (phase I), but none of the phase II or III behavior present in simulations of higher intensity drive pulses, and the mode beating decays quickly owing to group velocity walk-off between the modes. This indicates that some form of non-linear interaction plays a role in phase II beating.
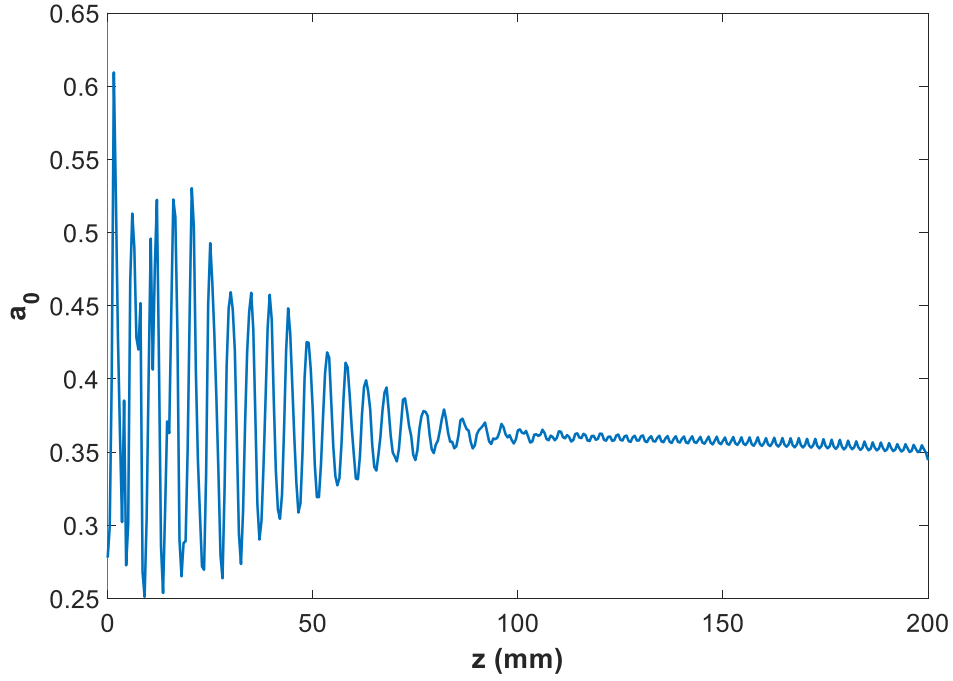
Figure 4.8: Peak laser intensity evolution for a low-intensity drive pulse with intensity $a_0 = 0.3$ and on-axis plasma density $N_{e0} = 2.0 \times 10^{17} \ cm^{-3}$.
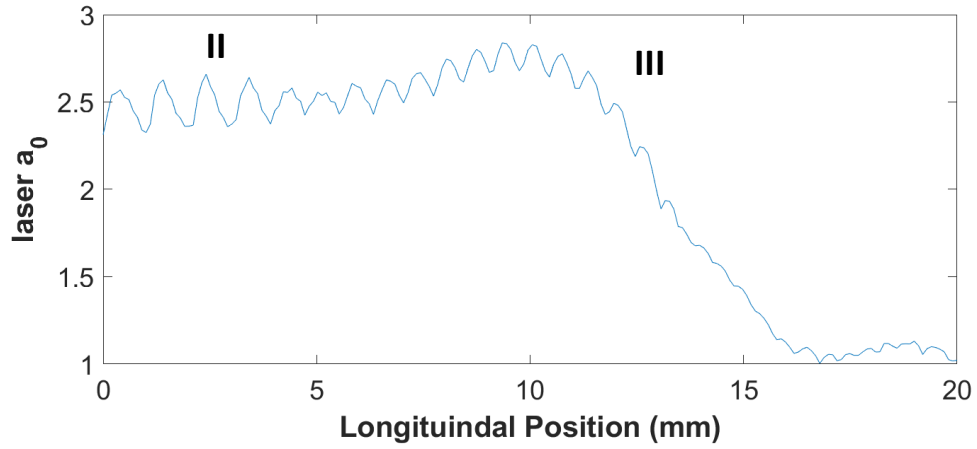
Figure 4.9: Intensity evolution of a matched $w_0 = 30 \ \mu m$ Gaussian drive pulse ($\tau_{FWHM} = 35 \ fs, a_0 = 2.5$) in a parabolic channel with on-axis plasma density $N_{e0} = 4.0 \times 10^{17} \ cm^{-3}$. The numbers identify the propagation phase as defined for mismatched guides. There is no phase I with high amplitude intensity variation due to linear mode beating.

Figure 4.9 plots a_0 against propagation distance for a matched $w_0 = 30 \ \mu m$

Gaussian drive pulse propagating in a parabolic channel with $N_{e0} = 4.0 \times 10^{17} \ cm^{-3}$.

113

There is no phase I beating with high amplitude intensity variation due to coupling into higher order modes. However, there is still the low amplitude intensity variation identified as phase II propagation in Figure 4.1(a). The variations continue as the mean intensity increases until the intensity rapidly drops due to nonlinear collapse of the pulse in phase III.

Further insight can be gained from inspection of the phase II pulse evolution in Figure 4.6, which is partially replotted in Figure 4.10 along with the wake structure for a single cycle of phase II beating. Analysis of the pulse envelope shows that for the leading edge of the pulse (denoted by the dashed line in the top left panel of Figure 4.10), the waist size of the guided beam is $20\ \mu m$ corresponding to $w_{ch} = w_{ch,0}$, the initial waveguide mode size. However, for the pulse maximum (solid line), the waist size is reduced to $w_{ch,p} = 18\ \mu m$. This is true for all of the panels in Figure 4.10 and similar analysis for the simulation in Figure 4.9 shows a mode size of $w_{ch.0} = 30\ \mu m$ in the leading edge and $w_{ch,p} = 24\ \mu m$ at the pulse maximum.
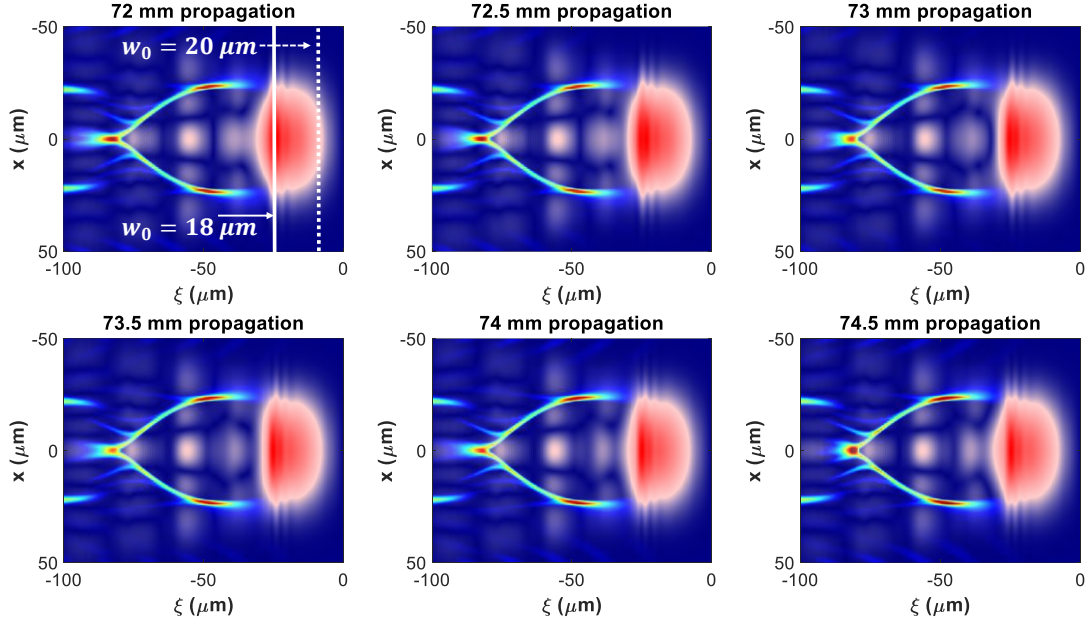
Figure 4.10: Pulse envelope and wake plasma density for a cycle of stage II intensity modulation show in Figure 4.4. The complete separation of the higher order modes is clearly seen, as is a full cycle of beating between the $(1,0)$ and $(0,0)$ components of the pulse, where the $(1,0)$ mode appears in $x - \xi$ cross section as the 3 vertically spaced peaks immediately behind the $(0,0)$ energy centroid. The solid and dashed lines in the top left panel denote the locations of the corresponding waist sizes.

The ξ-dependence of the guided mode size is a result of ponderomotive modification of the channel by the pulse, and the phase II beating can be understood as beating of the $(1,0)$ and $(0,0)$ modes of the pondermotively modified channel [74]. As the pulse propagates through the unperturbed guide, pulse front erosion and red shifting from wake excitation, along with self-steepening at the back of the pulse, act to continuously feed energy from the leading edge of the pulse, where $w_{ch} = w_{ch,0}$, to the cavitated region where the pulse centroid is located and $w_{ch,p} < w_{ch,0}$. This effective mismatch couples to the $(0,0)$ and $(1,0)$ modes of the ponderomotively modified channel, leading to a beat period $\Lambda = 2\pi/|\beta_{10} - \beta_{00}| = \pi^2 \lambda_0 (w_{ch}/\lambda_0)^2$. The amplitude of the beating remains constant because energy is continuously coupled from

the (0,0) mode of the unperturbed channel to the modes of the modified channel. For the specific cases of the blue and gold curves in Figure 4.1(a), $w_{ch} = w_{ch}^{blue}$ (in phase II) gives $\Lambda_{blue} = 4.0$ mm and $w_{ch} = w_{ch}^{gold}$ gives $\Lambda_{gold} = 7.1$ mm. These are in excellent agreement with the oscillation periods observed in the simulations.

Unfortunately, the boosted frame simulation codes we used do not support lab frame reconstruction of the plasma density profile, and so we must infer the channel parameters from the local mode properties. However, the effect of ponderomotive modification on channel structure can be derived from a simple model. In the long pulse limit, the ponderomotive channel modification is expressed as [74]

$$\frac{N_e}{N_{ei}} = 1 + k_p^{-2}\nabla_\perp^2\gamma , \qquad (4.1)$$

where the relativistic factor is $\gamma = (1 + a^2/2)^{1/2}$ for linearly polarized pulses, and $N_e, N_{ei},$ and k_p are functions of r. Here $N_{ei}(r) = N_{e0} + r^2/\pi r_e w_{ch}^4$ [89] is the parabolic plasma density profile of the unperturbed channel, $k_p = c^{-1}(4\pi N_{ei}e^2/m)^{1/2}$ is the plasma wavenumber, and $a = a_{0i}\exp(-(r/w_{ch})^2)$ is the lowest-order mode. The modification is negligible for $r > 2w_{ch}$. Assuming that the ponderomotively perturbed channel is locally parabolic with modified central density N'_{e0} and modified mode radius w'_{ch}, we write

$$N_e(r) = N'_{e0} + \frac{r^2}{\pi r_e w_{ch}^{\prime 4}} \qquad (4.2)$$

Using $N'_{e0} = 0$ (owing to near-cavitation at the pulse energy centroid) and imposing charge conservation ($\int_0^{2w_{ch}} r\,dr\,N_e(r) = \int_0^{2w_{ch}} r\,dr\,N_{ei}(r)$) yields an expression for w'_{ch},

$$\frac{1}{w_{ch}'^4} = \frac{1}{w_{ch}^4} + \frac{\pi r_e N_{e0}}{2\,w_{ch}^2} \quad , \tag{4.3}$$

which can be compared to the local w_{ch} determined from the mode size in our simulations

Table 4.1 shows the efficacy of this model for three cases, two corresponding to the blue and gold curves of Figure 4.1(a) and one corresponding to an $a_0 = 2.5, w_0 = 30\,\mu m, \tau_{FWHM} = 35\,fs$ pulse in a matched parabolic channel with $N_{e0} = 2.0 \times 10^{17}\,cm^{-3}$. In all cases, w_{ch}' determined by the simple model (column E) agrees well with the value extracted from the PIC simulations (column D), giving confidence in our physical picture of mode structure in ponderomotively modified plasma waveguides. The beat period is calculated as $\Lambda = \pi^2 \lambda_0 (w_{ch}'/\lambda_0)^2$, with values plotted in column H of the table. These values compare well to the values (column G) determined by a continuous wavelet transform (CWT) of the associated simulation curves. We note that little energy is coupled into the $(0,1)$ and higher order azimuthal modes of the ponderomotively modified channel since it is necessarily co-axial with the drive pulse; the process resulting in $(0,0) - (1,0)$ mode beating essentially selects for radial modes.

A	B	C	D	E	G	H
w_0, unperturbed w_{ch} (μm)	a_{0i}	N_{e0} $(10^{17}$ $cm^{-3})$	w_{ch}' (μm) sim	w_{ch}' (μm) from Eq. (S4)	Λ (mm) from CWT of curve	Λ (mm) from w_{ch}' (column D)
30, 20 mismatched	2.0	2.0	18	18.5	3.5	4.0
30, 30 matched	2.5	4.0	24	23.6	6.5	7.1
30, 30 matched	2.5	2.0	27	25.9	8.6	8.3

Table 4.1: Comparison of pondermotively modified channel sizes obtain from Eq. 4.3 and analysis of simulated modes.

The sustained beating of $(0,0)$ and $(1,0)$ modes appears to be a universal feature of $a_0 > 1$ laser pulse propagation in a plasma waveguide, whether or not the injected pulse is mode-matched to the guide and to our knowledge, has not been fully identified in previous work. In [48] and [184], phase II-like intensity variations are noted in simulations of a matched mode propagating in a parabolic channel. The suggested cause is ponderomotive modification of the plasma channel. The dependence on phase II beating on drive pulse intensity demonstrated in Figure 4.8 supports this idea. Ref. [186] demonstrates that the intensity and spot size oscillations are correlated with periodic changes in the wake phase velocity. The effects of ponderomotively induced density variations on pulse propagation have been noted for self-guided pulses in [16,83–85,187]. The balance between nonlinear self-focusing and channel modification was predicted to lead to cyclical variation in the propagated beam size. To our knowledge, however, the effect has never been tied to enhancement and suppression of ionization injection and has never been tied to beating between specific waveguide modes.

To further investigate the effect of phase II mode beating on electron injection, we performed a quasi-3D simulation with FBPIC [120] (which enables particle tracking) using the same laser pulse and plasma waveguide profile as in the blue curve in Figure 4.1(a). The simulation was performed in a boosted frame with $\gamma = 5$, with 2 azimuthal modes and 8 particles per cell. The field and tracked particle data are saved every 0.5 mm.

Presented in Figure 4.11 are the on-axis electric field envelope in the light frame over the full propagation distance, and injected charge per unit length in each frame. As in Figure 4.1(a), we identify the three stages of propagation in panel (a): large amplitude oscillation ($z = 0\sim30$ mm, stage I), sustained lower amplitude oscillations, ($z = 30 \sim125$ mm, stage II) and rapid intensity decline ($z > \sim125$ mm, stage III). In stage II, the injected charge is enhanced when the laser peak intensity position retreats in the light frame, which leads to slower wake velocity. Panel (b) shows a zoomed-in part of panel (a) over $z = 30\sim80$ mm. This correlation is clearly seen by the overlap between the peaks of injected charge (white curve) and the periodic deceleration of laser peak position due to mode beating. As a result, the evolution of the electron energy spectra exhibits a striated character. The modulation of laser group velocity due to a mismatched pulse is consistent with observations in [186].
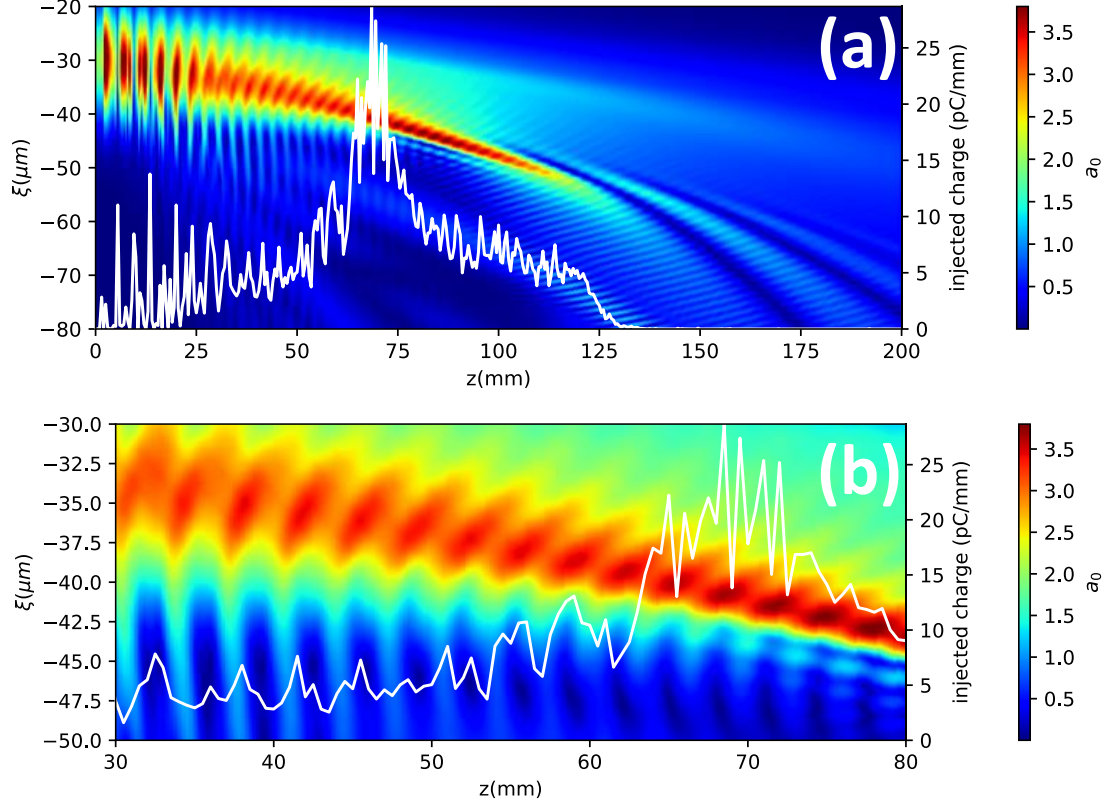
Figure 4.11: Analysis of wake velocity and injection. **(a)** Evolution of the axial laser envelope (a_0) in the light frame, where $\xi = z - v_g t$ is the local space coordinate and v_g is the laser group velocity along z. The white line shows injected charge per unit length over the full propagation. **(b)** Zoomed-in part of panel (a) over $z = 30 \sim 80$ mm showing the correlation between injected charge and the periodic motion of laser pulse peak.

While some injection occurs during phase I, the large amplitude beating induces significant distortion of the wake and loss of trapped electrons. By $z > 80$ mm, ionization injection in phase II ceases owing to pulse self-steepening and etching. By phase III (Fig. 2(c)), the pulse has dispersed and broken up from red shifting and pulse stretching. Here, depletion-induced dephasing [22,44] results in a reduction of maximum accelerated electron energy for $z > 140$ mm, but the striated energy structure is preserved because the pulse is too weak to disrupt the wakefield structure.

For higher laser intensity and plasma density, we observe pulse breakup earlier in propagation, leading to wakefield distortion and loss of the striated energy structure.

4.3 Monoenergetic electron bunches generated by a self-waveguiding LWFA with localized ionization injection

The results in Sec. 4.2 and Figure 3.10 suggest that electron bunches with narrow energy spreads around a single peak energy can be generating by localizing a short ($< $ cm) region of dopant gas within the propagation region where pulse intensity variations result in enhancement and suppression of ionization injection. We present an experimental demonstration of this technique, including the generation of electron bunches with narrow energy spreads ($\Delta E/E \gtrsim 7\%$) up to 2 GeV [74]. These experiments were performed on the ALEPH laser at Colorado State University with the nearly same experimental setup as in [22]. The primary difference was the use of an updated jet design (the internal structure is shown in Figure 2.7) which produced higher Mach number gas flow and enabled insertion of a localized dopant region. We will identify this as 'jet 2', while the jet used for the experiments discussed in Chapter 3 will be identified as 'jet 1'. The longitudinal gas density profiles for jet 1 and jet 2 are shown in Figure 4.12(a-b). Figure 4.12(c) demonstrates the longitudinal density profiles corresponding to use of different localized 95%/5% H_2/N_2 dopant gas within a pure H_2 waveguiding gas. For this case, the dopant was backed with greater or equal pressure to the waveguiding gas. The localized dopant region does have higher variation than the rest of the profile, but it is similar to some of the variations observed in the jet used in [22] and Chapter 3. We also employed a configuration with the dopant gas at a significantly lower backing pressure than the H_2 waveguiding gas. This is

shown in Figure 4.12(d), where the injector region is seen to be quite well localized within the hydrogen. For experiments using jet 2, the transverse interferometer and guided mode diagnostics were not used.

We note that the fluorescence measurement discussed in Sec. 2.4.2 measures fluorescence at the hydrogen α line, and so could not be used to directly measure the distribution of the dopant gas within a larger hydrogen background. Instead, as shown in figure (b), the measurement was performed for two different conditions: (1) with both the injector and main valves firing H_2, (2) with the main valves firing N_2, and the injector valve firing H_2. Comparing these results allows us to infer the location of the doped gas. The dopant valves were backed with variable pressures. In the experiments discussed here, we used a 'high' backing pressure corresponding the same backing pressure (600 psi) for the H_2 valves which led to the highest density accelerator conditions and a 'low' backing pressure of ~30-60 psi.
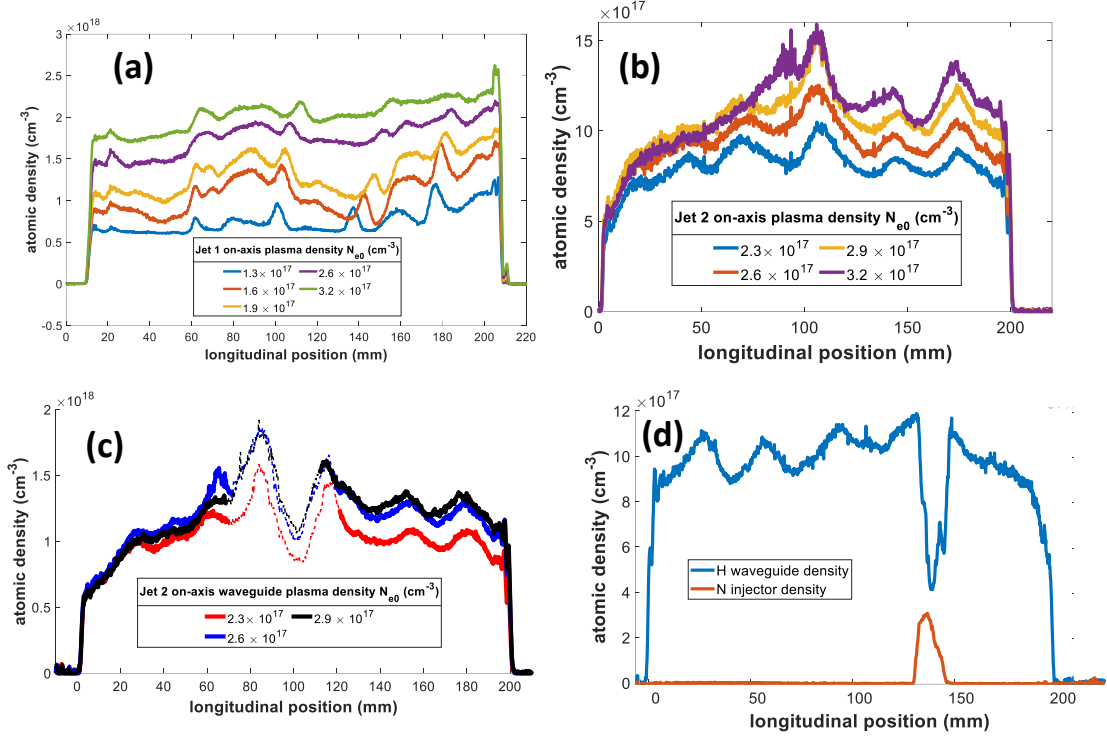
Figure 4.12: Longitudinal density profiles for different jet 2 modes of operation. **(a)** 'jet 1' used in [22]. **(b)** 'jet 2' used in [74] with the same gas used in the entire jet. **(c)** with localized injector gas backed at high pressure. **(d)** with localized dopant gas backed at low pressure.

4.3.1 Experimental observation of stratified electron spectra
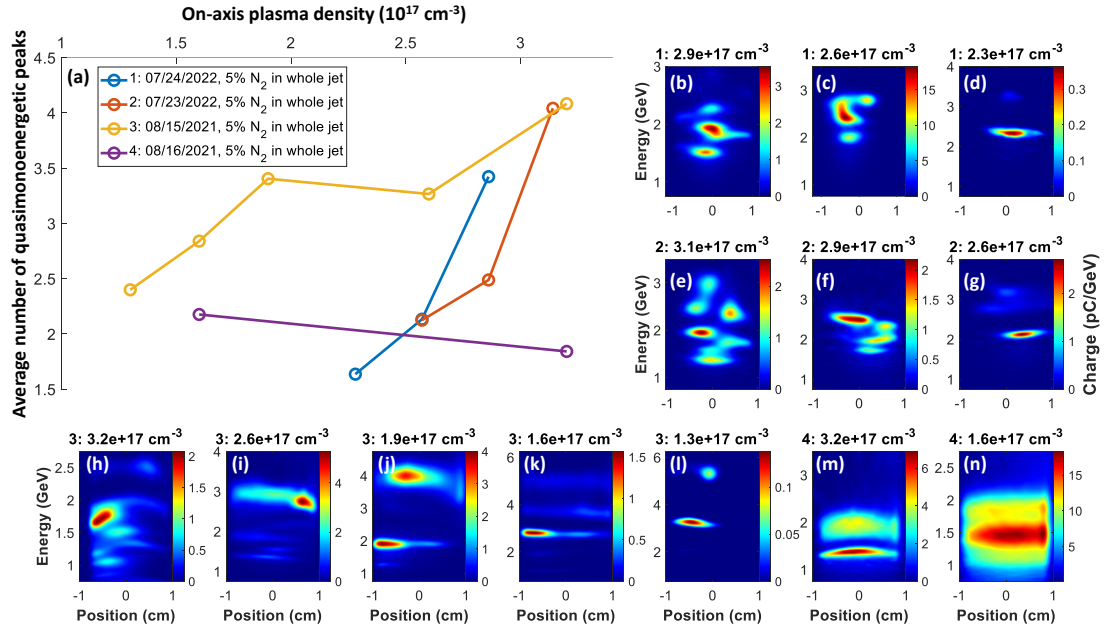
Figure 4.13: Characteristic trends in spectra collected during self-waveguided LWFA experiments. **(a)** the average number of quasi-monoenergetic peaks observed in spectra plotted against on-axis plasma density for different experimental conditions 1-4 identified in Table 2. **(b)-(n)**, representative angle-resolved spectra for each of the conditions shown in (a)

Condition #	P1 energy	P1 pulse length	P2 energy	Jet design	Dopant gas
1	11	55	.5	2	5% N_2, whole jet
2	11	55	.5	2	5% N_2, whole jet
3	11	55	.5	1	5% N_2, whole jet
4	15	45	.5	1	5% N_2, whole jet
5	11	45	.5	2	5% N_2, 10 cm, high pressure
6	11	45	.5	2	5% N_2, 10 cm, low pressure
7	11	45	.5	2	5% N_2, 14 cm, low pressure

					N₂, 14 cm, low pressure
8	11	45	.5	2	

Table 2: experimental conditions for self-waveguided LWFA experiments. Jet design 1 corresponds to that used in the experimental campaign discussed in Chapter 3 and [22]. The longitudinal gas density profile is shown in Figure 4.12(a). Jet design 2 corresponds to the design shown in Figure 2.7 and used in [74], with density profiles for different configurations shown in Figure 4.12(c-d). This design enabled the use of localized dopant regions centered at different longitudinal positions (measured from the front of the jet) as indicated by the 'dopant gas column'.

In our experimental implementation of self-waveguided LWFAs, we have observed that periodic injection due to linear and nonlinear mode beating results in spectra which preserve the characteristic stratified energy distribution predicted by the simulations in Sec. 4.2.1. Figure 4.13(a) plots the average number of quasi-monoenergetic peaks observed vs. on-axis plasma for different experimental configurations identified by the legend and Table 2. Characteristic angle resolved spectra for each configuration and density are identified in Figure 4.13(b-n). For configurations 1-3, there is a clear positive correlation between the on-axis plasma density and the total number of peaks observed. This agrees with our simulation picture, where the amplitude of drive pulse intensity variations during both phases I and II increases with higher plasma density, resulting in more instances of localized injection and a stratified energy structure which was preserved throughout the whole accelerator.

This trend is broken, however, in configuration 4, where the laser intensity was at the maximum for all experiments. In panels (m)-(n), the observed spectral peaks are significantly broader and lower energy than at comparable plasma conditions with a lower drive pulse intensity. This also fits with the picture derived from simulations: the higher initial drive pulse intensity causes an earlier onset of depletion induced

125

dephasing (phase III of pulse propagation), resulting in more significant distortion of the stratified energy structure than with a lower intensity driver.

The highest observed energy gain (~ 5 GeV, panel (l)) occurred with the lowest on-axis density and featured noticeably less accelerated charge (< pC) than other conditions, as shown in Figure 3.7(c). We speculate that these were injected during phase I of the pulse evolution where phase I mode beating dominated the dynamics and much less charge was successfully trapped in the distorted wakes. The higher charge peaks observed at lower energies then correspond to injection during phase II, when the more stable, lower amplitude pulse variations have less effect on the wake structure.

4.3.2 Experiments with localized injector gas region

Along with our simulation studies, these results suggest a path towards the generation of electron bunches with a single quasi-monoenergetic peak: localization of the dopant gas to a short longitudinal region corresponding to the scale length of the intensity variations which trigger ionization injection. Jet 2 presented in Figure 4.12(c-d) features secondary inlets for injector gas which enable exactly this mode of operation and has been successfully deployed to generate quasi-monoenergetic bunches with energy <2 GeV and energy spread >7%.

The results of these experiments are present in Figure 4.14. Panel (a) plots the average number of quasi-monoenergetic measured for configurations 1 and 2 above as well as configurations 5,6, and 7 identified in Table 2, which featured a localized section of 5%/95% N_2/H_2 dopant gas. As expected, use of the localized injector gas region dramatically reduces the number of peaks present in the spectra of accelerated bunches. The angle-resolved spectra in Figure 4.14(b-n) demonstrate that the peak

properties (energy spread, charge, divergence) are qualitatively similar to those observed with dopant in the entire jet (Figure 4.13), indicating that the injection and acceleration process is similar, but that by restricting dopant region, we have limited the number of times electrons are injected due to longitudinal variations in pulse intensity. We note that the spectra collected in Figure 4.13 and Figure 4.14 featured different spectrometer slit widths in order to better characterize the energy spread of these peaks (Sec. 2.5.2. The narrowest (.25 mm) slit used in Figure 4.14(b-d) results in measured energy spreads of >7%. Electron beam propagation simulations [169] suggest that this number is an overestimate, due to dispersion during transmission through the vacuum chamber exit flange.

The injection regions for these configurations were located at 10 and 14 cm from the front of the jet. Based on the simulations presented in Sec. 4.2, this likely means that injection occurred during phase II of pulse evolution and was caused by nonlinear beating of the drive pulse. The comparatively lower energy gain of 1-2 GeV is expected for such late injection. Comparing panels (h-j) with (k-l), shows an expected decrease in the energy gain as the injection location is moved further from the entrance of the guide. We also observe a decrease in the energy gain between configurations 5 and 6, when the injector region stays in the same location, but the backing pressure is dropped. This is perhaps because the effective L_{acc} after the injection region is shorter than the dephasing length, so energy gain is maximized for the higher plasma density.

Figure 4.14(a) demonstrates a significant reduction in the average number of quasi-monoenergetic peaks observed and the angle-resolved spectra show consistent bunch properties for the single peak shots. However, some shots (such as Figure

127

4.14(l)) still demonstrated multiple peaks. We attribute this variation to poor

repeatability of the injector gas profile, which varied in extent from shot to shot.
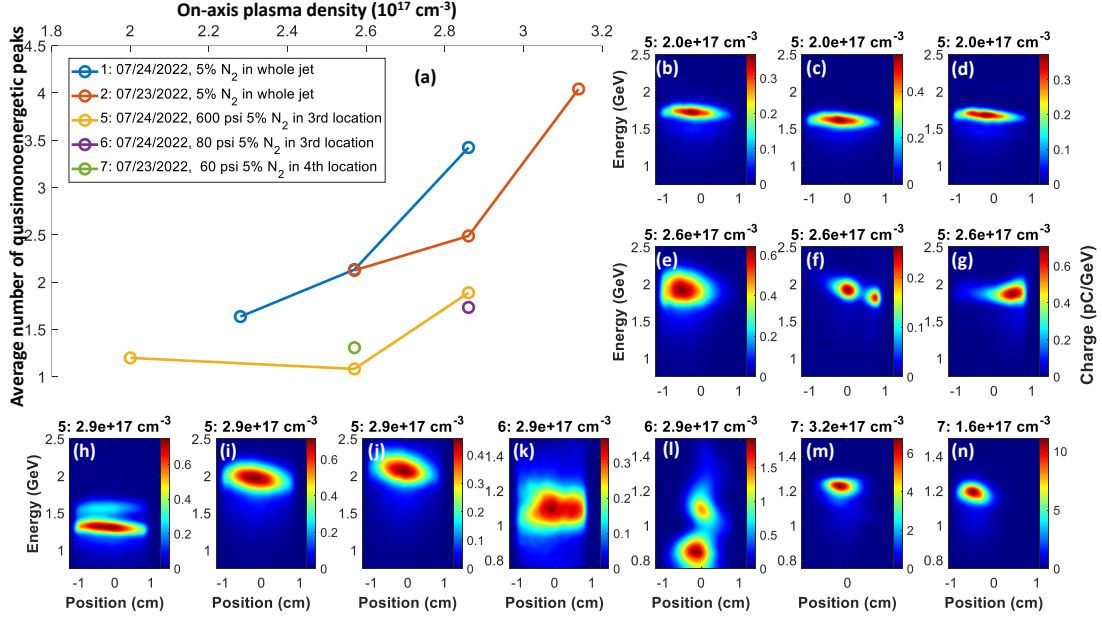
Figure 4.14: Characteristic trends in spectra generated with localized dopant region.**(a)** the average number of quasi-monoenergetic peaks observed in spectra plotted against on-axis plasma density for different experimental configurations 1-2, 5-7 identified in Table 2. **(b)-(n),** representative angle-resolved spectra for each of the conditions shown in (a) for configurations 5-7.

Overall, with improvements in the repeatability of the gas plume and

restriction of the dopant region, this approach will likely be able to consistently

produce monoenergetic multi-GeV electron bunches with <10 % energy spread.

However, the energy spread will ultimately be tied to the spatial scale of the intensity

variations during drive pulse propagation, and must be improved for application

LWFA to FELs or other advanced light sources [13,30]. Better understanding of the

dynamics which govern the injection enhancing variations in pulse intensity is

essential to further improvement and control of the injection process. A focus of

future research will be the identification of the key parameters which cause this

variation, and optimization of the jet and waveguide properties to maximize the amount of injected charge and minimize the spatial period of intensity variations.

4.4 Induced injection through pulse manipulation with plasma channel properties

Another result of interest is shown in Figure 4.15, where the localized dopant was replaced with localized pure N_2 gas. As shown in Figure 4.12, this produces a tightly localized portion of the profile with pure N_2 gas. In [93,106], it was shown that a plasma column field-ionized by a J_0 Bessel beam expanding into neutral gas drove a shock in the neutral atoms moving at the local sound speed: $c_s = (\gamma_s k_B T_g / m_m)^{1/2}$, where $\gamma_s = c_p / c_v$ is the ratio of specific heats, T_b is the local gas temperature (elevated by conduction from the adjacent plasma), and m_m is molecular mass of the working gas. This means that shock expansion is slower in the N_2 region than in the rest of the waveguide, and so the resulting local channel size $w_{ch}(z)$ is smaller. The guided pulse is forced to 'squeeze' into a smaller channel during this region, resulting in energy loss from the mode mismatch, but increasing the pulse intensity above the ionization injection threshold of $a_0 \sim 2.2$ [69,72]. This effect is actually present in all of the mismatched simulations presented in Sec. 4.2, where the mean a_0 in the blue in gold curves of Figure 4.1(a) is noticeably higher than the injected pulse intensity due to squeezing of the $w_0 = 30 \ \mu m$ pulse into waveguides with matched mode sizes $w_{ch} \approx 20 \ \mu m$. This increase in mean intensity is not observed in for matched propagation as presented in Figure 4.9.

The angle-resolved (a) and integrated (b) spectrum in Figure 4.15 show an example of a continuous energy spectrum collected with pure N_2 in the localized injector gas region (configuration 8 in Table 2). The only observations of continuous

spectra across all experimental conditions occurred with the use of a localized N_2 region, suggesting control of the pulse evolution (and thereby injection) can be achieved by manipulation of the channel properties. This is characteristically different than the results in Figure 4.14, which modify the channel properties (i.e. longitudinal restriction of the dopant gas) to accommodate the natural pulse evolution. We speculate that mode control could also be achieved by modifying the ring grating to introduce significant longitudinal dependence to the intensity profile, thus reducing the local heating and concomitant shock expansion speed. This will be a focus of future experiments.
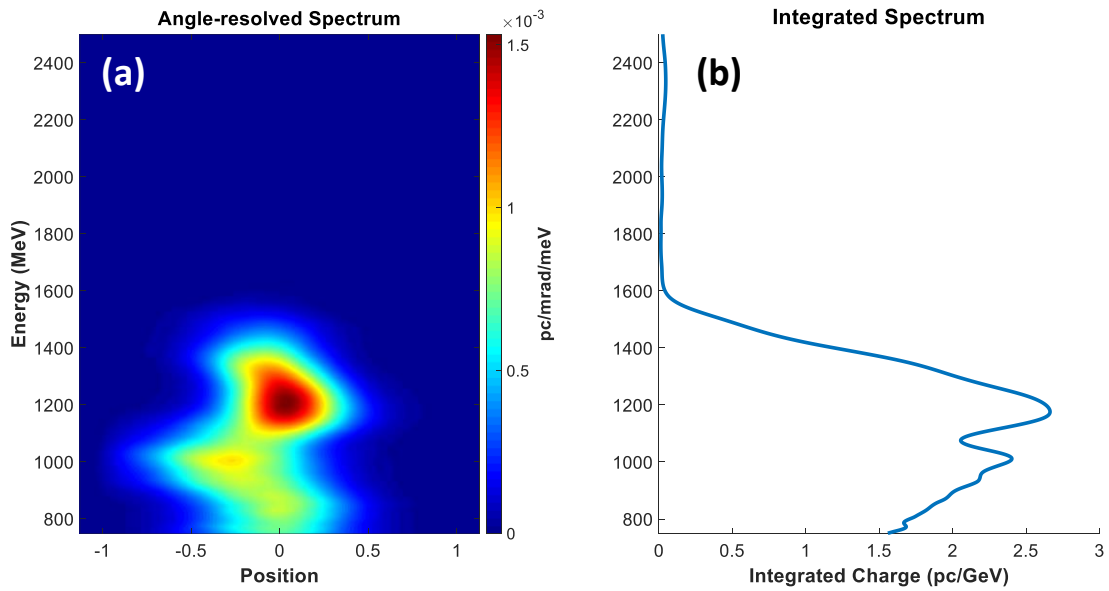
Figure 4.15: Example of a continuous spectrum produced from a localized N_2 region. **(a)** angle-resolved spectrum. **(b)** integrated spectrum.

Chapter 5: Summary and future work

5.1 Summary

Optically generated plasma waveguides will likely be an essential component of next generation laser wakefield accelerators. Waveguides extend the laser-plasma interaction length well beyond the natural diffraction scale of the LWFA drive pulse and thus enable maximal energy gain in the most efficient, quasilinear regime. In this dissertation, we have presented the first demonstrations of multi-GeV electron LWFA in an optically generated plasma waveguide, and identified key pieces of the injection and acceleration processes. In Chapter 1, we reviewed relevant topics including the fundamentals of laser ionization, LWFA, and plasma waveguides.

In Chapter 2, we discussed key experimental components for implementing the self-waveguiding method of plasma waveguide generation in a LWFA. This included discussions of Bessel beam generation using diffractive optical elements, design considerations and characterization of meter-scale supersonic gas jets, and essential diagnostics for the guided pulse, plasma structure, and accelerated electron beams. We also discussed the specific measurement and analysis techniques used for diagnosing electron bunches produced in our experiments.

Chapter 3 presented the first experimental demonstration of multi-GeV LWFA in an optically generated plasma waveguide, which at the time of those experiments was the highest energy gain demonstrated in an all optical LWFA, with some bunches reaching > 5 GeV in few pC quasi-monoenergetic peaks with <15% energy spread and ~mrad divergence over the 20 cm acceleration distance. We presented high power (>100 TW) guiding results, and a series of 43 consecutive shots with synchronized

pulse and electron beam diagnostics which suggested that pointing variation between the drive pulse and channel-forming Bessel beam was the primary cause of shot to shot variation. Accompanying particle-in-cell simulations provided further insight into the guiding and acceleration process. They suggested that electrons were injected via ionization injection of N^{5+} over multiple short ($<$ cm) longitudinal regions, resulting in acceleration of multiple bunches in multiple quasi-monoenergetic peaks. Energy gain was limited by dephasing, which was significantly worsened by depletion of the drive pulse causing a reduction in wake velocity.

These results were further clarified in Chapter 4, where we presented a more detailed picture of pulse evolution in three phases. During phase I, beating between different waveguide modes causes large amplitude variations in drive pulse intensity due to interference and distortion of the transverse electric field. We showed that for our experimental parameters, energy coupled into the higher order modes propagates much more slowly than the fundamental, resulting in spatial separation of the modes and suppression of mode beating. As mode beating is suppressed, the pulse enters phase II where ponderomotive modification of the channel causes interference between different temporal slices of the pulse which results in steady, low amplitude variation of the drive pulse intensity. During these two phases, the intensity variations are shown to be correlated with enhancement and suppression of ionization injection, resulting in a stratified energy structure in the accelerating bunch. This stratification can be either preserved or distorted during phase III, when accumulated nonlinear effects cause the drive pulse to collapse and the electron bunch begins to dephase. We further demonstrated that restricting the longitudinal extent of the dopant gas to the same

spatial scale as the phase I and II intensity variations, results in a drastic decrease in the number of quasi-monoenergetic peaks, and can produce electron bunches with single quasi-monoenergetic peaks < 2GeV with >6% energy spread and ~mrad divergence. We also presented evidence that the mode properties can be modified by use of a structured plasma channel in order to induce ionization injection.

5.2 Future work

We have outlined several paths towards improved control of multi-GeV LWFA in optically generated plasma waveguides. Mode manipulation as discussed in Sec. 4.4 is one such path, as are the localized dopant regions in Sec. 4.3. Better control of injection is key not only for LWFA repeatability, but also for improving energy gain. As discussed in Sec. 3.5, the highest energy gain electron bunches produced were likely dephasing-limited over the 20 cm jet. This means that higher energy gain could likely have been achieved with the same driver if we had been able to operate with a longer jet at a lower density. Better understanding of the injection process and control of the dynamics is essential for operating at these lower densities. As discussed in Chapter 1, dephasing can also be mitigated with tailored plasma density profiles, which results in increasing wake phase velocity and prevents the accelerating bunch from leaving the back of the bucket. One possible explanation for the different energy gain for the same nominal conditions between the jets used in Chapters 3 and 4 is that a slight upramp during the last third of the first jet enabled higher energy gain. One possible path towards longitudinal control of the density profile is through manipulation of the throat

133

the width. In general, longitudinal control of gas jet profiles will be essential for producing the most efficient and repeatable LWFAs.

We also identified several key areas where waveguide implementation and diagnosis could be improved. Better diagnosis of guided mode properties, particularly spectral filtering will be key to better understanding intense pulse evolution. It is possible that the transition observed from apparent monomode to multimode guiding in our experiments was due to redshifting of the fundamental mode resulting in a significantly weaker camera pixel response. Of high priority is better understanding of the relationship between OFI plasma heating and channel expansion, particularly the effect of longitudinal variations in Bessel beam intensity on the longitudinal uniformity of the prepared index structure. One approach to improving Bessel beam uniformity is the implementation of a logarithmic axicon which modifies the linear radial phase profile of a Bessel beam to slightly change the approach angle for each near field annulus, resulting in a more consistent peak central spot intensity across the focal line [188]. Finally, we also presented another axicon design, the binary Bessel beam, which will be essential for implementation of the two-Bessel waveguide generation method.

References

[1] W.A. Hendrickson, Trends Biochem. Sci. **25**, 637 (2000).

[2] S. Benedetti, A. Grudiev, and A. Latina, Phys. Rev. Accel. Beams **20**, 040101 (2017).

[3] R. Van Noorden, Nature **504**, 202 (2013).

[4] P. Suortti and W. Thomlinson, Phys. Med. Biol. **48**, R1 (2003).

[5] M.K. Gaillard, P.D. Grannis, and F.J. Sciulli, Rev. Mod. Phys. **71**, S96 (1999).

[6] V. Shiltsev and F. Zimmermann, Rev. Mod. Phys. **93**, 15006 (2021).

[7] C. Bostedt, S. Boutet, D.M. Fritz, Z. Huang, H.J. Lee, H.T. Lemke, A. Robert, W.F. Schlotter, J.J. Turner, and G.J. Williams, Rev. Mod. Phys. **88**, 015007 (2016).

[8] T. Tajima and J.M. Dawson, Phys. Rev. Lett. **43**, 267 (1979).

[9] C.B. Schroeder, E. Esarey, C.G.R. Geddes, C. Benedetti, and W.P. Leemans, Phys. Rev. Spec. Top. - Accel. Beams **13**, 101301 (2010).

[10] M.P. Anania, E. Brunetti, S.M. Wiggins, D.W. Grant, G.H. Welsh, R.C. Issac, S. Cipiccia, R.P. Shanks, G.G. Manahan, C. Aniculaesei, S.B. Van Der Geer, M.J. De Loos, M.W. Poole, B.J.A. Shepherd, J.A. Clarke, W.A. Gillespie, A.M. Macleod, and D.A. Jaroszynski, Appl. Phys. Lett. **104**, 264102 (2014).

[11] K. Ta Phuoc, S. Corde, C. Thaury, V. Malka, A. Tafzi, J.P. Goddet, R.C. Shah, S. Sebban, and A. Rousse, Nat. Photonics **6**, 308 (2012).

[12] K. Nakajima, Nat. Phys. **4**, 92 (2008).

[13] F. Albert and A.G.R. Thomas, Plasma Phys. Control. Fusion **58**, 103001 (2016).

[14] K.K. Kainz, K.R. Hogstrom, J.A. Antolak, P.R. Almond, C.D. Bloch, C. Chiu, M. Fomytskyi, F. Raischel, M. Downer, and T. Tajima, Med. Phys. **31**, 2053 (2004).

[15] C. Joshi, S. Corde, and W.B. Mori, Phys. Plasmas **27**, 070602 (2020).

[16] E. Esarey, C.B. Schroeder, and W.P. Leemans, Rev. Mod. Phys. **81**, 1229 (2009).

[17] E. Esarey, P. Sprangle, J. Krall, and A. Ting, IEEE Trans. Plasma Sci. **24**, 252 (1996).

[18] T. Katsouleas, Phys. Rev. A **33**, 2056 (1986).

[19] M.J. Hogan, C.D. Barnes, C.E. Clayton, F.J. Decker, S. Deng, P. Emma, C. Huang, R.H. Iverson, D.K. Johnson, C. Joshi, T. Katsouleas, P. Krejcik, W. Lu, K.A. Marsh, W.B. Mori, P. Muggli, C.L. O'Connell, E. Oz, R.H. Siemann, and D. Walz, Phys. Rev. Lett. **95**, 054802 (2005).

[20] I. Blumenfeld, C.E. Clayton, F.J. Decker, M.J. Hogan, C. Huang, R. Ischebeck, R. Iverson, C. Joshi, T. Katsouleas, N. Kirby, W. Lu, K.A. Marsh, W.B. Mori, P. Muggli, E. Oz, R.H. Siemann, D. Walz, and M. Zhou, Nature **445**, 741 (2007).

[21] E. Adli, A. Ahuja, O. Apsimon, R. Apsimon, A.M. Bachmann, D. Barrientos, F. Batsch, J. Bauche, V.K. Berglyd Olsen, M. Bernardini, T. Bohl, C. Bracco, F. Braunmüller, G. Burt, B. Buttenschön, A. Caldwell, M. Cascella, J. Chappell, E. Chevallay, M. Chung, D. Cooke, H. Damerau, L. Deacon, L.H. Deubner, A. Dexter, S. Doebert, J. Farmer, V.N. Fedosseev, R. Fiorito, R.A. Fonseca, F. Friebel, L. Garolfi, S. Gessner, I. Gorgisyan, A.A. Gorn, E. Granados, O. Grulke, E. Gschwendtner, J. Hansen, A. Helm, J.R. Henderson, M. Hüther, M. Ibison, L. Jensen, S. Jolly, F. Keeble, S.Y. Kim, F. Kraus, Y. Li, S. Liu, N. Lopes, K. V. Lotov, L. Maricalva Brun, M. Martyanov, S. Mazzoni, D. Medina Godoy, V.A. Minakov, J. Mitchell, J.C. Molendijk, J.T. Moody, M. Moreira, P. Muggli, E. Öz, C. Pasquino, A. Pardons, F. Peña Asmus, K. Pepitone, A. Perera, A. Petrenko, S. Pitman, A. Pukhov,

136

S. Rey, K. Rieger, H. Ruhl, J.S. Schmidt, I.A. Shalimova, P. Sherwood, L.O. Silva, L. Soby, A.P. Sosedkin, R. Speroni, R.I. Spitsyn, P. V. Tuev, M. Turner, F. Velotti, L. Verra, V.A. Verzilov, J. Vieira, C.P. Welsch, B. Williamson, M. Wing, B. Woolley, and G. Xia, Nature **561**, 363 (2018).

[22] B. Miao, J.E. Shrock, L. Feder, R.C. Hollinger, J. Morrison, R. Nedbailo, A. Picksley, H. Song, S. Wang, J.J. Rocca, and H.M. Milchberg, Phys. Rev. X **12**, 31038 (2022).

[23] A.J. Gonsalves, K. Nakamura, J. Daniels, C. Benedetti, C. Pieronek, T.C.H. De Raadt, S. Steinke, J.H. Bin, S.S. Bulanov, J. Van Tilborg, C.G.R. Geddes, C.B. Schroeder, C. Tóth, E. Esarey, K. Swanson, L. Fan-Chiang, G. Bagdasarov, N. Bobrova, V. Gasilov, G. Korn, P. Sasorov, and W.P. Leemans, Phys. Rev. Lett. **122**, 84801 (2019).

[24] X. Wang, R. Zgadzaj, N. Fazel, Z. Li, S.A. Yi, X. Zhang, W. Henderson, Y.Y. Chang, R. Korzekwa, H.E. Tsai, C.H. Pai, H. Quevedo, G. Dyer, E. Gaul, M. Martinez, A.C. Bernstein, T. Borger, M. Spinks, M. Donovan, V. Khudik, G. Shvets, T. Ditmire, and M.C. Downer, Nat. Commun. **4**, 1988 (2013).

[25] K. Oubrerie, A. Leblanc, O. Kononenko, R. Lahaye, I.A. Andriyash, J. Gautier, J.-P. Goddet, L. Martelli, A. Tafzi, K.T. Phuoc, S. Smartsev, and C. Thaury, Light Sci. Appl. **11**, 180 (2022).

[26] S. Steinke, J. Van Tilborg, C. Benedetti, C.G.R. Geddes, C.B. Schroeder, J. Daniels, K.K. Swanson, A.J. Gonsalves, K. Nakamura, N.H. Matlis, B.H. Shaw, E. Esarey, and W.P. Leemans, Nature **530**, 190 (2016).

[27] A.E. Hussein, N. Senabulya, Y. Ma, M.J.V. Streeter, B. Kettle, S.J.D. Dann, F.

Albert, N. Bourgeois, S. Cipiccia, J.M. Cole, O. Finlay, E. Gerstmayr, I.G. González, A. Higginbotham, D.A. Jaroszynski, K. Falk, K. Krushelnick, N. Lemos, N.C. Lopes, C. Lumsdon, O. Lundh, S.P.D. Mangles, Z. Najmudin, P.P. Rajeev, C.M. Schlepütz, M. Shahzad, M. Smid, R. Spesyvtsev, D.R. Symes, G. Vieux, L. Willingale, J.C. Wood, A.J. Shahani, and A.G.R. Thomas, Sci. Rep. **9**, 1 (2019).

[28] H.P. Schlenvoigt, K. Haupt, A. Debus, F. Budde, O. Jäckel, S. Pfotenhauer, H. Schwoerer, E. Rohwer, J.G. Gallacher, E. Brunetti, R.P. Shanks, S.M. Wiggins, and D.A. Jaroszynski, Nat. Phys. **4**, 130 (2008).

[29] A.R. Maier, A. Meseck, S. Reiche, C.B. Schroeder, T. Seggebrock, and F. Grüner, Phys. Rev. X **2**, 031019 (2012).

[30] C. Pellegrini, A. Marinelli, and S. Reiche, Rev. Mod. Phys. **88**, 015006 (2016).

[31] M. Labat, J.C. Cabadağ, A. Ghaith, A. Irman, A. Berlioux, P. Berteaud, F. Blache, S. Bock, F. Bouvet, F. Briquez, Y.Y. Chang, S. Corde, A. Debus, C. De Oliveira, J.P. Duval, Y. Dietrich, M. El Ajjouri, C. Eisenmann, J. Gautier, R. Gebhardt, S. Grams, U. Helbig, C. Herbeaux, N. Hubert, C. Kitegi, O. Kononenko, M. Kuntzsch, M. LaBerge, S. Lê, B. Leluan, A. Loulergue, V. Malka, F. Marteau, M.H.N. Guyen, D. Oumbarek-Espinos, R. Pausch, D. Pereira, T. Püschel, J.P. Ricaud, P. Rommeluere, E. Roussel, P. Rousseau, S. Schöbel, M. Sebdaoui, K. Steiniger, K. Tavakoli, C. Thaury, P. Ufer, M. Valléau, M. Vandenberghe, J. Vétéran, U. Schramm, and M.E. Couprie, Nat. Photonics **17**, 150 (2023).

[32] F. Albert, A.G.R. Thomas, S.P.D. Mangles, S. Banerjee, S. Corde, A. Flacco, M. Litos, D. Neely, J. Vieira, Z. Najmudin, R. Bingham, C. Joshi, and T. Katsouleas, Plasma Phys. Control. Fusion **56**, (2014).

[33] D. Strickland and G. Mourou, Opt. Commun. **56**, 219 (1985).

[34] L. V. Keldysh, J.E.T.P. (USSR) **47**, 1945 (1964).

[35] P.B. Corkum, N.H. Burnett, and F. Brunel, Phys. Rev. Lett. **62**, 1259 (1989).

[36] N.B. Delone and V.P. Krainov, Uspekhi Fiz. Nauk **168**, 548 (1998).

[37] S. Augst, D. Strickland, D.D. Meyerhofer, S.L. Chin, and J.H. Eberly, Phys. Rev. Lett. **63**, 2212 (1989).

[38] R.M. Schwartz, D. Woodbury, J. Isaacs, P. Sprangle, and H.M. Milchberg, Sci. Adv. **5**, 6804 (2019).

[39] E. Yablonovitch, Appl. Phys. Lett. **23**, 121 (1973).

[40] W. Lu, M. Tzoufras, C. Joshi, F.S. Tsung, W.B. Mori, J. Vieira, R.A. Fonseca, and L.O. Silva, Phys. Rev. Spec. Top. - Accel. Beams **10**, 061301 (2007).

[41] C. Joshi, IEEE Trans. Plasma Sci. **45**, 3134 (2017).

[42] J.E. Ralph, K.A. Marsh, A.E. Pak, W. Lu, C.E. Clayton, F. Fang, W.B. Mori, and C. Joshi, Phys. Rev. Lett. **102**, 175003 (2009).

[43] A. Golovanov, I.Y. Kostyukov, A. Pukhov, and V. Malka, Phys. Rev. Lett. **130**, 105001 (2023).

[44] B.A. Shadwick, C.B. Schroeder, and E. Esarey, Phys. Plasmas **16**, 056704 (2009).

[45] C.B. Schroeder, C. Benedetti, E. Esarey, and W.P. Leemans, Phys. Rev. Lett. **106**, 135002 (2011).

[46] S. Shiraishi, C. Benedetti, A.J. Gonsalves, K. Nakamura, B.H. Shaw, T. Sokollik, J. Van Tilborg, C.G.R. Geddes, C.B. Schroeder, C. Tóth, E. Esarey, and W.P. Leemans, Phys. Plasmas **20**, 063103 (2013).

[47] C.D. Decker, W.B. Mori, K.C. Tzeng, and T. Katsouleas, Phys. Plasmas **3**, 2047 (1996).

[48] P. Sprangle, E. Esarey, J. Krall, and G. Joyce, Phys. Rev. Lett. **69**, 2200 (1992).

[49] J. Wu and T.M. Antonsen, Phys. Plasmas **10**, 2254 (2003).

[50] E. Esarey, P. Sprangle, J. Krall, and A. Ting, IEEE J. Quantum Electron. **33**, 1879 (1997).

[51] C.A. Lindstrøm, Phys. Rev. Accel. Beams **24**, 14801 (2021).

[52] A.I. Akhiezer and R. V. Polovin, J.E.T.P. (USSR) **30**, 915 (1956).

[53] J.M. Dawson, Phys. Rev. **113**, 383 (1959).

[54] C.B. Schroeder, E. Esarey, B.A. Shadwick, and W.P. Leemans, Phys. Plasmas **13**, 033103 (2006).

[55] C.B. Schroeder, E. Esarey, and B.A. Shadwick, Phys. Rev. E - Stat. Nonlinear, Soft Matter Phys. **72**, 055401 (2005).

[56] E. Esarey, C.B. Schroeder, E. Cormier-Michel, B.A. Shadwick, C.G.R. Geddes, and W.P. Leemans, Phys. Plasmas **14**, 056707 (2007).

[57] S. Bulanov, N. Naumova, F. Pegoraro, and J. Sakai, Phys. Rev. E - Stat. Physics, Plasmas, Fluids, Relat. Interdiscip. Top. **58**, R5257 (1998).

[58] C.G.R. Geddes, K. Nakamura, G.R. Plateau, C. Toth, E. Cormier-Michel, E. Esarey, C.B. Schroeder, J.R. Cary, and W.P. Leemans, Phys. Rev. Lett. **100**, 215004 (2008).

[59] C.S. Hue, Y. Wan, E.Y. Levine, and V. Malka, Matter Radiat. Extrem. **8**, (2023).

[60] H. Suk, N. Barov, J.B. Rosenzweig, and E. Esarey, Phys. Rev. Lett. **86**, 1011 (2001).

[61] K. Schmid, A. Buck, C.M.S. Sears, J.M. Mikhailova, R. Tautz, D. Herrmann, M. Geissler, F. Krausz, and L. Veisz, Phys. Rev. Spec. Top. - Accel. Beams **13**, 091301 (2010).

[62] P. Sprangle, B. Hafizi, J.R. Peñano, R.F. Hubbard, A. Ting, C.I. Moore, D.F. Gordon, A. Zigler, D. Kaganovich, and T.M. Antonsen, Phys. Rev. E **63**, 564051 (2001).

[63] A. Döpp, E. Guillaume, C. Thaury, A. Lifschitz, K. Ta Phuoc, and V. Malka, Phys. Plasmas **23**, 056702 (2016).

[64] E. Guillaume, A. Döpp, C. Thaury, K. Ta Phuoc, A. Lifschitz, G. Grittani, J.P. Goddet, A. Tafzi, S.W. Chou, L. Veisz, and V. Malka, Phys. Rev. Lett. **115**, 155002 (2015).

[65] J. Faure, C. Rechatin, A. Norlin, A. Lifschitz, Y. Glinec, and V. Malka, Nature **444**, 737 (2006).

[66] G. Fubiani, E. Esarey, C.B. Schroeder, and W.P. Leemans, Phys. Rev. E - Stat. Physics, Plasmas, Fluids, Relat. Interdiscip. Top. **70**, 12 (2004).

[67] E. Esarey, R.F. Hubbard, W.P. Leemans, A. Ting, and P. Sprangle, Phys. Rev. Lett. **79**, 2682 (1997).

[68] V. Malka, J. Faure, C. Rechatin, A. Ben-Ismail, J.K. Lim, X. Davoine, and E. Lefebvre, Phys. Plasmas **16**, 056703 (2009).

[69] A. Pak, K.A. Marsh, S.F. Martins, W. Lu, W.B. Mori, and C. Joshi, Phys. Rev. Lett. **104**, 025003 (2010).

[70] C. McGuffey, A.G.R. Thomas, W. Schumaker, T. Matsuoka, V. Chvykov, F.J. Dollar, G. Kalintchenko, V. Yanovsky, A. Maksimchuk, K. Krushelnick, V.Y.

Bychenkov, I. V. Glazyrin, and A. V. Karpeev, Phys. Rev. Lett. **104**, 025004 (2010).

[71] C.E. Clayton, J.E. Ralph, F. Albert, R.A. Fonseca, S.H. Glenzer, C. Joshi, W. Lu, K.A. Marsh, S.F. Martins, W.B. Mori, A. Pak, F.S. Tsung, B.B. Pollock, J.S. Ross, L.O. Silva, and D.H. Froula, Phys. Rev. Lett. **105**, 105003 (2010).

[72] M. Chen, E. Esarey, C.B. Schroeder, C.G.R. Geddes, and W.P. Leemans, Phys. Plasmas **19**, 033101 (2012).

[73] C. Thaury, E. Guillaume, A. Lifschitz, K. Ta Phuoc, M. Hansson, G. Grittani, J. Gautier, J.P. Goddet, A. Tafzi, O. Lundh, and V. Malka, Sci. Rep. **5**, 16310 (2015).

[74] J.E. Shrock, B. Miao, E. Rockafellow, A. Picksley, R. Hollinger, S. Wang, J.J. Rocca, and H.M. Milchberg, *Guided Mode Evolution and Localized Ionization Injection in Meter-Scale, Multi-GeV Laser Wakefield Accelerators* (n.d.).

[75] C.G. Durfee, J. Lynch, and H.M. Milchberg, Phys. Rev. E **51**, 2368 (1995).

[76] F. Mitschke, *Fiber Optics: Physics and Technology* (Springer, London, 2008).

[77] S. Atakaramians, S. Afshar V., T.M. Monro, and D. Abbott, Adv. Opt. Photonics **5**, 169 (2013).

[78] M. Soljačić and J.D. Joannopoulos, Nat. Mater. **3**, 211 (2004).

[79] P. Sprangle, E. Esarey, A. Ting, and G. Joyce, Appl. Phys. Lett. **53**, 2146 (1988).

[80] P. Sprangle, E. Esarey, and J. Krall, Phys. Rev. E - Stat. Physics, Plasmas, Fluids, Relat. Interdiscip. Top. **54**, 4211 (1996).

[81] H.T. Kim, K.H. Pae, H.J. Cha, I.J. Kim, T.J. Yu, J.H. Sung, S.K. Lee, T.M. Jeong, and J. Lee, Phys. Rev. Lett. **111**, 165002 (2013).

[82] P. Sprangle, E. Esarey, and A. Ting, Phys. Rev. Lett. **64**, 2011 (1990).

[83] T.M. Antonsen and P. Mora, Phys. Rev. Lett. **69**, 2204 (1992).

[84] B. Hafizi, A. Ting, P. Sprangle, and R.F. Hubbard, Phys. Rev. E - Stat. Physics, Plasmas, Fluids, Relat. Interdiscip. Top. **62**, 4120 (2000).

[85] G.-Z. Sun, E. Ott, Y.C. Lee, and P. Guzdar, Phys. Fluids **30**, 526 (1987).

[86] A.J. Goers, G.A. Hine, L. Feder, B. Miao, F. Salehi, J.K. Wahlstrand, and H.M. Milchberg, Phys. Rev. Lett. **115**, 194802 (2015).

[87] D. Guénot, D. Gustas, A. Vernier, B. Beaurepaire, F. Böhle, M. Bocoum, M. Lozano, A. Jullien, R. Lopez-Martens, A. Lifschitz, and J. Faure, Nat. Photonics **11**, 293 (2017).

[88] F. Salehi, M. Le, L. Railing, M. Kolesik, and H.M. Milchberg, Phys. Rev. X **11**, 021055 (2021).

[89] T.R. Clark and H.M. Milchberg, Phys. Rev. E **61**, 1954 (2000).

[90] T.R. Clark, Hydrodynamical and Optical Properties of the Plasma Waveguide, University of Maryland, 1998.

[91] T.M. Antonsen and P. Mora, Phys. Rev. Lett. **74**, 4440 (1995).

[92] B.Z. Djordjević, C. Benedetti, C.B. Schroeder, E. Esarey, and W.P. Leemans, Phys. Plasmas **25**, 013103 (2018).

[93] L. Feder, B. Miao, J.E. Shrock, A. Goffin, and H.M. Milchberg, Phys. Rev. Res. **2**, 43173 (2020).

[94] C.G. Durfee, F. Lynch, and H.M. Milchberg, Opt. Lett. **20**, 946 (1995).

[95] G. Bonnaud, H.S. Brandi, C. Manus, G. Mainfray, and T. Lehner, Phys. Plasmas **1**, 968 (1994).

[96] E. Esarey, J. Krall, and P. Sprangle, Phys. Rev. Lett. **72**, 2887 (1994).

[97] C. Benedetti, C.B. Schroeder, E. Esarey, and W.P. Leemans, Phys. Plasmas **19**,

053101 (2012).

[98] J.E. Shrock, B. Miao, E. Rockafellow, and H.M. Milchberg, *Generation and Diagnosis of Plasma Waveguides* (2023).

[99] C.G. Durfee and H.M. Milchberg, Phys. Rev. Lett. **71**, 2409 (1993).

[100] T.R. Clark and H.M. Milchberg, Phys. Rev. Lett. **78**, 2373 (1997).

[101] A.W. Snyder and J.D. Love, *Optical Waveguide Theory* (Chapman and Hall, London, 1984).

[102] P. Volfbeyn, E. Esarey, and W.P. Leemans, Phys. Plasmas **6**, 2269 (1999).

[103] H.M. Milchberg, S.J. McNaught, and E. Parra, Phys. Rev. E - Stat. Physics, Plasmas, Fluids, Relat. Interdiscip. Top. **64**, 7 (2001).

[104] H. Sheng, K.Y. Kim, V. Kumarappan, B.D. Layer, and H.M. Milchberg, Phys. Rev. E - Stat. Nonlinear, Soft Matter Phys. **72**, 036411 (2005).

[105] V. Kumarappan, K.Y. Kim, and H.M. Milchberg, Phys. Rev. Lett. **94**, 205004 (2005).

[106] B. Miao, L. Feder, J.E. Shrock, A. Goffin, and H.M. Milchberg, Phys. Rev. Lett. **125**, 74801 (2020).

[107] A. Picksley, A. Alejo, J. Cowley, N. Bourgeois, L. Corner, L. Feder, J. Holloway, H. Jones, J. Jonnerby, H.M. Milchberg, L.R. Reid, A.J. Ross, R. Walczak, and S.M. Hooker, Phys. Rev. Accel. Beams **23**, 81303 (2020).

[108] N. Lemos, L. Cardoso, J. Geada, G. Figueira, F. Albert, and J.M. Dias, Sci. Rep. **8**, 3165 (2018).

[109] N. Lemos, T. Grismayer, L. Cardoso, G. Figueira, R. Issac, D.A. Jaroszynski, and J.M. Dias, Phys. Plasmas **20**, 063102 (2013).

[110] R.J. Shalloo, C. Arran, L. Corner, J. Holloway, J. Jonnerby, R. Walczak, H.M. Milchberg, and S.M. Hooker, Phys. Rev. E **97**, 053203 (2018).

[111] S. Smartsev, C. Caizergues, K. Oubrerie, J. Gautier, J.-P. Goddet, A. Tafzi, K.T. Phuoc, V. Malka, and C. Thaury, Opt. Lett. **44**, 3414 (2019).

[112] R.J. Shalloo, C. Arran, A. Picksley, A. Von Boetticher, L. Corner, J. Holloway, G. Hine, J. Jonnerby, H.M. Milchberg, C. Thornton, R. Walczak, and S.M. Hooker, Phys. Rev. Accel. Beams **22**, 41302 (2019).

[113] A. Butler, D.J. Spence, and S.M. Hooker, Phys. Rev. Lett. **89**, 185003 (2002).

[114] Y. Ehrlich, C. Cohen, A. Zigler, J. Krall, P. Sprangle, and E. Esarey, Phys. Rev. Lett. **77**, 4186 (1996).

[115] W.P. Leemans, B. Nagler, A.J. Gonsalves, C. Tóth, K. Nakamura, C.G.R. Geddes, E. Esarey, C.B. Schroeder, and S.M. Hooker, Nat. Phys. **2**, 696 (2006).

[116] W.P. Leemans, A.J. Gonsalves, H.S. Mao, K. Nakamura, C. Benedetti, C.B. Schroeder, C. Tóth, J. Daniels, D.E. Mittelberger, S.S. Bulanov, J.L. Vay, C.G.R. Geddes, and E. Esarey, Phys. Rev. Lett. **113**, 245002 (2014).

[117] N.A. Bobrova, P. V. Sasorov, C. Benedetti, S.S. Bulanov, C.G.R. Geddes, C.B. Schroeder, E. Esarey, and W.P. Leemans, Phys. Plasmas **20**, 020703 (2013).

[118] J.E. Shrock, B. Miao, L. Feder, and H.M. Milchberg, Phys. Plasmas **29**, 073101 (2022).

[119] D. Marcuse, Bell Syst. Tech. J. **56**, 703 (1977).

[120] R. Lehe, M. Kirchen, I.A. Andriyash, B.B. Godfrey, and J.L. Vay, Comput. Phys. Commun. **203**, 66 (2016).

[121] M. Kolesik and J. V. Moloney, Phys. Rev. E - Stat. Physics, Plasmas, Fluids,

Relat. Interdiscip. Top. **70**, 036604 (2004).

[122] B. Miao, J.E. Shrock, L. Feder, R.C. Hollinger, J. Morrison, R. Nedbailo, A. Picksley, H. Song, S. Wang, J.J. Rocca, and H.M. Milchberg, ArXiv:2112.03489v2 (2021).

[123] A. Morozov, A. Goltsov, Q. Chen, M. Scully, and S. Suckewer, Phys. Plasmas **25**, 053110 (2018).

[124] A. Picksley, A. Alejo, R.J. Shalloo, C. Arran, A. Von Boetticher, L. Corner, J.A. Holloway, J. Jonnerby, O. Jakobsson, C. Thornton, R. Walczak, and S.M. Hooker, Phys. Rev. E **102**, 53201 (2020).

[125] K. Okamoto, *Fundamentals of Optical Waveguides* (Academic Press, New York, 2005).

[126] C.K. Birdsall and A.D. Langdon, *Plasma Physics via Computer Simulation* (CRC Press, Boca Raton, 1991).

[127] T.D. Arber, K. Bennett, C.S. Brady, A. Lawrence-Douglas, M.G. Ramsay, N.J. Sircombe, P. Gillies, R.G. Evans, H. Schmitz, A.R. Bell, and C.P. Ridgers, Plasma Phys. Control. Fusion **57**, 113001 (2015).

[128] J.L. Vay, A. Huebl, A. Almgren, L.D. Amorim, J. Bell, L. Fedeli, L. Ge, K. Gott, D.P. Grote, M. Hogan, R. Jambunathan, R. Lehe, A. Myers, C. Ng, M. Rowan, O. Shapoval, M. Thévenet, H. Vincenti, E. Yang, N. Zaïm, W. Zhang, Y. Zhao, and E. Zoni, Phys. Plasmas **28**, 023105 (2021).

[129] J.L. Vay, C.G.R. Geddes, E. Cormier-Michel, and D.P. Grote, J. Comput. Phys. **230**, 5908 (2011).

[130] J.L. Vay, Phys. Rev. Lett. **98**, 130405 (2007).

[131] J. Durnin, J. Miceli, and J.H. Eberly, Phys. Rev. Lett. **58**, 1499 (1987).

[132] A. Vasara, J. Turunen, and A.T. Friberg, J. Opt. Soc. Am. A **6**, 1748 (1989).

[133] J. Durnin, J. Opt. Soc. Am. A **4**, 651 (1987).

[134] D. McGloin and K. Dholakia, Contemp. Phys. **46**, 15 (2005).

[135] V. Grillo, E. Karimi, G.C. Gazzadi, S. Frabboni, M.R. Dennis, and R.W. Boyd, Phys. Rev. X **4**, 011013 (2014).

[136] M.K. Bhuyan, F. Courvoisier, P.A. Lacourt, M. Jacquot, R. Salut, L. Furfaro, and J.M. Dudley, Appl. Phys. Lett. **97**, 081102 (2010).

[137] J. Dudutis, R. Stonys, G. Račiukaitis, and P. Gečys, Opt. Express **26**, 3627 (2018).

[138] K.-S. Lee and J.P. Rolland, Opt. Lett. **33**, 1696 (2008).

[139] J. Arlt, V. Garces-Chavez, W. Sibbett, and K. Dholakia, Opt. Commun. **197**, 239 (2001).

[140] D. McGloin, V. Garcés-Chávez, and K. Dholakia, Opt. Lett. **28**, 657 (2003).

[141] J.H. McLeod, J. Opt. Soc. Am. **44**, 592 (1954).

[142] R.M. Herman and T.A. Wiggins, J. Opt. Soc. Am. A **8**, 932 (1991).

[143] N. Chattrapiban, E.A. Rogers, D. Cofield, W.T. Hill, III, and R. Roy, Opt. Lett. **28**, 2183 (2003).

[144] G.J. Swanson and W.B. Veldkamp, Opt. Eng. **28**, 605 (1989).

[145] D.C. O'Shea, T.J. Suleski, A.D. Kathman, and D.W. Prather, *Diffractive Optics: Design, Fabrication, and Test* (SPIE Press, Bellingham, Washington, 2009).

[146] G.J. Swanson, *Binary Optics Technology : Theoretical Limits on the Diffraction Efficiency of Multilevel Diffractive Optical Elements* (Lexington, Ma, 1991).

147

[147] I.A. Erteza, *Diffraction Efficiency Analysis for Multi-Level Diffractive Optical Elements* (Albuquerque, NM, 1995).

[148] B. Miao, Laser Wakefield Accelerator Experiments: Coherent Injection Radiation and Optical Field Ionization Based Plasma Waveguides, University of Maryland, College Park, 2020.

[149] M. Shutova, Z. Liege, A. Goltsov, A. Morozov, and A. V. Sokolov, J. Opt. Soc. Am. B **36**, 1313 (2019).

[150] B. Miao, J.E. Shrock, E. Rockafellow, and H.M. Milchberg, *No Title* (2023).

[151] N. Jhajj, E.W. Rosenthal, R. Birnbaum, J.K. Wahlstrand, and H.M. Milchberg, Phys. Rev. X **4**, 011027 (2014).

[152] A. Goffin, I. Larkin, A. Tartaro, and H.M. Milchberg, Phys. Rev. X **13**, 11006 (2022).

[153] T. Čižmár, M. Mazilu, and K. Dholakia, Nat. Photonics **4**, 388 (2010).

[154] K.D. Wulff, D.G. Cole, R.L. Clark, R. DiLeonardo, J. Leach, J. Cooper, G. Gibson, and M.J. Padgett, Opt. Express **14**, 4170 (2006).

[155] J. Houzet, N. Faure, M. Larochette, A.-C. Brulez, S. Benayoun, and C. Mauclair, Opt. Express **24**, 6542 (2016).

[156] B. Miao, L. Feder, J.E. Shrock, and H.M. Milchberg, Opt. Express **30**, 11360 (2022).

[157] M.C. Downer, R. Zgadzaj, A. Debus, U. Schramm, and M.C. Kaluza, Rev. Mod. Phys. **90**, 35002 (2018).

[158] J.C. Sivells, J. Spacecr. Rockets **7**, 1292 (1970).

[159] M. Takeda, H. Ina, and S. Kobayashi, J. Opt. Soc. Am. **72**, 156 (1982).

[160] G.R. Plateau, N.H. Matlis, C.G.R. Geddes, A.J. Gonsalves, S. Shiraishi, C. Lin, R.A. Van Mourik, and W.P. Leemans, Rev. Sci. Instrum. **81**, 0833108 (2010).

[161] V. Dribinski, A. Ossadtchi, V.A. Mandelshtam, and H. Reisler, Rev. Sci. Instrum. **73**, 2634 (2002).

[162] A.J. Gonsalves, K. Nakamura, C. Lin, J. Osterhoff, S. Shiraishi, C.B. Schroeder, C.G.R. Geddes, C. Tóth, E. Esarey, and W.P. Leemans, Phys. Plasmas **17**, 056706 (2010).

[163] A. Buck, K. Zeil, A. Popp, K. Schmid, A. Jochmann, S.D. Kraft, B. Hidding, T. Kudyakov, C.M.S. Sears, L. Veisz, S. Karsch, J. Pawelke, R. Sauerbrey, T. Cowan, F. Krausz, and U. Schramm, Rev. Sci. Instrum. **81**, 033301 (2010).

[164] T. Kurz, J.P. Couperus, J.M. Krämer, H. Ding, S. Kuschel, A. Köhler, O. Zarini, D. Hollatz, D. Schinkel, R. D'Arcy, J.-P. Schwinkendorf, J. Osterhoff, A. Irman, U. Schramm, and S. Karsch, Rev. Sci. Instrum. **89**, 093303 (2018).

[165] K.A. Tanaka, T. Yabuuchi, T. Sato, R. Kodama, Y. Kitagawa, T. Takahashi, T. Ikeda, Y. Honda, and S. Okuda, Rev. Sci. Instrum. **76**, 013507 (2005).

[166] C. Huang, W. Lu, M. Zhou, C.E. Clayton, C. Joshi, W.B. Mori, P. Muggli, S. Deng, E. Oz, T. Katsouleas, M.J. Hogan, I. Blumenfeld, F.J. Decker, R. Ischebeck, R.H. Iverson, N.A. Kirby, and D. Walz, Phys. Rev. Lett. **99**, 255001 (2007).

[167] C.M. Huntington, A.G.R. Thomas, C. McGuffey, T. Matsuoka, V. Chvykov, G. Kalintchenko, S. Kneip, Z. Najmudin, C. Palmer, V. Yanovsky, A. Maksimchuk, R.P. Drake, T. Katsouleas, and K. Krushelnick, Phys. Rev. Lett. **106**, 105001 (2011).

[168] P. Sprangle, J. Krall, and E. Esarey, Phys. Rev. Lett. **73**, 3544 (1994).

[169] D.F. Gordon, A. Ting, T. Jones, B. Hafizi, R.F. Hubbard, and P. Sprangle, Proc.

IEEE Part. Accel. Conf. **3**, 1846 (2003).

[170] B.F.W. Croke, Publ. Astron. Soc. Pacific **107**, 1255 (1995).

[171] W. Pych, Publ. Astron. Soc. Pacific **116**, 148 (2004).

[172] P.G. van Dokkum, Publ. Astron. Soc. Pacific **113**, 1420 (2001).

[173] M. Ester, H.-P. Kriegel, J. Sander, and X. Xu, Proc. 2nd Int. Conf. Knowl. Discov. Data Min. 226 (1996).

[174] Y. Glinec, J. Faure, A. Guemnie-Tafo, V. Malka, H. Monard, J.P. Larbre, V. De Waele, J.L. Marignier, and M. Mostafavi, Rev. Sci. Instrum. **77**, 103301 (2006).

[175] K. Nakamura, W. Wan, N. Ybarrolaza, D. Syversrud, J. Wallig, and W.P. Leemans, Rev. Sci. Instrum. **79**, 053301 (2008).

[176] C.M.S. Sears, S.B. Cuevas, U. Schramm, K. Schmid, A. Buck, D. Habs, F. Krausz, and L. Veisz, Rev. Sci. Instrum. **81**, 073304 (2010).

[177] K. Nakamura, A.J. Gonsalves, C. Lin, A. Smith, D. Rodgers, R. Donahue, W. Byrne, and W.P. Leemans, Phys. Rev. Spec. Top. - Accel. Beams **14**, 062801 (2011).

[178] K. Nakamura, D.E. Mittelberger, A.J. Gonsalves, J. Daniels, H.S. Mao, F. Stulle, J. Bergoz, and W.P. Leemans, Plasma Phys. Control. Fusion **58**, 034010 (2016).

[179] Y. Wang, S. Wang, A. Rockwood, B.M. Luther, R. Hollinger, A. Curtis, C. Calvi, C.S. Menoni, and J.J. Rocca, Opt. Lett. **42**, 3828 (2017).

[180] D.C. O'Shea, T.J. Suleski, A.D. Kathman, D.W. Prather, and Society of Photo-optical Instrumentation Engineers., *Diffractive Optics : Design, Fabrication, and Test* (SPIE, 2004).

[181] V. Malka, J. Faure, J.R. Marquès, F. Amiranoff, J.P. Rousseau, S. Ranc, J.P.

Chambaret, Z. Najmudin, B. Walton, P. Mora, and A. Solodov, Phys. Plasmas **8**, 2605 (2001).

[182](n.d.).

[183] E. Esarey, B.A. Shadwick, C.B. Schroeder, and W.P. Leemans, AIP Conf. Proc. **737**, 578 (2004).

[184] T.R. Clark and H.M. Milchberg, Phys. Rev. Lett. **81**, 357 (1998).

[185] K. Nakamura, H.S. Mao, A.J. Gonsalves, H. Vincenti, D.E. Mittelberger, J. Daniels, A. Magana, C. Toth, and W.P. Leemans, IEEE J. Quantum Electron. **53**, (2017).

[186] C. Benedetti, F. Rossi, C.B. Schroeder, E. Esarey, and W.P. Leemans, Phys. Rev. E - Stat. Nonlinear, Soft Matter Phys. **92**, 1 (2015).

[187] R. Bharuthram, J. Parashar, and V.K. Tripathi, Phys. Plasmas **6**, 1611 (1999).

[188] I. Golub, B. Chebbi, D. Shaw, and D. Nowacki, Opt. Lett. **35**, 2828 (2010).